In situ Characterization of Dynamic Structures of Coatings

A DISSERTATION
SUBMITTED TO THE FACULTY OF THE GRADUATE SCHOOL
OF THE UNIVERSITY OF MINNESOTA
BY

Jin-Oh Song

IN PARTIAL FULFILLMENT OF THE REQUIREMENTS
FOR THE DEGREE OF
DOCTOR OF PHILOSOPHY

Lorraine F. Francis, Advisor

April 2012

Acknowledgements

First of all, I would like to express my sincere gratitude to my advisor, Prof. Lorraine F. Francis, for guiding and supporting me to become an independent researcher. Without her continuous encouragement and support, I would not have completed this project successfully. I want to thank the members of my dissertation committee, Prof. Chris W. Macosko, Prof. Alon V. McCormick, and Prof. Jian Ping Wang who provided me with thoughtful and brilliant advice and guidance. Also, I am extremely grateful to IPRIME industrial fellows, Dr. Robert Henry in Nexolve Corp. and Dr. Bruce Forsyth in Boston Scientific Inc., who helped me academically to discuss and design unique experimental methods for this project. I would like to express my sincere gratitude to Mr. Wieslaw Suszynski and Dr. Jinping Dong who gave me a lot of technical assistances. I want to give a special thank you to my previous and current group members, Karan Jindal, Christine Cardinal, Heng Zhang, Erica Redline, Sreeram Kalpathy, Kyle Price and Bryce Williams at Room 424 in Amundson Hall for their sincere assistances. Finally, I would like to express my deepest and highest appreciation to my family in Korea, especially, father, mother, and sister. Without their unconditional love, I could never have completed this long journey successfully.

Abstract

We have developed new methods and apparatus to characterize the structure changes of coatings *in situ*. The techniques enabled the study of critical factors to control during drying or curing process to avoid excess materials use and coating defects. The instruments have been used to investigate the effect of process conditions on the structure development and final coating properties.

A magnetic microrheometer for *in situ* measurement of local viscosity of coatings was designed since conventional bulk rheometry cannot be used to follow the temporal and spatial gradients of viscosity in drying or curing coatings. Micron-sized magnetic probe particles under a magnetic field gradient act as probes for local rheological responses in coatings. Viscosity-time profiles were measured in drying aqueous PVA coatings, and the results revealed the correlation between sagging defects and viscosity build-up. The development of viscosity gradient through the thickness in UV curing epoxy coatings was also characterized to study wrinkling defects, skin formation, and structure or composition gradients through the coating thickness.

The microstructure of drug-polymer coatings was also characterized using confocal Raman microscopy. A drying apparatus was built to control the coating method, drying temperature, and air flow during the characterization since the size and distribution of drug phase and polymer structure in the coating strongly depend on the process conditions. The dependence of environmental inputs to the drug and polymer coating morphology during drying was investigated in order to elucidate and optimize either the processing conditions or coating formulation.

Table of Contents

Acknowledgements ……

Abstract ……

Table of Contents ……

List of Tables ……

List of Figures ……

Chapter 1. Introduction ……

1.1 Motivation ……

1.2 Objective of Research ……

1.3 Overview of Thesis ……

Chapter 2. Background ……

2.1 Introduction to Solidification of Coatings …… 7

2.1.1 Elementary process and phenomena …… 7

2.1.2 Rheological properties of coatings during solidification …… 11

2.1.3 Microstructure of drug-polymer coatings …… 14

2.2 Microrheology Methods …… 1

2.2.1 Overview ……

2.2.2 Particle motions in Newtonian fluids …… 18

2.2.3 Rheological response measurement …… 23

2.2.4 Active and passive microrheology methods …… 28

2.3 Confocal Raman Microscopy ····· 40
2.3.1 Overview ·····
2.3.2 Basic principles ·····

Chapter 3. Design of Magnetic Microrheometer ····· 45
3.1 Introduction ·····
3.2 Basic Theory ·····
3.3 Apparatus Design ·····
3.3.1 Magnet configuration and magnetic probe particles ····· 54
3.3.2 Particle imaging and data acquisition ····· 59
3.3.3 Process control system ····· 6
3.3.4 Magnetic microrheometer ····· 61
3.4 System Validation ·····
3.4.1 Materials and methods ····· 6
3.4.2 Comparison with bulk rheometry ····· 66
3.4.3 Wall effect correction ····· 7
3.4.4 Coating viscosity measurement during drying process ····· 75
3.5 Summary ·····

Chapter 4. Depthwise Viscosity Gradient in UV cured Epoxy Coatings ····· 80
4.1 Introduction ·····
4.2 Experimental Section ·····
4.2.1 Materials and methods ····· 8
4.2.2 Particle tracking for viscosity gradient measurement ····· 87
4.3 Results and Discussion ····· 9
4.3.1 Effect of photoinitiator concentration ····· 91
4.3.2 Effect of UV light source ····· 100
4.3.4 Effect of curing temperature ····· 104
4.4 Summary ·····

Chapter 5. Viscosity and Surface Flow in Drying Coatings ····· 109
5.1 Introduction ·····
5.2 Experimental Section ····· 11
5.2.1 Materials and methods ····· 111
5.2.2 Particle tracking for surface flow measurement ····· 112
5.3 Results and Discussions ····· 11
5.3.1 Viscosity and surface of drying PVA coatings ····· 114
5.3.2 Analysis of sag length ····· 119
5.3.3 Effect of free surface on particle tracking ····· 121
5.4 Summary ·····
Chapter 6. Microstructure Evolution in Drug-Polymer Coatings ····· 126
6.1 Introduction ·····
6.2 Design of apparatus for *in situ* confocal Raman microscopy ····· 129
6.2.1 Mass loss measurement system ····· 129
6.2.2 Drying channel ····· 1
6.3 Experimental Section ····· 1
6.3.1 Materials and methods ····· 133
6.3.2 Confocal Raman microscopy ····· 133
6.4 Results and Discussion ····· 13
6.4.1 Quantification of evaporation rate ····· 136
6.4.2 Characterization of drug domains ····· 139
6.4.3 Effect of drying rate on structure development ····· 143
6.4.4 Effect of sterilization process ····· 147
6.5 Summary ·····
Chapter 7. Future Work ·····
7.1 Introduction ·····
7.2 Alternative System Design····· 153

7.3 Drying Coating Surface····· 15

Bibliography ·····

List of Tables

Table 2.1 Comparison of microrheology methods ····· 34

Table 3.1 Predicted and measured magnetic field gradient as a function of gap between two permanent magnets ····· 57

Table 4.1 Rate coefficient (*n*) at each depth in coatings with different PI concentrations ·····

Table 4.2 Rate coefficient (*n*) at each depth in coatings cured at different UV light wavelength ····· 1

Table 4.3 Rate coefficient (*n*) at each depth in coatings cured with different UV irradiance ····· 1

Table 4.4 Rate coefficient (*n*) at each depth in coatings cured at different temperatures ····· 107

Table 5.1 Coating thickness decease as a function of drying temperature from the mass loss measurement of 12.1 wt.% PVA coatings ····· 122

Table 6.1 Mass loss rate of various solvents and mixtures ····· 137

List of Figures

Figure 1.1 Research scheme and characterization method for each coating system ……

Figure 2,1 The elementary processes and phenomena during solidification of coatings ……

Figure 2.2 Forces on embedded small sphere probe in Newtonian liquid; F_{ext}, can be from electric or magnetic field, mechanical force and thermal energy ($\sim k_B T$) …… 2

Figure 2.3 Stress response vs time for (a) strain γ in (b) Hookean solid, (c) Newtonian fluid, and (d) viscoelastic solid and liquid …… 24

Figure 2.4 Stress relaxation data for a polydimethylsiloxane. Stress decays exponentially, and the decay rate strongly depends on the strain γ …… 25

Figure 2.5 Schematics of (a) magnetic manipulation method, (b) optical tweezer, and (c) atomic force microscopy …… 30

Figure 2.6 Microrheology experiment with oscillatroy magnetic force. Schematic diagram of (a) experimental set up, (b) the applied magnetic field and the particle response, and (c) the equivalent viscoelastic model for the system …… 33

Figure 2.7 Experimental steps for the particle tracking method. (a) Particle trajectory in x-y plane measured and (b) the average fluctuation spectrum vs time plotted (b) …… 39

Figure 2.8 Schematic representation of (a) Rayleigh scattering, (b) Stokes scattering, and (c) anti-Stokes scattering …… 44

Figure 3.1 Particle velocity vs time under different magnetic filed gradient (T/m) (60 : solid line, 40 : dashed line, and 20 : dotted line) within coating solutions with different viscosities of η = (a) 0.001, (b) 1, (c) 10, and (d) 1,000 (Pa·s) …… 51

Figure 3.2 (a) The particle velocity changes as a function of viscosity of coatings for the magnetic particle with radius of 2 μm and M_s of 0.1 (T) under different external magnetic gradient (T/m) (60 : solid line, 40 : dashed line, and 20 : dotted line), and (b) the dependence on the magnetic

field gradient (*dB/dx*) and the radius of the particle in the coating of which η = 10 (Pa·s) ····· 5

Figure 3.3 Simulation (solid) and experimental (open) results of magnetic field gradient of single magnet configuration and double magnet configuration with 10 mm gap between magnets ····· 56

Figure 3.4 (a) SEM image and (b) magnetization curve of MS0302 probe particles ·····

Figure 3.5 Pictures of (a) the sample stage and (b) the temperature/ heating process controller. The sample stage is connected with thermocouple, gas inlet, and heater. Gas outlets are holes in the sample stage ·····

Figure 3.6 Overview of magnetic microrheometer setup, (a) schematics of the apparatus and configuration of control units, (b) picture of the apparatus, and (c) dimensions and details of magnets, magnet holders/adapters, and sample stage A: magnet holder and adapter B: NdFeB permanent magnet (D×L: 12.7×50.8 mm) C: stepper motor D: optical microscope (magnification: x140~1,400, working distance: 13 mm) E: sample stage connected to solidification system, F: micropositioner, G: Hall probe Gaussmeter, H: Clip to hold coating samples) ·····

Figure 3.7 Velocity of probe particles in (a) aqueous glycerol (96.7 wt. %) solution and (b) 10.5 wt. % PIP solution ····· 68

Figure 3.8 Schematic representation of (a) the particle velocity measurement and (b) acquired particle trajectory of MS0302 magnetic particle in PVA coating without drying process ····· 70

Figure 3.9 Viscosity versus shear rate of PIP and PVA wet coatings from particle velocity measurement (open), and the results of coating solution from standard bulk rheometry (solid) ····· 71

Figure 3.10 Theoretical prediction and experimental data of the effect of coating substrate on particle velocity within wet PIP coating as a function of position through coating thickness. Theoretical prediction and experimental measurements were done with 0.5 μm-radius particle in PI coating (=3.2 Pa s) under the applied magnetic field gradient of 65 T/m ·····

Figure 3.11 Particle velocity changes (solid square) in PVA coating and

calculated viscosity (open square) of PVA coating as a function of drying time ……

Figure 3.12 PVA coating viscosity change from particle velocity measurement at different drying temperatures; 27 ^{o}C (open circle), 60 ^{o}C (open triangle) and 80 ^{o}C (solid circle) …… 78

Figure 4.1 Chemical structures of (a) bis-(3,4-epoxycyclohexylmethyl) adipate and (b) a mixed triarylsulfonium hexafluoroantimonate salts …… 86

Figure 4.2 Schematics of (a) particle velocity measurements in UV curing coatings at different *z* positions (z_1: 70, z_2: 55 and z_3: 35 µm from the substrate), and (b) an example of the accumulated particle displacement along the applied magnetic field direction in UV curing coatings …… 89

Figure 4.3 Schematic representation (not to scale) of the particle trajectories of magnetic probe particles at each *z* position in the wet epoxy coating …… 90

Figure 4.4 Real-time degree of conversion measurements using FTIR as a function of curing time of epoxy coatings with 0.2 and 2 wt.% PI concentration. Sample thickness for the conversion measurement is 80 µm. Data was collected with a UV wavelength of 365 nm at 20 µW·cm^{-2} …… 93

Figure 4.5 Viscosity-time profile of ~80 µm epoxy coatings at different *z* positions during curing with 365 nm UV lamp with an irradiance of 20 µW·cm^{-2} with the PI concentration of (a) 0.2 wt.% and (b) 2 wt.%. Equation (4) was used to fit the data. Error bars are based on the standard deviation of multiple measurements of particle velocity in a given time period, and the sample to sample variations. Equation (4.2) was used to fit the viscosity-time curves …… 94

Figure 4.6 Epoxy coating surfaces after 90 minutes of curing cured with 365 nm and 20 µW·cm^{-2} UV light with coating thicknesses and PI concentrations of (a) 80 µm and 0.2 wt.%, (b) 80 µm and 2 wt.%, (c) 100 µm and 0.2 wt.%, (d) 20µm and 0.2 wt.%, and (e) 20 µm and 2 wt.% …… 96

Figure 4.7 Defect regime map of epoxy coating cured with 365 nm and 20 µW·cm^{-2} UV light …… 9

Figure 4.8 Effect of UV light wavelength on the viscosity-time profile of ~80 µm epoxy coatings with 0.2 wt.% PI concentration. Coating samples were cured with an irradiance of 20 µW·cm^{-2} at room temperature using (a) a 365 nm lamp and (b) 254 nm lamp. Equation (4.2) was used to fit the viscosity-time curves …… 101

Figure 4.9 (a) UV absorption spectra of PI (UVI-6976) and the mixture of epoxy monomer with 0.2 wt.% PI, and (b) schematic of emission spectra of 254 and 365 nm UV lamps, illustrated using the product information ⋯101

Figure 4.10 Effect of UV light intensity on the viscosity-time profile of ~80 μm epoxy coatings with 0.2 wt.% PI concentration. Coating samples were cured with a 254 nm UV lamp at room temperature with an irradiance of (a) 20 $\mu W \cdot cm^{-2}$ and (b) 1,000 $\mu W \cdot cm^{-2}$. Equation (4.2) was used to fit the viscosity-time curves ⋯⋯103

Figure 4.11 Effect of curing temperature on the viscosity-time profile of ~80 μm epoxy coatings with 0.2 wt.% PI concentration. Coating samples were cured with a 254 nm UV lamp with an irradiance of 1,000 $\mu W \cdot cm^{-2}$ at (a) room temperature and (b) 60 ^{o}C. Equation (4.2) was used to fit the viscosity-time curves ⋯⋯106

Figure 4.12 Epoxy coating surfaces after 60 minutes of curing with 254 nm and 1,000 $\mu W \cdot cm^{-2}$ UV light at (a) room temperature and (b) 60 ^{o}C. Coating thickness is ~80 μm, and PI concentration is 0.2 wt.% ⋯⋯107

Figure 5.1 Schematic of (a) the magnetic microrheology for coating viscosity measurement and (b) spore motion tracking on a coating surface without magnetic field for sag length measurement on a tilt ($\theta = 7.5^{o}$) sample stage. The sample stage has channels for air/gas flow, and is connected to a heater with temperature controller ⋯⋯ 113

Figure 5.2 Particle velocity changes (solid square) in PVA coating and calculated viscosity (open square) of PVA coating as a function of drying time ⋯ 115

Figure 5.3 (a) Magnetic particle velocities measured at different drying times and tempeartures for a 12.1 wt.% PVA coating. (b) Coating viscosities calculated from the velocity data using Eq. (1). The viscosity build-up times at the various temperatures are marked ⋯⋯ 117

Figure 5.4 Final dried surfaces of 12.1 wt. % PVA coatings dried at different drying temperatures on flat or titled stage [drying temperature (^{o}C) / tilted angle (^{o})]. A circle shows uneven surfaces ⋯⋯ 118

Figure 5.5 Measured spore velocities on 12.1 wt.% PVA coating surfaces as a function of drying time to calculate sag length changes during drying at different temperatures. Measurements are taken on a tilted sample stage ⋯⋯

Figure 5.6 Illustration of the positions of coating surface and the probe particle within a focal plane (a) in an initial wet coating and (b) in a drying coating with thickness shrinkage ····· 122

Figure 5.7 Distance between coating surface and focal plane as a function of drying time at different temperatures ····· 124

Figure 6.1 (a) Schematic of mass loss system and pictures of (b) microbalance and (c) drying tunnel connected ····· 130

Figure 6.2 Schematic of (a) a portable drying apparatus, and (b) experimental set-up (not to scale) of confocal Raman microscopy with a drying apparatus and a temperature control system. A: stage for coating sample preparation, B: hole for confocal Raman microscopy, and C: air/gas inlet ·····

Figure 6.3 (a) Raman spectra of drug and (b) example chemical mapping of drug-polymer coating using lateral scan ····· 135

Figure 6.4 Normalized mass loss of solvent mixtures at room temperature and forced heat (FH) drying conditions ····· 137

Figure 6.5 Amount of solvent remaining in coating formulations (PLGA / DMF:THF) as a function of drying time and solid (PLGA) concentrations ·····

Figure 6.6 Raman lateral scan and cross-sectional SEM images drug-polymer coatings dried at (a) room temperature and (b) 90 ^{o}C ····· 139

Figure 6.7 Real-time Raman imaging of drug domains in the coating during drying at room temperature for (a) 37, (b) 38, (c) 39, (d) 40, and (e) 41 minutes using later scans at a fixed position (~ 2.5 µm from surface). The arrow indicates the direction of the lateral motion of a drug domain ·····

Figure 6.8 Real-time Raman imaging of vertical drug distribution through the coating thickness during drying at room temperature ····· 142

Figure 6.9 Drying front evolution and thickness shrinkage rate determined using real-time Raman depth scans of drug-polymer coatings during drying. Coatings were prepared using different Mayer rods (# 3 and # 5), and dried at room temperature with or without nitrogen flow ·····

Figure 6.10 Changes in drug domain size and distribution due to changes in drying temperature ····· 145

Figure 6.11 Averaged drug domain size change as a function of drying conditions ·····

Figure 6.12 Depth and lateral scans of (a) pre-sterile and (b) post-sterile drug-polymer coatings. Pre-sterile coatings was dried at 95 ^{o}C for 5 minutes and the dried sample was sterilized at 55 ^{o}C for 30 minutes with 99 % of relative humidity ····· 149

Figure 7.1 (a) Illustration of magnetic probe particle motions in silica/water system with a constant viscosity and (b) observed magnetic probe particle motions influenced by surrounding silica nanoparticles ····· 156

Chapter 1. Introduction

1.1 Motivation

In the ‘paints and coatings’ industry, the economic contribution of coatings to the United States gross domestic product was estimated to be $19.3 billon in 2010, and it is expected to grow after the global economic downturn in 2008 and 2009 [1]. Coating companies have developed new formulations and processes to improve the sustainability and cost efficiency of the products. Currently, lower limits on volatile organic compounds (VOC), and a growing demand for green products have driven coating researchers to find advanced technologies for both formulation and process. As new formulations and process strategies are explored, an effective measurement technique for coatings could save significant time and resources in product development.

Coating products have been used in many applications and have practical importance in a broad spectrum of manufacturing sectors, ranging from architectural and automotive coatings to functional coatings for biomedical devices and flexible electronics. In the coating process, a coating liquid prepared as a polymer solution or colloidal dispersion is applied onto a substrate by processes such as slot coating or spray coating. The applied coating liquid transforms into a final coating typically by drying, curing, chilling or some combination of these. Solidification of the applied coating liquid onto the substrate is frequently accomplished by drying (i.e, solvent removal by evaporation) or curing (i.e., chemical reaction, cross-linking). Particle coalescence or

phase separation can also occur depending on the type of coating materials as the coatings transform to the solid state. These phenomena can make the dynamic changes in viscosity, stress, and microstructure in the coatings [2-5]. The solidification processes are critical to the development of the final coating's structure and properties. Improper conditions can lead to excessive energy or material use, which lead to inefficient manufacturing and increased costs.

Control of rheological property is important to the design of effective coating processes. The rheology of the coating liquid before it is applied to the substrate is routinely characterized by various standard techniques [6]. Typically, these standard methods have been used to determine viscosity and the effect of shear rate on viscosity for designing the coating liquid application process, however, these methods cannot be used to characterize the rheological properties of the coating liquid after the deposition on the substrate. Information on the change in the viscosity of coated layer during solidification process would be useful for designing improved condition and preventing defects [7]. For example, coatings deposited onto vertical surfaces 'sag' or develop drips if their viscosity does not increase quickly enough after deposition [8]. However, coatings that build viscosity too quickly may not level to a smooth surface [9, 10]. Measurements of the viscosity of the coated layer as process conditions change would provide the information needed to find "process windows", or critical combinations of processing variables, for efficient manufacturing of defect-free coatings. Moreover, local viscosity in a coating, particularly depthwise gradients through the coating thickness, can also yield information on gradients in composition and structure [11].

In drug-polymer coating systems, control of drug phase during drying process is the key to achieve a desired function of drug eluting stents, such as drug release rate. The microstructure of drug-polymer coatings, specifically, the size and distribution of drug phase, strongly depends on temperature, air/gas flow and humidity. It is well known that in order to provide a controlled release rate of drug from a medical device, the drug microstructure should be stable and predictable over a wide range of environmental storage conditions. Recently, confocal Raman microscopy has been successfully used to investigate the microstructure of dried drug-polymer coatings, however, the previous results did not provide real-time structure development information [12-14]. In order to understand and control the microstructure evolution in drying drug-polymer coatings, a new approach to improve the previous experimental method is required to get experimental data for the dynamic microstructure of coatings during both solidification and subsequent dispensation.

Therefore, the characterization of these dynamic changes in the coating structure during solidification will be beneficial for desired final coating properties without various defects. In order to address the issues of previous standard methods, a new technique needs to be developed for *in situ* characterization of the coating structure development. The *in situ* characterization methods will be beneficial for the investigation of the spatial gradients in the structure development of coatings and their time evolution as they dry or cure. This will also provide information on fundamentals of solidification phenomena as well as on improved process conditions or material formulations.

1.2 Objective of Research

The primary objective of this research is to develop *in situ* characterization method as a tool to monitor the coating structure change in coatings during drying or curing process, and demonstrate how the information can be used to design more effective manufacturing processes for the coatings and to understand fundamentals of solidification phenomena. The specific research topics are (i) viscosity change measurement in coatings during drying and curing process and (ii) drug morphology change in drug-polymer coatings during drying. The research scheme, characterization methods, and parameters to control are summarized in Figure 1.1.

For *in situ* coating viscosity measurement, the development of a proper apparatus is required to measure the coating viscosity as a function of both time and depth into the coatings during drying and UV curing. The apparatus should be capable of characterizing real-time and depthwise viscosity through the coating thickness using a new concept to overcome the limitations of standard methods. The measured viscosity data under various drying and UV curing conditions is critical to understand the relationship between viscosity, surface defects, and solidification process conditions.

In addition, real-time drug phase characterization requires a drying apparatus capable of creating thin films and tracking microstructure development in-line with confocal Raman microscopy. It is important to produce a controlled microenvironment, such as air flow, temperature, and humidity, to vary the rate of solvent extraction out of the coatings during confocal Raman microscopy measurement. As a result of system integration, analyzed data over time in fixed lateral or cross-sectional regions of interest

provides the information needed to find the dependence of environmental inputs on the drug-polymer coating structure.

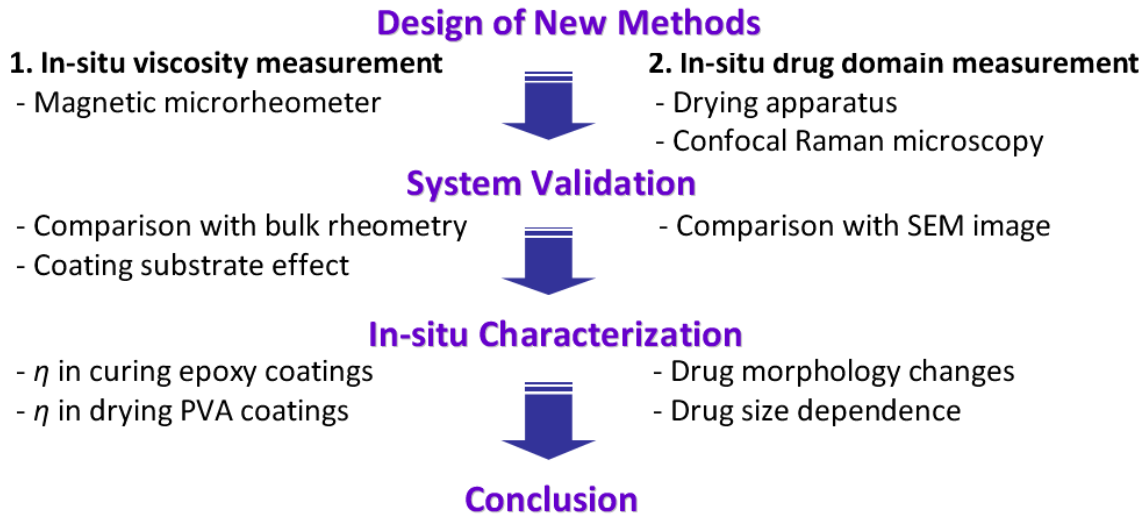

Figure 1.1 Research scheme and characterization method for each coating system.

1.3 Overview of Thesis

The thesis is organized into seven chapters. Chapter 1 provides the reader an overall introduction and outline of the research. Chapter 2 covers the background of coating solidification and structure characterization methods. The basic theory on microrheology methods and confocal Raman microscopy is described. Chapter 3 deals with the design of a new apparatus for viscosity measurement using magnetic microrheology technique. System validation results demonstrate that the designed apparatus, magnetic microrheometer, is capable of measuring coating viscosity during solidification *in situ*. The magnetic microrheometer is used to investigate depthwise viscosity gradients in UV curing coatings in Chapter 4. The effects of process conditions on the viscosity gradient development, on the rate of viscosity increase, and on surface defects were studied. Chapter 5 examines the time evolution of viscosity in drying coatings. The results of this chapter indicate the potential characterization methods in characterizing defects and viscosity development in drying coatings. Chapter 6 deals with the design of a drying apparatus for the integration with confocal Raman microscopy to follow drug morphology change in drug-polymer coatings during drying. The evaporation rate of various coating formulations was quantified to generate a right process window for real-time monitoring. Raman characterization data from both lateral and depth scans showed the dependence of drying rate and humidity on the size and distribution of drug domains. Chapter 7 concludes the thesis with prospects for future works.

Chapter 2. Background

2.1 Introduction to Solidification of Coatings

Coatings are generally applied in a liquid state, and then transformed into a final solid state through solidification processes. The development of final coating properties and microstructure can be significantly influenced by these solidification processes. If the process conditions are not controlled well, various coating defects and fails, such as crazing, curl, delamination and cracking may occur. In order to achieve the desired structures and properties of coatings, it is necessary to understand firmly main phenomena of solidification processes and to control the solidification process of coatings properly.

2.1.1 Elementary process and phenomena

Elementary processes of the solidification process are solvent evaporation from the surfaces of coatings, solvent diffusion to the surface from within coatings, fusion (coalescence) or binding, and other chemical reactions. Through all these elementary processes, coating viscosity can vary through its thickness since it is quite sensitive to liquid solvent composition, polymer chain configuration and stiffness, degree of cross-linking and temperature. Figure 2.1 provides a schematic representation of the elementary processes and phenomena during the solidification of coatings.

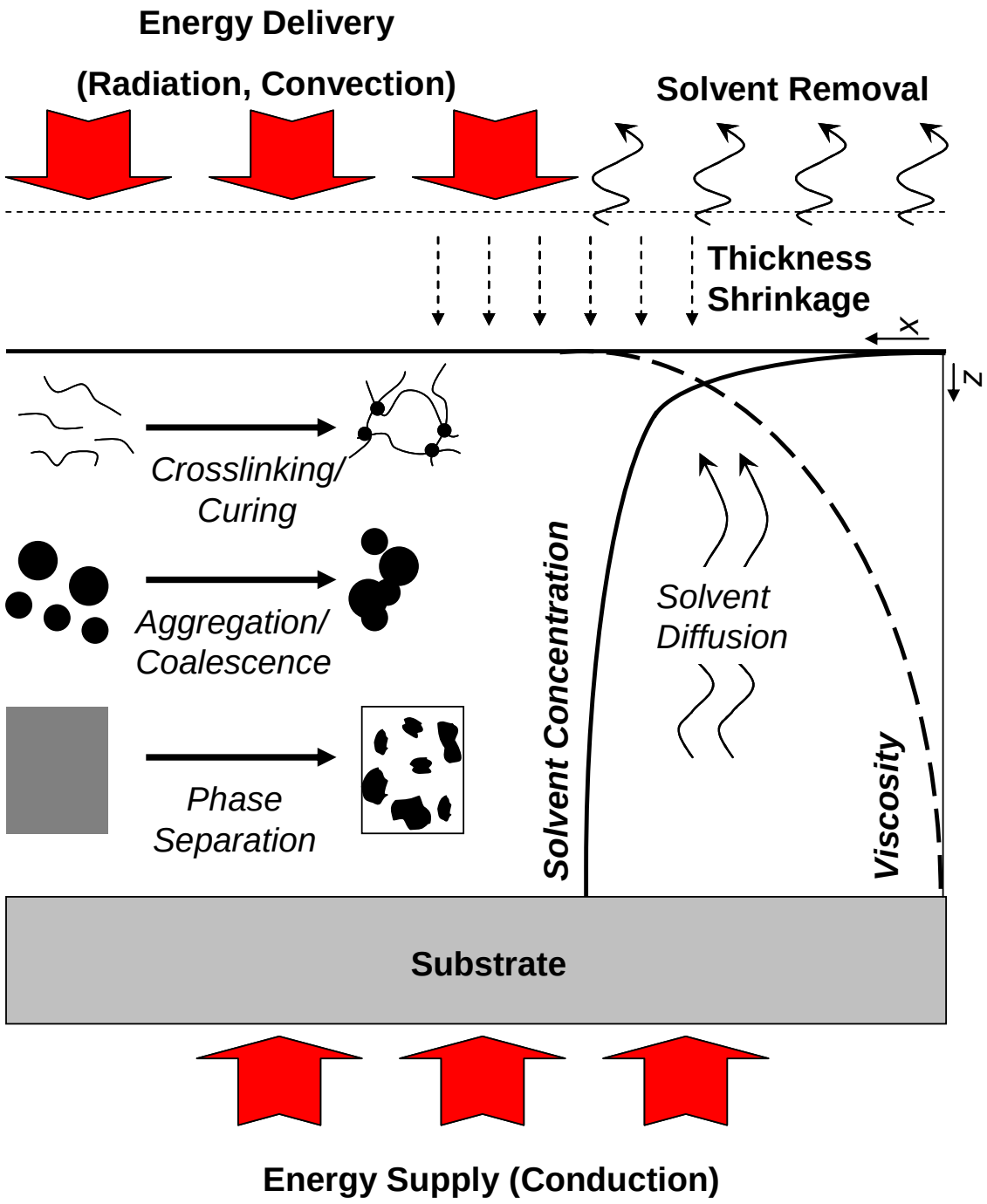

Figure 2.1 The elementary processes and phenomena during solidification of coatings.

Solvent removal and diffusion during solidification can result in solvent concentration gradients in coatings. Generally, the solvent diffuses from a higher concentration region (within the coating) to a lower concentration region (surface of the coating) during the solvent evaporation. Since the coating viscosity is sensitive to liquid solvent concentration, it can cause viscosity gradients within coatings [15]. The solvent removal and diffusion strongly depend on the partial solvent pressure in the drying gas and the temperature of the process [16].

Aggregation and coalescence of particles can also result in the solidification only at the solvent evaporation surface of coatings after drying. In a reactive polymer coating system, concentrated reactants at the surface of coatings can increase curing reactions. Therefore, increased polymer cross-linking enhances gelation at the coating surface, while the inside of the coating is still a liquid state [4]. This case causes composition gradients of the liquid solvents through the coating thickness, which may also lead to viscosity gradients.

During solidification process of coatings, these elementary processes usually produce volume shrinkage. Stresses can develop when a coating is confined to a rigid substrate [17]. In a polymer coating system, the stress can be relaxed quickly when it is a liquid state. During the solvent evaporation, the volume shrinks and the polymer chains relaxes by molecular rearranging within the coating in order to fill the volume left by the solvent evaporation. If the rate of the solvent evaporation and the polymer relaxation are same, the final coating is stress-free state. However, since the relaxation rate of polymer chains decreases due to the adhesion and the transition from a liquid-like state to a solid-

like state, the rate of solvent evaporation and polymer chain relaxation can be different practically. Slower polymer relaxation rate generally leaves a free-volume that is not filled with solvent or polymer. Therefore, the volume of stress-free state and that of the actual state are different, and this causes strain [18]. Stress within the coating develops when strain does within it. The stress in the coating also strongly depends on the solidification conditions, such as temperature, gas flow, and relative humidity [19].

'Skinning' is also an common phenomenon during solidification process. Skinning at the coating surface is the development of a solvent-depleted layer that has higher viscosity and a lower solvent diffusion coefficient than the deeper materials in a coating [4]. This layer can form due to falling diffusion coefficient of solvent, phase/colloidal transformation or chemical reaction at the coating surface prior to the inside materials of a coating. Under severe drying conditions, such as high temperature and high air flow rate, a significant drop in solvent concentration near the coating can also result in skinning. *'Figurative skinning'* occurs at the coating surface where sharp gradients of concentration, viscosity and solvent diffusivity are developed [16]. *'Literal skinning'* is the formation of more solid-like layer at the coating surface when the inside material remains liquid [4]. Finally, *'Trapping skinning'* explains a case that more residual solvent within the coating under severe drying conditions (higher airflow or higher temperature) [20]. Generally, skinning is not a desired phenomenon in coating process since it can result in many defects and failures, such as cracking, non-uniform drying rate through the coating, and non-uniform microstructure and composition in coatings. Various types of

skinning from different mechanisms may occur individually or in combination during the solidification process.

2.1.2 Rheological properties of coatings during solidification

Rheological properties of coatings can change dramatically during the solidification process due to solvent concentration changes or chemical reactions. It is necessary to measure rheological properties of coatings continuously during the solidification process for better understanding of solidification phenomena [21]. The characterization of rheological properties of various coating systems will be useful to study the relation between coating viscosity at each solidification stage and its influence on final properties and defects.

In UV curable coating systems, coating materials generally consist of a photoinitiator (PI) and a mixture of reactive monomers and oligomers. UV light absorbed by the PI induces photopolymerization to form the final coating product. The curing reaction kinetics and structure development rate are affected by the type and concentration of PI, the wavelength and irradiance of UV light, and curing temperature [22]. With PI absorption, the variation in the UV irradiance through the thickness leads to the development of a conversion gradient. The surface of the coating receives a higher irradiance of light and hence experiences a higher conversion. In the extreme, a solidified skin can form at the coating surface. The skin can develop compressive stress due to the swelling from the diffusion of unreacted monomer beneath. When the compressive stress

is high enough to make the skin buckle, wrinkles appear on the coating surface. Such nonuniformity can cause gradients in the rheological properties of the coatings as they cure. Since the development of coating viscosity as a function of time and depth into the coating strongly depends on the degree of photopolymerization [23, 24], the investigation of coating viscosity will be useful to study the effects of these parameters on the structure development, final properties, and related defects of UV cured coatings.

Previously, several methods have been developed to study the rheological properties of various UV curing systems. Modified parallel plate and oscillating rheometer designs have been used to monitor dynamic moduli (G', G'') during the UV curing process [25, 26]. These methods have been improved for a wide range of measurable rheological property with a shorter time scale , and the methods have been combined with real-time Fourier-transform infrared (FTIR) spectroscopy to relate the extent of conversion to rheological data [27]. However, the samples for these previous studies are placed between the plates, and are not coatings. Moreover, these methods provide depth-averaged data and are not able to characterize depthwise gradients in local rheological properties.

In situ characterization of the change in coating viscosity as a function of depth during photopolymerization would be useful for designing process conditions and coating formulations. Some progress in measuring depthwise gradients has been made. Raman spectroscopy [28] and nano-indentation [29], have been used to follow conversion and modulus, respectively, but not during photopolymerization. Particle tracking microrheology [30] methods were used to characterize the gelation time of UV curing

coatings as a function of depth during photopolymerization; however, this method did not provide real-time photorheology information.

In drying coatings, coating defects are often related to changes in the rheological properties of the applied coating liquid during drying [31, 32]. A coating liquid with lower viscosity can be beneficial for fast application and efficient leveling; however, coatings applied on a vertical or slanted substrate may 'sag' or develop drips as they dry if the viscosity does not increase quickly enough [8]. Sagging is a critical factor in determining the coating appearance in architectural coatings and automotive coatings that are applied by spraying [8, 33]. In addition, sagging may also occur when a web or substrate moves vertically upward just after the liquid is applied, as in roll coating and dip coating processes [31].

The extent of gravity-induced sagging flow on a vertical surface depends on the density, thickness, and viscosity of the coated layer [32, 34, 35]. Since the viscosity of the coated film increases substantially during drying, coating viscosity is one of the most critical factors for controlling sag. However, measuring the viscosity of coated liquid layers during drying is challenging. The viscosity of a coating liquid as a function of drying time (or solvent content) without deposition on a substrate has been studied using conventional rheometers [32, 36], and specially designed rheometers, such as modified plates [37] and T-bars [33]. These studies provide useful information; however, conventional methods cannot be used to follow the changes in rheological properties of coated layers during drying.

2.1.3 Microstructure of drug-polymer coatings

Control of drug/polymer structure is critical to the function of medical devices, such as drug eluting stents (DES). The performance of DES strongly depends on both the amount of total drug released and how the drug is released over time, and these can be affected by stent design, formulation, surrounding polymer structure, and drying process conditions [12, 13]. The function of DES has been controlled by changing the physical properties of polymers, drug/polymer ratio, and degree of mixing of drug in the mixture [38-40]. Such attempts have modified the size and spatial distribution of drug domains in the drug-polymer coatings, showing different characteristics of the medical devices. Especially, the drug morphology at the coating surface is critical for the device performance since the interface between the coating surface and human tissue affects biocompatibility [38]. Therefore, it is important to understand the structure of drug under various process conditions to control desired final coating properties for biomedical applications.

Previously, various analytical methods have been used for physical or chemical mapping of the drug-polymer coating structure to investigate the correlation between drug elution profile and the spatial distribution or contents of drug. Atomic force microscopy is useful to characterize surface topography as well as drug domains on the coating surface [41, 42]. Near infrared and Fourier transform infrared imaging has been used for chemical mapping due to the chemical selectivity for distinguishing the drug from the surrounding polymer matrix [43, 44]. However, these methods are surface limited; therefore, they cannot be used for depth profile through the coating thickness.

Electron spectroscopy for chemical analysis (ESCA) and time-of-flight secondary ion mass spectrometry (TOF-SIMS) have used for depth profiling of drug-polymer coatings to characterize the distribution of drug contents both at the surface and bulk in the coatings [38]. These techniques provided useful information on quantitative chemical analysis, however, the coating samples were characterized after the final structure development thorough solidification process, such as drying.

The structure development of drug-polymer coatings involves a range of physical or chemical phenomena, such as the nucleation or aggregation of drug particles, polymerization, and phase separation during solidification [45]. It is important to monitor the microstructure evolution in drug-polymer coatings to study kinetic parameters for nucleation or growth of drug phase since the desired drug structure is essential for the clinical efficacy of DES [12, 45]. This information will also be useful to design an enhanced process conditions for drying or sterilization to get better final coating products. The development of *in situ* analytical techniques, referred to as process analytical technologies (PATs) has improved the capability of in-line monitoring of complex dynamic characteristics of pharmaceutical products.

Raman spectroscopy has been used as a reliable and quantitative tool in PATs [45]. It has been used for process monitoring and control in pharmaceutical industry due to its advantages, such as non destructive and real-time manner, fast data acquisition, and minimum sample preparation for the characterization [46]. This technique has been applied to study drug crystallization process, phase transformation, polymer structures, and drug concentrations [47-50]. In addition, a combined tool with an optical microscope,

confocal Raman microscopy has the potential for the characterization of the structure evolution in DES since it provides non destructive chemical imaging of component distribution in drug/polymer mixtures with high chemical specificity and spatial resolution. The size and spatial distribution of drug phase in drug-polymer coatings has been characterized to investigate the effect of formulation and process conditions on the final performance of DES using confocal Raman microscopy [38].

2.2 Microrheology Methods

The viscosity can vary through the coating thickness direction due to the skin formation at the surface, structure development, and different solidification rates in coatings. Microrheology is applicable for this study, because it concerns the storage and dissipation of mechanical energy in materials at the micrometer or sub-micrometer ranges. Therefore, analyzing the motion of micron-sized particles and their velocities in coating layers, especially through coating thickness, can be useful for firm understanding of viscosity gradients and changes in coatings during the solidification process.

This section provides an overview of microrheology methods with various types of experimental measurements and feasible microrheology techniques for the characterization of rheological properties of coatings.

2.2.1 Overview

Rheology is defined as the science of deformation and the flow of matter under applied stress [6]; it finds practical application in the determination of viscosity. Microrheology investigates how the rheological responses change at micron or sub-micron length scale. In this microrheology technique, micron-sized probes locally deform the material and probe the rheological response of materials [51]. The conventional bulk rheology method generally requires a larger sample volume, which makes it impossible to measure local viscosity of materials and the viscosities of small samples. The

microrheology technique has emerged to address these issues. Microrheology describes various approaches that attempt to overcome limitations of traditional bulk rheology [52].

Microrheology has been applied to characterize the viscosity of various soft material systems, such as colloid and biological materials, polymers, and cells or biomolecules. The method also probe intracellular function and phase change during chemical reaction since many cellular processes and chemical reactions involve changes in the viscosity of materials at the micron level [53, 54]. However, microrheology method also has limitations. Sample materials must be transparent to light if optical microscopes are used to detect probe particle motions. In addition, it can be challenging to observe small motion of the probes in highly viscous samples. Overcoming such limits will be important for the extension of these methods to more complex systems.

2.2.2 Particle motions in Newtonian fluids

A Newtonian fluid shows a constant viscosity (η), and the viscosity can be described by :

$$\eta = \frac{\tau}{\dot{\gamma}} \tag{2.1}$$

In a Newtonian solution, stress (τ) increases linearly with a constant slope (η) as strain rate ($\dot{\gamma}$) increases In contrast, the fluid of which viscosity depends on the strain rate is called a non-Newtonian fluid. This behavior is described by using power law [6]:

$$\eta \approx \eta_0 K^{1-n} \dot{\gamma}^{n-1} \tag{2.2}$$

where η_0 is the viscosity when $\dot{\gamma}$ is very small, K and n are model parameters. Therefore, the viscosity of a non-Newtonian fluid cannot be determined by a constant at higher strain rate. When the viscosity of non-Newtonian fluid drops at a high shear strain rate, it is called shear thinning. If the viscosity increases with a shear strain rate, it is called shear thickening. The viscosity of both fluids shows the temperature dependence, and it generally decreases with increasing temperature. Andrade-Eyring equation describes the relation over a wide temperature (T) range [6, 55].

$$\ln \frac{\eta_1(T_1)}{\eta_2(T_2)} = \frac{\Delta E}{R}\left(\frac{1}{T_1} - \frac{1}{T_2}\right) \tag{2.3}$$

where E is the activation energy of the system, and R is the gas constant.

Since microrheology methods use the particle as the probe to measure rheological properties of the fluids, it is useful to study particle motion in fluids under applied forces. When the small sphere is embedded and moving in the fluid as shown in Figure 2.2, the sphere will experience several forces in the fluid, such as gravitational force, applied external force, drag force and elastic recovery force. The simple equation that governs particle motion in Newtonian fluid from Langevin equation is described as [51]:

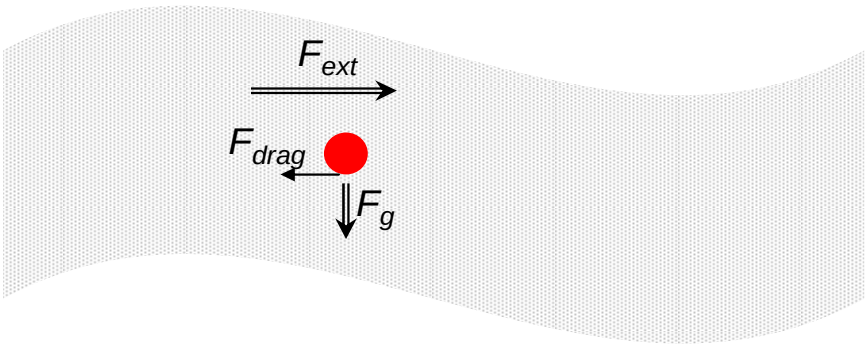

Figure 2.2 Forces on embedded small sphere probe in Newtonian liquid; F_{ext}, can be from electric or magnetic field, mechanical force and thermal energy ($\sim k_B T$).

$$m\frac{d^2x(t)}{dt^2} = F_{ext} + F_{drag} + F_g \tag{2.4}$$

where m is mass of the particle and $x(t)$ is its displacement. The particle will move along the external applied force F_{ext} or gravitational force F_g, but particle motion can be hindered by hydrodynamic interaction with drag force $F_{drag.}$ F_{ext} can be from thermal energy, mechanical energy, and electric field or magnetic field gradient. F_{drag} depends on the drag coefficient of the system, which includes the viscosity (η) and density (ρ) of a medium, the size of a particle, and the distance between a particle and a wall or substrate.

In a particular system, the Reynold number (R_e) described in Equation (2.5) is low due to the low particle velocity (v) and small radius (a) of a rigid sphere, so the inertia force ($m\, d^2x(t)/dt^2$) is negligible [56].

$$R_e = \frac{inertia \quad force}{viscous \quad force} = \frac{va\rho}{\eta} \tag{2.5}$$

Therefore, the sphere velocity can be determined by the force balance between F_{ext}, F_{drag}, and F_g within a medium. In a totally viscous system with only a gravitational force on a sphere, the sphere motion was studied and its equilibrium sedimentation velocity is described as [57]:

$$v_{sed} = \frac{2a^2 m^* g}{9V\eta} \tag{2.6}$$

where V is the volume of a sphere, and m^* is the effective mass of a sphere due to the buoyancy of the sphere.

Practically, random thermal fluctuation always exists due to the thermal energy ($\sim k_B T$) of a sphere. It is important to study the relation between thermal motion and sphere diffusion to understand the passive microrheology method that will be discussed. The mean-square fluctuation of the sphere in a purely viscous fluid in two dimensions $\langle r^2 \rangle$ is defined as [57]:

$$\langle r^2 \rangle = 4Dt \tag{2.7}$$

The diffusion coefficient (D) of the sphere can be calculated after tracing its displacement and can be applied to calculate the viscosity of the fluid. The diffusion coefficient is inversely proportional to the friction factor, which also depends on the viscosity of the fluid. From Stoke's equation, the friction factor (f) is given by:

$$f = 6 \pi \eta a \tag{2.8}$$

The relation between the diffusion coefficient and the friction factor is described as:

$$D = \frac{k_B T}{f} \tag{2.9}$$

Thus, Stokes-Einstein relationship [58] can describe the viscosity of a fluid by combining these equations.

$$D = \frac{k_B T}{6 \pi \eta a} \qquad \eta = \frac{k_B T}{6 \pi D a} \tag{2.10}$$

These results assume that the sphere has no interaction with other spheres in a medium and is infinitely far from the wall or substrate. In addition, the types of applied external force can vary with experimental methods, and the external forces are usually the

most dominant forces on the probe sphere in materials. When the applied external force is larger than those forces from thermal fluctuation and gravity, the particle motions will be governed by the applied external forces and the drag force in the fluid.

2.2.3 Rheological response measurement

Most polymer coatings show the viscoelasticity. The main phenomenon that distinguishes viscoelastic materials from purely viscous liquid and elastic solid is stress relaxation over a time [59]. The response to applied stress can differ for each type of material. Figure 2.3 (b) shows the stress (τ) versus time (t) of the Hookean solid for a step input in strain γ (Figure 2.3 a). It shows no stress relaxation, while the Newtonian liquid shows stress relaxation to zero immediately when the strain becomes constant (Figure 2.3 c). However, the stress in viscoelastic solid reaches asymptotically an equilibrium stress τ_e after a significant time, while the stress in viscoelastic liquid relaxes to zero (Figure 2.3 d).

The stress relaxation modulus G is given by :

$$G(t) = \frac{\tau(t)}{\gamma} \tag{2.11}$$

This linear dependence is called linear viscoelasticity. When a strain is larger than a critical strain ($\gamma > \gamma_c$), the relaxation modulus becomes not only a function of time but also of strain, as shown in Figure 2.4.

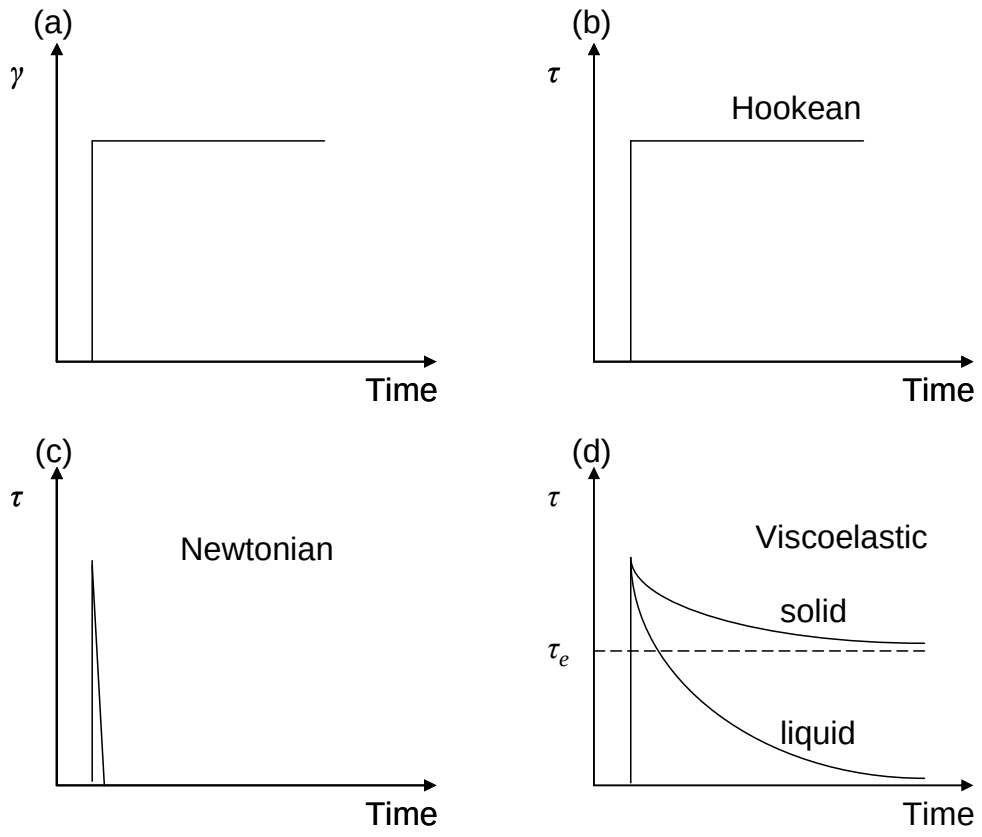

Figure 2.3 Stress response vs time for (a) strain γ in (b) Hookean solid, (c) Newtonian fluid, and (d) viscoelastic solid and liquid [6].

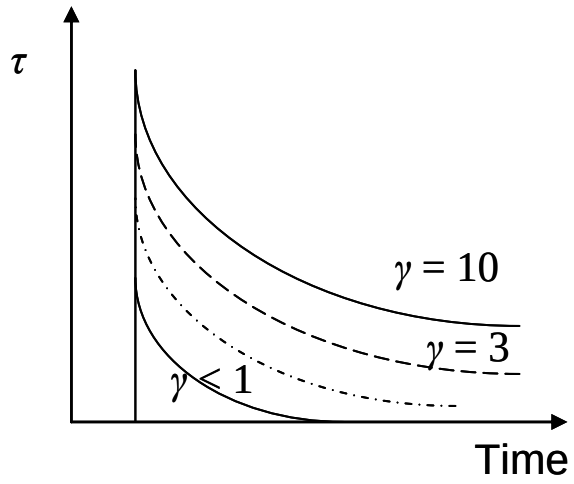

Figure 2.4 Stress relaxation data for a polydimethylsiloxane. Stress decays exponentially, and the decay rate strongly depends on the strain γ [6].

The non-linear viscoelastic behavior can be described as:

$$G(t,\gamma) = \frac{\tau(t,\gamma)}{\gamma} \tag{2.12}$$

These viscoelastic responses of materials can be characterized by conventional bulk rheology methods that are analogous to microrheology methods. Non-linear behaviors of materials are characterized by constitutive equations appropriate for the materials [6].

It is useful to apply sinusoidal strain to the material and measure its corresponding linear rheological response [6]. When shear strain is applied to the material as a function of time and frequency ω, the corresponding stress oscillates sinusoidally at the same frequency but will be shifted by phase angle δ.

$$\gamma = \gamma_0 \sin \omega t \qquad \tau = \tau_0 \sin(\omega t + \delta) \tag{2.13}$$

where γ_0 and τ_0 are constant strain and stress respectively. Then, the stress can be decomposed by two phases.

$$\tau = \tau' + \tau'' = \tau_0' \sin \omega t + \tau_0'' \cos \omega t \tag{2.14}$$

The storage or elastic modulus that is in-phase with the strain is

$$G' = \frac{\tau_0'}{\gamma_0} \tag{2.15}$$

Then, the loss modulus that refers to the energy dissipated in the material

$$G'' = \frac{\tau_0''}{\gamma_0} \tag{2.16}$$

Combining Equations (2.15) and (2.16), the loss angle (δ) is

$$\tan\delta = \frac{\tau_0''}{\tau_0'} = \frac{G''}{G'} \tag{2.17}$$

The dynamic viscosity of materials can be characterized the relation between the out-of-phase stress (τ''_0) and strain rate ($\dot{\gamma} = d\gamma/dt = \gamma_0\omega \cos \omega t = \dot{\gamma}_0 \cos \omega t$)

$$\eta' = \frac{\tau_0''}{\dot{\gamma}_0} = \frac{G''}{\omega} \tag{2.18}$$

Similarly, the elastic part of the dynamic viscosity is

$$\eta'' = \frac{\tau_0'}{\dot{\gamma}_0} = \frac{G'}{\omega} \tag{2.19}$$

Thus, complex viscosity is defined as [6]:

$$|\eta^*| = (\eta'^2 + \eta''^2)^{1/2} = \left[\left(\frac{G''}{\omega}\right)^2 + \left(\frac{G'}{\omega}\right)^2\right]^{1/2} = \frac{1}{\omega}|G^*| \tag{2.20}$$

The viscosity in Equation (2.18) at the zero frequency limit ($\omega \rightarrow 0$) is equal to zero shear rate limit of the conventional bulk viscosity ($\eta = \eta(\dot{\gamma}) \ \dot{\gamma} \rightarrow 0$). This oscillation stress/strain experiment can be carried out using active microrheology methods with the magnetic manipulation and optical tweezer systems. Details of these measurements are discussed in Section 2.2.4.

2.2.4 Active and passive microrheology methods

Microrheology methods use micron-sized particles as probes for local rheological measurements. Presently, there are two broad classes in microrheology methods; one uses the active manipulation of probe particles by the local application of stress, and the other uses passive thermal fluctuating probe particle motion [60].

Active microrheology involves the active manipulation of probe particles using magnetic or electric fields and mechanical force. This method can be applied to measure rheological properties of both soft and stiff materials. Sufficient external force can be applied to strain the materials beyond the linear viscoelastic regime in order to measure a wider range of responses. Since this method requires external stress to the samples,

additional equipments to generate external force on the probes are necessary. There are several active methods that use different experimental set-ups to apply adequate external forces to probes. The schematic representations of several active microrheology methods are illustrated in Figure 2.5, and compared in Table 2.1.

Magnetic manipulation is one active microrheology category. The schematic representation of this method is illustrated in Figure 2.5 (a). It uses strong magnets as external force sources and magnetic spheres as probes for viscosity characterization, with the optical microscope used for probe particle tracking. Since the external magnetic field from the magnet traps the magnetic probe particles and manipulates their motion, this method is also called the *'magnetic tweezer'*. The external magnetic force on magnetic probe particle is defined as [61, 62]:

$$F_m(t) = M(t)_{moment} V \frac{dB}{dx} = \chi B(t) V \frac{dB}{dx} \tag{2.21}$$

where $M(t)_{moment}$ is the induced magnetic moment of the magnetic particle, V is the volume of the magnetic particle, χ is the susceptibility of the particle, $B(t)$ is the strength of the applied magnetic field and dB/dx is the magnetic field gradient generated from the magnet.

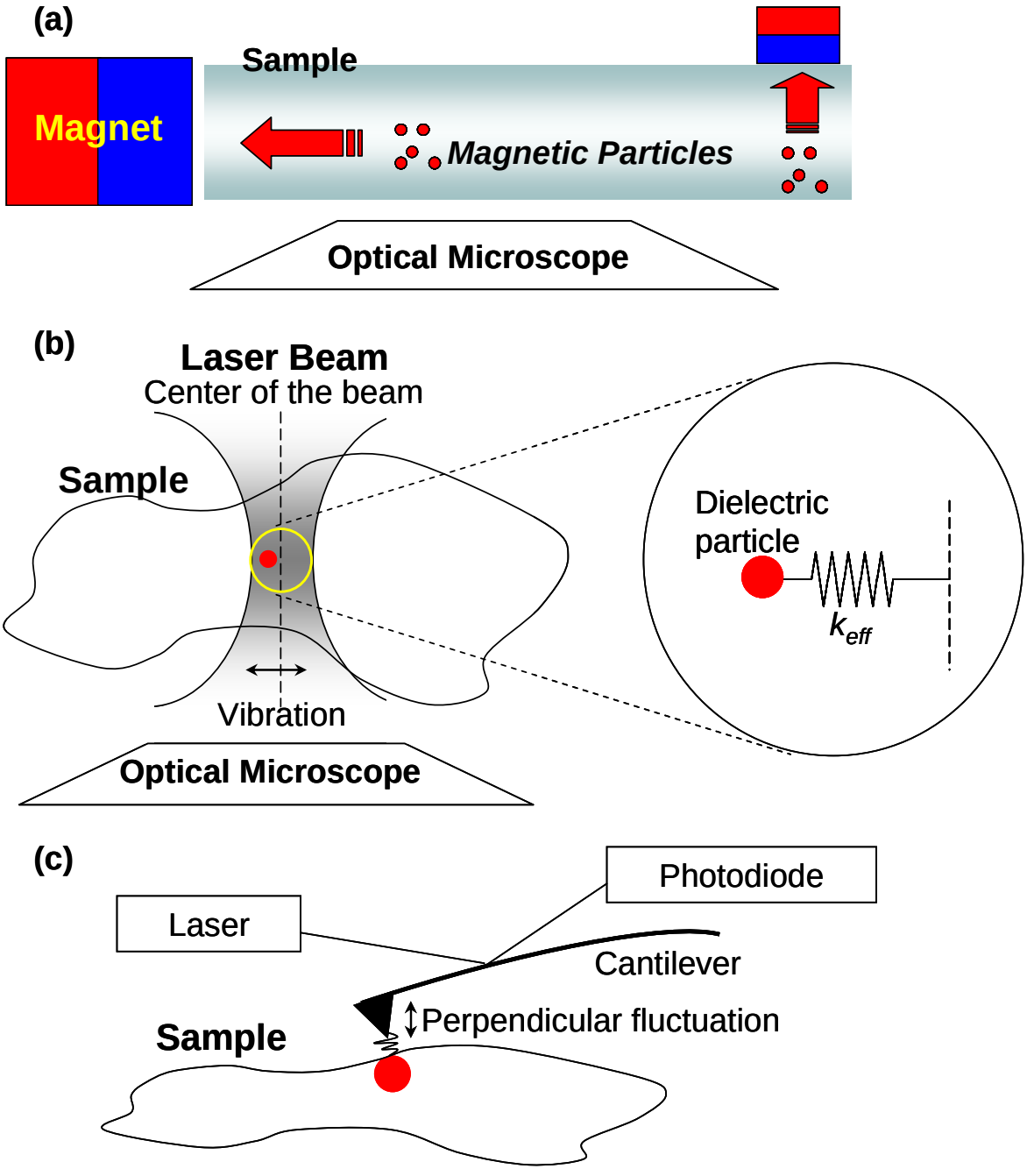

Figure 2.5 Schematics of (a) magnetic manipulation method, (b) optical tweezer, and (c) atomic force microscopy.

The motion of the magnetic sphere in a fluid can be governed by two dominant forces, such as a magnetic force and a drag force, if the spheres are in highly viscous Newtonian solution under strong magnetic force. Therefore, the motion of a sphere with radius *a* in a fluid is described by the balance of the magnetic force and drag force.

$$m\frac{d^2x}{dt^2} = F_m(t) + F_{drag}(t) = \chi B(t)V\frac{dB}{dx} + 6\pi\eta a\frac{dx}{dt} \tag{2.22}$$

It is shown that the viscosity of the fluid can be determined by the sphere velocity under constant magnetic force on the sphere [61, 62].

$$\eta = \frac{\chi BV(dB/dx)}{6\pi a v_p} \tag{2.23}$$

In addition to this constant force viscometry, another way to measure the rheological properties of materials is to apply the frequency dependent magnetic force. As shown in Figure 2.6, an oscillatory force can be applied to the sphere with an electromagnet system. The amplitude and phase shift of the sphere displacement can be measured and used to determine the frequency-dependent viscoelastic modulus. The displacement of the sphere is $x(t) = x_0 \exp[i(\omega t - \delta)]$ under an oscillatory force $f_m(t) = f_0 \exp(i\omega t)$. Thus, the shear moduli are defined as:

$$G'(\omega) = \frac{f_0}{6\pi a|x_0\omega|}\cos\delta(\omega) \qquad G''(\omega) = \frac{f_0}{6\pi a|x_0\omega|}\sin\delta(\omega) \qquad (2.24)$$

For those viscoelastic response measurements, several different configurations have been developed to manipulate probe magnetic particles with different numbers (1, 2, 4, 6, 8 or more) of magnet pole pieces and with different types of magnets (permanent and electromagnets) [61, 63-66]. Typically, two-pole systems have been widely used to generate constant force on the probe spheres. Single and multi-pole systems have been used to generate oscillatory and rotational forces on the probes in order to measure time or frequency dependent rheological properties.

Permanent magnet configuration can generate strong constant force on the magnetic sphere instead of generating time dependent force, but it lacks the versatility of the probe particle manipulation ways [67]. However, the electromagnet configuration can generate various types of force, such as constant, oscillatory, and rotational on the magnetic sphere by adjusting the electric current on the coils [68]. Since it uses a high electric current, complex feedback control between the current and the generated magnetic field is required due to the considerable magnetic field hysteresis of magnet cores. A cooling system is also necessary due to the substantial heating from high current [67]. Despite the drawbacks of both permanent and electromagnetic configuration, magnetic manipulation methods offer many advantages, such as uniform force on large area in the sample, no damage to samples, and various ways to manipulate the probes, as summarized in Table 2.1.

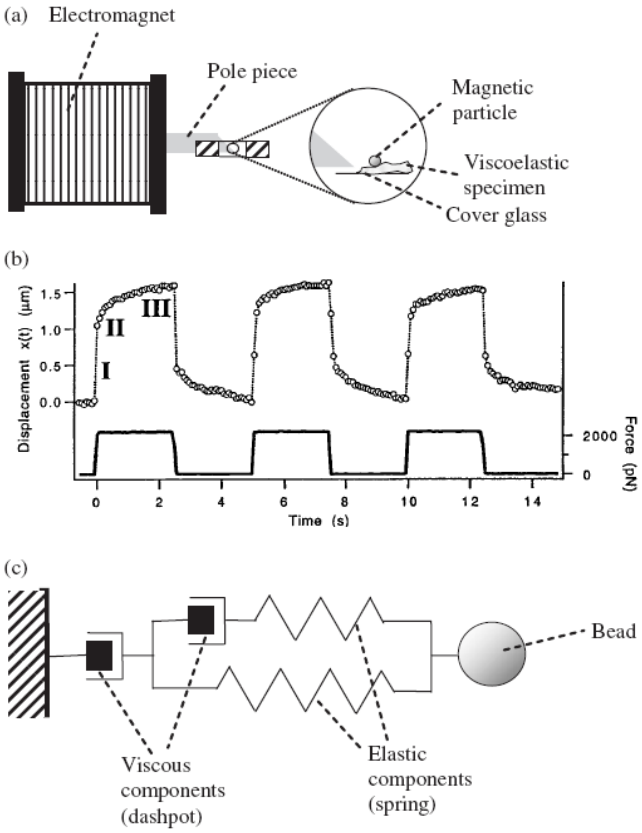

Figure 2.6 Microrheology experiment with oscillatory magnetic force. Schematic diagram of (a) experimental set up, (b) the applied magnetic field and the particle response, and (c) the equivalent viscoelastic model for the system [63].

Table 2.1 Comparison of microrheology methods [51, 67, 68].

	Magnetic tweezer	Optical tweezer	AFM
Force (pN)	$10^{-2} \sim 10^{4}$	0.1 ~ 200	$10 \sim 10^{4}$
Frequency (Hz)	$10^{-2} \sim 10^{3}$	$10^{-2} \sim 10^{6}$	$10^{-1} \sim 10^{4}$
Damages from heating or contact	No	Yes	Yes
Constant force area	Large	Very small	Small

Another active microrheology method, called the *'optical tweezer'*, uses a highly focused laser beam to trap and manipulate dielectric probe particles. As shown in Figure 2.5 (b), this laser has a strong electric field gradient at the narrowest point of the beam, so the dielectric probe particle is attracted along the gradient to the strongest electric field point at the center of the beam; hence, it can become trapped in the focused beam. For small displacements (~150 nm), the trap acts like a linear spring with an effective spring constant k_{eff} that depends on the polarizability of the probe particle and the intensity of the beam [69]. Forces on the probe up to ~100 pN can be generated by moving the focused beam to apply local stress to materials. Then, the local rheological responses can be probed from the resultant particle displacement [70].

The optical tweezers microrheology method allows for high frequency measurements; it can also accurately resolve the small displacement of the small probe. However, it has several drawbacks, including local heating and force limitations [67, 71]. The high intensity of the focused beam can generate local heating within the material. Local heating influences the viscosity of materials; therefore, samples are limited to those that are not susceptible to photodamages. Moreover, the generated force is limited to the pico-newton range, so it cannot be utilized to characterize highly viscous materials.

In addition, the active manipulation method can employ the use of AFM to probe micro-mechanical responses. AFM with soft cantilever has been used in tapping mode for both imaging and elastic modulus measurement. The schematic diagram of the AFM active microrheology method is illustrated in Figure 2.5 (c). The deflection of a cantilever is

measured with reflected laser beam detection using a photodetector. The cantilever tip vibrates close to the surface of samples; therefore, the bottom of the tip taps the surface.

The viscosity of the sample can be measured by oscillating the tip normal to the sample surface [72]. An amplitude sinusoidal signal $\tilde{\delta}$, of the oscillating cantilever tip was applied normal to the surface at frequency of 20 ~ 400 Hz. The probe that has oscillating amplitude $\tilde{\delta}$ deformed the sample with the initial indentation depth δ_o. Then, the cantilever responded with a phase-shifted signal. In this case, the modified Hertz model describes the frequency dependent response. For small (5 ~ 20 nm) oscillation, the force is:

$$f \approx \frac{4}{3}\sqrt{R}(\hat{E}_o\delta^{3/2} + \frac{3}{2}\hat{E}^*\sqrt{\delta_o}\tilde{\delta}) \tag{2.25}$$

where R is the radius of a spherical tip, $\hat{E}^*$ is the complex longitudinal modulus, and $\hat{E}_o$ is the zero-frequency value of $\hat{E}^*$. However, a hydrodynamic impact on the cantilever also exists during the oscillation at viscous medium. Since it depends on the oscillation frequency ω and viscosity that influences the oscillation amplitude constant α, the drag force is defined as:

$$f_{drag} = i\omega\alpha\tilde{\delta} \tag{2.26}$$

Then, the complex modulus $\hat{E}^*$ can be determined using the corrected applied force f_c by subtracting f_{drag} from f [73]:

$$\hat{E}^* = \frac{1}{2}\frac{f_c}{\tilde{\delta}\sqrt{\delta_o R}} \tag{2.27}$$

Therefore, this AFM experiment has the issue of coupling viscoelasticity of the sample with the hydrodynamic interaction of cantilever at the surface. A number of different methods for more precise quantitative measurement are being investigated [74].

The other class of methods is passive microrheology method that uses the thermal Brownian motion of probe particles to measure the rheological properties of soft materials. It measures the response of the probe to thermal energy (~k_BT). Since the method uses thermal energy of embedded probe particles, the materials should be soft enough to be deformed by the weak stress. The steps for tracking particles using image software are illustrated in Figure 2.7. The mean-square displacement (MSD) of the fluctuating probe is calculated after imaging of particle motion. Next, the data is transformed to rheological functions.

The MSD of the probe in *n* dimensions is proportional to the diffusion coefficient *D* and time *t* in a pure viscous medium [57]. The correlation between MSD and *D* from the diffusion equation is

$$\left\langle \Delta r^2(t) \right\rangle = 2nDt \tag{2.28}$$

Therefore, the viscosity η of the fluid surrounding the probe can be obtained using Stokes-Einstein equation:

$$\eta = \frac{k_B T}{6\pi a D} = \frac{2ntk_B T}{6\pi a\left\langle \Delta r^2(t)\right\rangle} \tag{2.29}$$

The passive microrheology method is generally used to measure the linear rheological response of materials due to the small applied stress to samples.

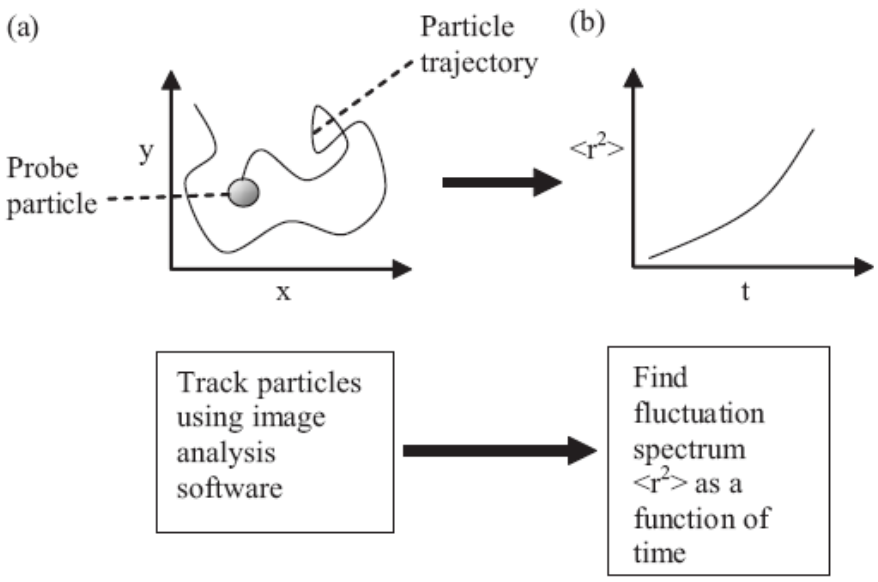

Figure 2.7 Experimental steps for the particle tracking method. (a) Particle trajectory in x-y plane measured and (b) the average fluctuation spectrum vs time plotted (b) [51].

2.3 Confocal Raman Microscopy

Raman spectroscopy has been used to analyze the structure of materials in many applications across the fields of biology, chemistry, pharmacology, and materials science. It is generally non-destructive and non-invasive, and can be applied to many types of samples (solid, liquid or gas) with minimal or no sample preparation. The method combined with the capability to confocal analysis, confocal Raman microscopy, is suitable for the characterization of the microstructure evolution in thin films, which requires micron-level spatial resolution. This section provides an overview of confocal Raman microscopy with basic principles and experimental results for drug imaging in drug-polymer coatings.

2.3.1 Overview

Confocal Raman microscopy, integrated with an optical microscope, a confocal aperture, an excitation laser system and a detector, uses the spectra based on the inelastic scattering of photons in the laser light upon interaction with molecules. The spectra generally contain sharp characteristic bands of specific molecular bonds. The intensity of the bands is proportional to the concentration of the molecules in the sample; therefore, it can be used for quantitative analysis [75]. One of the key functions of the technique is the chemical mapping of a sample. The obtained spectra information is used for quantitative imaging of components distribution in the sample. There are several ways of chemical mapping by moving the sample stage or optical microscope during measurements. Two

dimensional mapping can be carried out using multiple line scans in the X-Y or X-Z plane. Lateral areas (X-Y plane) are captured in a given depth or on a surface, while the depth profiling (X-Z plane) is completed through the sample thickness due to the high spatial resolution and non-destructive characteristics of the method. In addition, three dimensional image of component distribution can also be constructed using multiple scans of both lateral and depth profiling.

This technique has been shown to be capable of analyzing various materials and devices in diverse areas of both industry and academic research. Recently, it has been widely applied to biomaterials and pharmaceutical researches due to several advantages over other techniques, such as sharp image quality, high sensitivity and spatial resolution, no sample preparation, and non-destructive nature [76]. In confocal Raman microscopy for biological and pharmaceutical specimens, a near infrared laser source has been used to reduce the damage within the microscopic regions of the specimen during Raman spectra collection [77]. Due to these advantages, the method has been used to monitor biochemical change in cells over time during its life cycle [78]. In addition, the characterization of structure evolution of the active components within coatings of medical devices, such as drug eluting stents has been tried to provide superior product quality control for more practical pharmaceutical industry applications [12]. However, it is still challenging to acquire high resolution of chemical mapping during structure evolution for these researches. Therefore, a new approach for real-time monitoring of the structure evolution of these specimens needs to be developed for further application of confocal Raman microscopy.

2.3.2 Basic principles

When a sample is irradiated with monochromatic light, the incident light can be transmitted or scattered. Most of the light passes through the sample, however, a small portion of the light is scattered. The majority of the monochromatic light is scattered by the sample at the same frequency as that of the incoming light, known as elastic scattering, while a small amount of the incoming light is scattered inelastically. The inelastic scattering means that the frequency of photons in monochromatic light changes upon interaction with a sample. "Raman effect", experimentally discovered in 1928 by C.V. Raman, is the frequency shift of the re-emitted photons when the sample interacts with the monochromatic light. It is based on the distortion of electron cloud (induced dipole moment) due to the oscillating electric field in the incident light. Molecules consist of periodical atomic bonds which vibrate continuously with different frequencies. The vibrational frequency depends on the size and the electronegativity of the atoms in the bond [76]. These vibrations also result in a distortion of the electron cloud. Due to the periodical distortion, molecules start vibrating with characteristic frequency.

Figure 2.8 shows energy levels in different forms of scattering. The interaction of light with a molecule causes an excitation to a virtual energy state. The virtual energy state is extremely short-lived, and the molecules return to lower energy states. When it returns back to its initial state, the re-emitted photon has the same frequency as that of the incident light; therefore, the scattering is called elastic or 'Rayleigh scattering' (Figure 2.8 a). Rayleigh scattering of sunlight by the molecules of the atmosphere causes the blue color of the sky or the redding of the setting sun due to its strong wavelength dependence.

Most of the incident photons return to the initial state (i.e., undergo elastic scattering), however, this type of signal is not useful for molecular characterization [75].

Molecules are excited to the virtual state and transformed into oscillating dipoles by an irradiated monochromatic light with a given frequency. A small proportion of the scattered light (< 1 %) undergo inelastic scattering due to the interaction of the incident photons with the vibrational energy levels, shifting the frequency of incident photon. This effect is weak due to the low probability of Raman scattering. The interaction involves the energy exchange between the photon and the molecule, and it is expressed as:

$$\Delta E = h\nu_0 - h\nu_1 = h\Delta\nu \tag{2.30}$$

where h is the plank constant, v_0 and v_1 are the frequencies of the incident and scattered photons, respectively, E_0 and E_1 are initial and final energy states, and $\Delta\upsilon$ is frequency shift. There are two types of Raman scattering: Stokes scattering and anti-Stokes scattering. Stokes scattering occurs if the energy is absorbed from the incident light upon the interaction between the photon and the molecule. The frequency of scattered light is reduced due to the energy absorption (Figure 2.8 b). On the other hand, anti-Stokes scattering occurs when the molecule is in the excited vibrational state and returned to the ground state from the virtual energy state, resulting in the higher frequency (Figure 2 c). Since Stokes scattering bands are more intense than the anti-Stokes bands, it is typical to use Stokes scattering for Raman spectroscopy. However, the intensity of Stokes

scattering is 10^7 times smaller than that of Rayleigh scattering (no energy exchange between the incident photon and the molecule); therefore, it is required for high-quality Raman spectra to reduce the strong Rayleigh scattering using adequate instruments, such as filters and apertures [76].

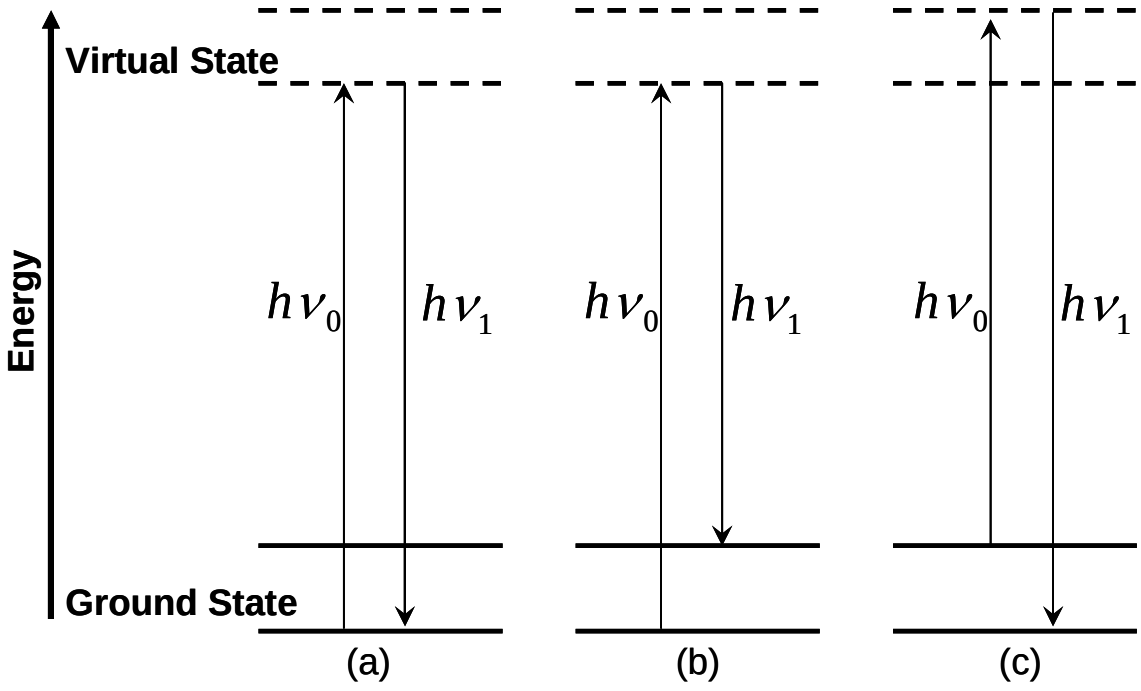

Figure 2.8 Schematic representation of (a) Rayleigh scattering, (b) Stokes scattering, and (c) anti-Stokes scattering.

Chapter 3. Design of Magnetic Microrheometer*

3.1 Introduction

Liquid-applied coatings are used to modify and protect surfaces, enhance functionality, and create single and multilayer products and devices. In the coating process, a liquid, such as a polymer solution or neat monomer, is applied onto a substrate and then solidified, typically by drying or curing, into a functional solid coating. Initially, the coating liquid viscosity must be low enough for deposition onto the substrate and surface leveling. Viscosity increases as the coating transforms to a final solid state; however, there may be a transient decrease in viscosity, initially, depending on the heating rate and temperature used [36, 37, 79]. The viscosity may also vary through the coating thickness due to gradients in solvent concentration or extent of reaction [5, 15]. Surface wrinkles can be generated if the skin swells from solvent or monomer beneath [11]. Characterization of the local viscosity of the coated layer as it transforms from liquid to solid would be useful for designing improved solidification processes and preventing defects.

Several attempts have been made to measure the rheological properties of coatings. Empirical routes employ a rolling ball on the surface of a coating [80]. Researchers have also studied the rheology of a coating liquid as a function of drying or

* A portion of this chapter has been published as: Jin-Oh Song, Robert M. Henry, Ryan M. Jacobs, and Lorraine F. Francis, Magnetic microrheometer for in situ characterization of coating viscosity, Review of Scientific Instruments, 81, 093903, 2010.

curing time without deposition on a substrate. Conventional rheometers have been used with specially designed fixtures, such as modified plates [37], T-bars [33], and torsional braids [81], to capture dynamic changes in thin layers of coating liquids. While these methods provide useful information, they do not characterize the local viscosity in a coating and they are inherently destructive.

Magnetic microrheology is well-suited to the investigation of local rheological properties in coatings. In this technique, micron-sized magnetic particles are used to probe local viscosity under an applied magnetic field [51]. For coatings, these probe particles can be placed in the coating and monitored as a function of time and particles at different positions within coating can be tracked. The magnetic method offers advantages over other microrheology techniques: a wider range of forces, no damage to the specimen by contact or heat, and smaller probes [67]. Therefore, magnetic microrheology has the possibility of providing *in situ* data over a wide range of local viscosity in a nondestructive manner.

Magnetic microrheology techniques have been widely used to characterize rheological properties of small volumes of soft materials. Permanent magnet setups generate strong and constant force on the magnetic probe particles [67]. Electromagnet configurations generate various forces on the probes, including constant, oscillatory, and rotational, depending on the magnitude and frequency of electric current on the coils, the gap between the poles, and the number of pole pieces [61, 64-66, 82, 83]. Much of the previous work has focused on manipulating probe particles in soft biomaterials [61, 64-

66, 82], colloidal dispersions [84], and polymers [30, 54, 85]. For studying the changes in viscosity of liquid applied coatings, a new magnetic microrheometer set-up is needed.

The apparatus described in this chapter is capable of characterizing the change in viscosity of a coating during solidification as well as the spatial gradients of viscosity. Permanent magnets are used to generate magnetic force on probe particles and a 3-D digital microscope is used for particle tracking. The microscope provides a sufficient working distance for the magnet placement while maintaining high resolution and low depth of field (DOF). In addition, there is a sample stage with controlled heating and a gas flow system that mimics industrial solidification processes.

3.2 Basic Theory

The motion of a magnetic probe particle in a liquid is affected by several forces: magnetic, fluid drag, gravity, particle-particle interaction, and thermal fluctuations. These forces are balanced by inertia [51]:

$$F_m + F_{drag} + F_g + F_{\text{int}} + F_{thermal} = m\frac{dv}{dt} \tag{3.1}$$

where F_i are force terms defined below, m is the particle mass and v is the particle velocity. Particle-particle interaction (F_{int}) is negligible at dilute particle concentration (< 10^{-4} vol.%) [61, 83]. In addition, inertia ($m\ dv/dt$) can be ignored when the Reynold's number is much lower than unity. If the applied magnetic force (F_m) is much stronger compared to the gravitational force (F_g) and thermal fluctuations ($F_{thermal}$), omitting F_g and $F_{thermal}$ results in less than 1 % error. For example, the displacement of a 1 μm diameter particle under a strong magnetic force (F_m ~10 pN) is 100 ~ 1,000 times greater than the displacements from sedimentation (F_g ~10^{-2} pN) and thermal fluctuation. Therefore, the particle motion is governed by two dominant forces, the magnetic force and the drag force (F_{drag}).

$$F_m + F_{drag} = 0 \tag{3.2}$$

The magnetic force on a spherical magnetic particle with magnetization M and radius R in a magnetic field gradient dB/dx is ,

$$F_m = \frac{M}{\mu_0}\left(\frac{4\pi R^3}{3}\right)\frac{dB}{dx} \tag{3.3}$$

where μ_0 is permeability of free space. The drag force acts in the opposite direction of F_m and is given by

$$F_{drag} = -6\pi\eta R v \tag{3.4}$$

where η is the liquid viscosity. This relation assumes that the coating liquid is Newtonian. In this case, the force balance equation allows the viscosity of coating liquids to be determined from the measured probe particle velocity under an applied magnetic field.

A constant terminal velocity of spherical particle can be used to calculate the viscosity of the medium [86]. Thus, it is important to predict the time to reach its terminal velocity and its dependence on the viscosity and magnetic force. The time versus the velocity change of the magnetically saturated particle (M = 0.1 T) in coatings is plotted in Figure 3.1. The velocity of the magnetic particle with radius 0.5 μm under a given magnetic field gradient approaches the terminal velocity very quickly. For example, a magnetic particle that has M of 0.1 (T) in water (η = 0.001 Pa·s) reaches its terminal velocity (v_t) after 10^{-6} sec. in Figure 3.1 (a), and the time required to reach the terminal velocity decreases as the viscosity of the coating increases as shown in Figure 3.1 (b), (c), and (d). Since the particle reaches its terminal velocity very quickly in every case, the measured velocity during the experiment can be equal to the terminal velocity. Therefore,

the viscosity of coatings can be simply determined by the measured particle velocity that is equal to the terminal particle velocity during the motion, and they are described by :

$$v_t \approx v = \frac{2MR^2 (dB/dx)}{9\mu_0 \eta} \tag{3.5}$$

$$\eta = \frac{2MR^2 (dB/dx)}{9\mu_0 v} \tag{3.6}$$

Assuming a low particle velocity , the shear rate [86, 87] ($\dot{\gamma} \approx v/2R$) in microrheological experiments is low enough for the Newtonian assumption to be valid for many coating liquids. For non-Newtonian liquids, the drag force (Eq. (4)) needs to be modified [87]. Likewise, modification is needed when significant interaction between the sphere and liquid, as would be expected if the probe particle were on the same size scale as structural features in the liquid [51].

As shown in Equation (3.4) and Figure 3.2 (a), v_t decreases with increasing viscosity. The velocity of the particle will drop dramatically during the drying process since the viscosity of coatings generally increases during the process. The viscosity measurement time during the particle motion must be much less than the time-scale that viscosity changes during the drying process in order to analyze the viscosity changes as a function of drying time. Therefore, it is necessary to have a sufficient particle velocity to measure the viscosity changes of coatings. Faster particle motions will be beneficial to measure local viscosity change during the drying process more precisely, especially in a high viscosity range.

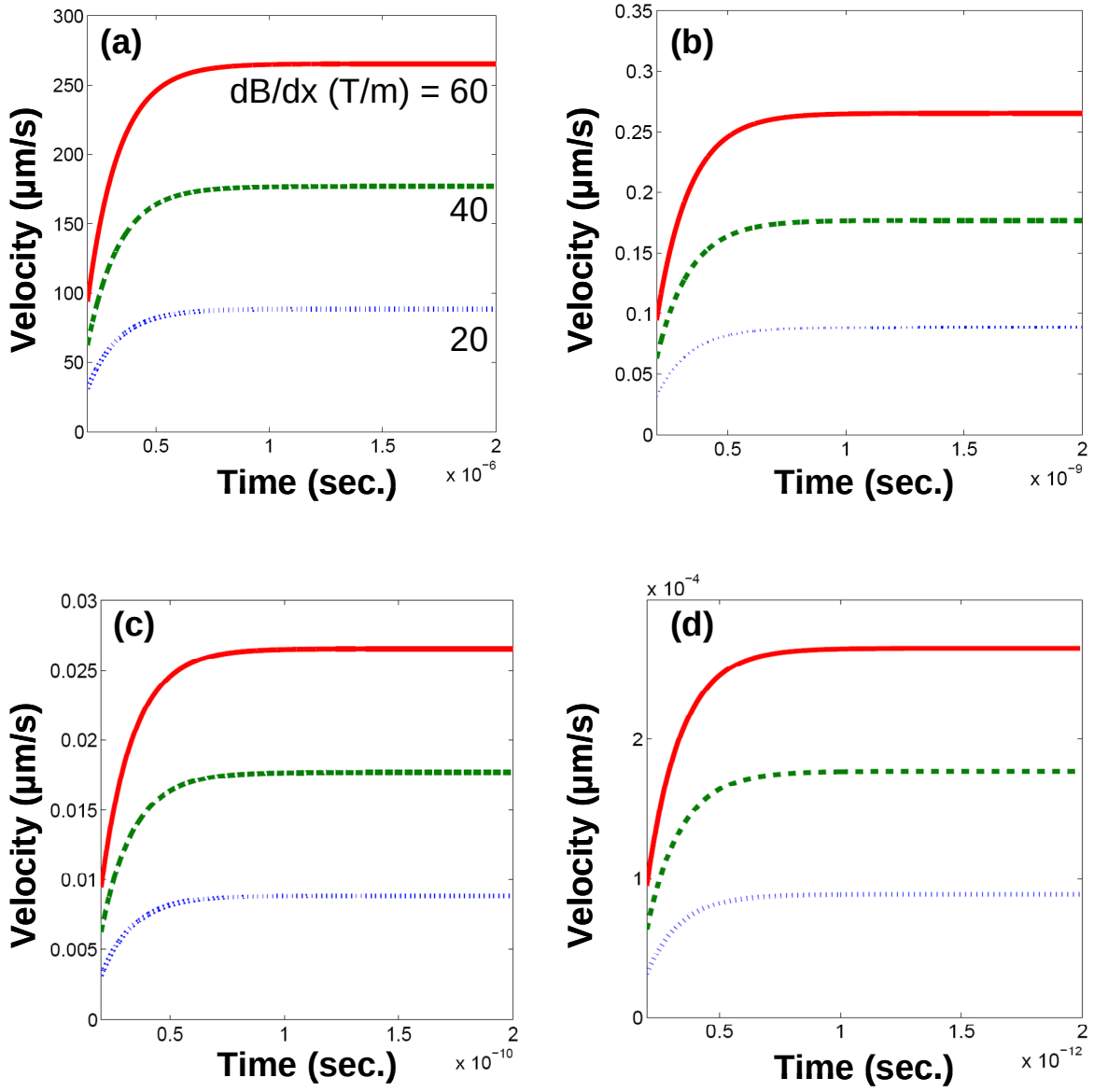

Figure 3.1 Particle velocity vs time under different magnetic filed gradient (T/m) (60 : solid line, 40 : dashed line, and 20 : dotted line) within coating solutions with different viscosities of η = (a) 0.001, (b) 1, (c) 10, and (d) 1,000 (Pa·s).

The dependence of the particle velocity on the magnetic field gradient and the particle size in a given coating with η = 10 Pa·s is shown in Figure 3.2 (b). The velocity of the magnetic particle mainly depends on the magnetic field gradient, the magnetization of the particle, and its volume. Since the particle velocity increases linearly with the magnetic field gradient, it is required to build and design a proper permanent magnet or electromagnet manipulation system to generate a higher magnetic field gradient for more accurate and faster measurements. The most dominant factor on the particle velocity is the radius of the probe particle (R). Since the particle velocity is proportional to R^2, a higher velocity can be achieved simply by the selection of bigger probe particles. However, the coating thickness (t_d) must be considered for the selection of the probe particle. Smaller probe particles (R < 1 μm) are required to determine local viscosity in thin coatings (t_d < 10 μm) while bigger particles are required for timely measurements of highly viscous materials. Therefore, it is necessary to consider both the wet and final coating thickness and the magnitude of the coating solution viscosity for the ideal selection of the probe size. Finally, the selection of high magnetic moment materials, such as Fe_3O_4, SmCo or NdFeB for the probe magnetic particle will be one of the ways to increase the particle velocity.

Through the theoretical study, it is estimated that the magnetic particle motion is governed by the force balance of the applied magnetic force and fluid drag force in Newtonian coating solutions. The measured velocity of the particle is equal to its terminal velocity and it is inversely proportional to the coating viscosity, which will give rise to challenges in measuring the high viscosity range during the solidification process. To

overcome the challenges, it is necessary to choose a proper magnetic manipulation method and a probe particle that has higher magnetic moment to apply strong and uniform forces on the probe particles during the measurement. The size of the probe particle needs to be chosen considering the viscosity and thickness range of coatings.

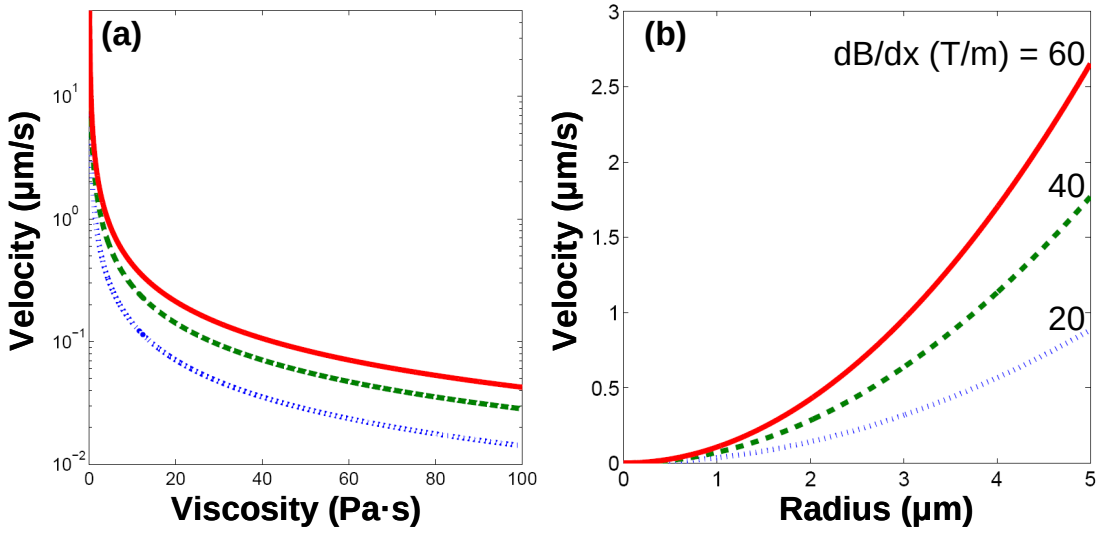

Figure 3.2 (a) The particle velocity changes as a function of viscosity of coatings for the magnetic particle with radius of 2 μm and M_s of 0.1 (T) under different external magnetic gradient (T/m) (60 : solid line, 40 : dashed line, and 20 : dotted line), and (b) the dependence on the magnetic field gradient (*dB/dx*) and the radius of the particle in the coating of which η = 10 (Pa·s).

3.3 Apparatus Design

The magnetic microrheometer was designed for the *in situ* local viscosity measurement through coating thickness. The candidate method and material to manipulate the magnetic particle appreciably in coatings are discussed for the apparatus design. The design mimics the two pole magnetic tweezers of previous studies [64, 66]. A new focusing method through the coating thickness with the apparatus using a digital optical microscope is introduced to track the particle motion in coatings. A system that can controls the temperature, heating rate, and air/gas flow is also designed to measure the effect of solidification conditions on the viscosity change within coatings.

3.3.1 Magnet configuration and magnetic probe particles

The uniformity and strength of the magnetic field and its gradient depend on the magnet properties, pole shapes and sizes, and the gap between magnets. In a single magnet configuration, smaller magnets with sharper pole tips create higher magnetic field gradients; however, these gradients are sensitive to position and hence do not provide the spatial uniformity needed for monitoring of probe particles in a coating. Better uniformity is achieved with larger, flatter magnets, but the magnetic field strength is not as high [67]. A double magnet configuration with two opposing magnets provides a better combination of magnetic field strength and gradient [66]. The strength and uniformity of the magnetic field gradient depends on the magnet properties and the gap between the magnets.

In the apparatus, two opposing cylindrical neodymium iron boron (NdFeB) permanent magnets (grade N42, K.J. Magnetics) are used. The apparatus allows mounting of different magnet sizes. In the research to-date, we have used magnets with diameters (D) of 12.7 and 25.4 mm, and lengths (L) of 25.4 and 50.8 mm. The magnetic field measured at the surface of the magnet pole ranges from 0.2 to 0.6 T, depending on the magnet dimensions. The NdFeB magnets are mounted on two stepper motors (Compumotor, NEAT) that control the gap width to a precision of 0.1 μm. The stepper motors are wired to control boxes (6K6, Parker) for communication with the operating program (Visual Basic 6.0) in the computer. A Hall probe gaussmeter (5100 series, F.W. Bell) was used to measure magnetic field strength distribution as a function of the distance from the magnet pole.

Maxwell 2-D electromagnetic field simulation (Version 3.1.04, Ansoft cooperation) was used to predict the magnitude and homogeneity of the magnetic field gradient. Simulation and experimental results for single and double NdFeB magnet (D×L: 12.7 mm × 50.8 mm) configurations are summarized in Table 3.1, and some example magnetic field distributions are shown in Figure 3.3. The magnetic field distribution between the magnets was determined. Initially, the gaussmeter was placed in contact with the center of the pole surface. Then, magnetic field strength as a function of the distance (50 μm increments) from the magnet pole surface was measured by moving both magnets laterally with stepper motors, keeping the gap between two magnets constant. The gaussmeter was stationary during the measurement. During microrheology measurements, the specimen position is also at the center of the magnet pole surface.

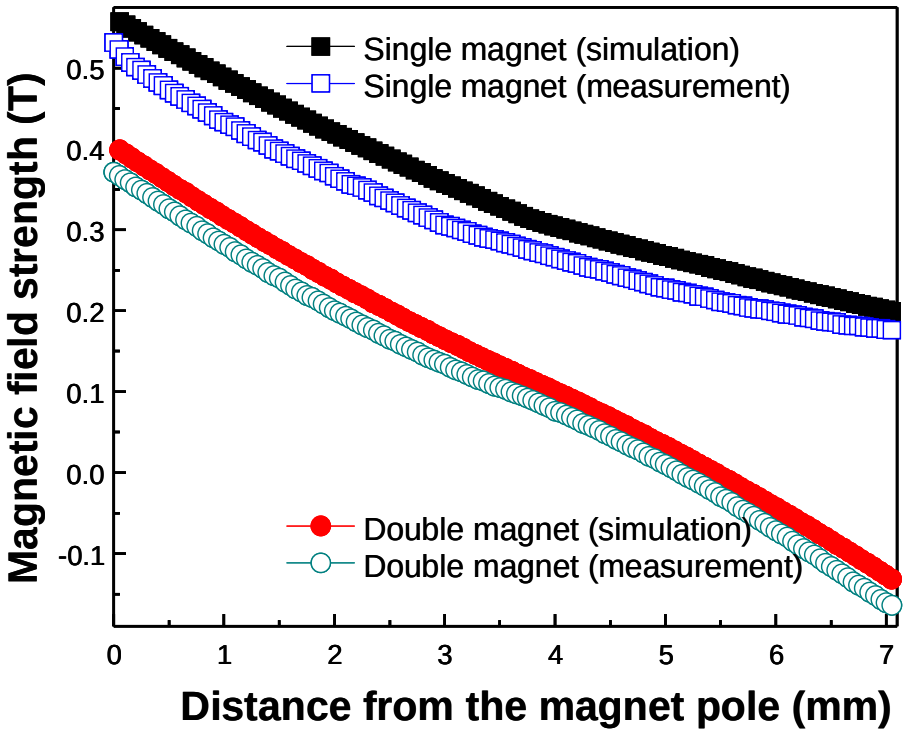

Figure 3.3 Simulation (solid) and experimental (open) results of magnetic field gradient of single magnet configuration and double magnet configuration with 10 mm gap between magnets.

Table 3.1 Predicted and measured magnetic field gradient as a function of gap between two permanent magnets.

Gap (mm)	Simulation		Measurement	
	dB/dx (T/m)	R-squared	dB/dx (T/m)	R-squared
Single Magnet	50.7	0.988	48.8	0.935
20	52.1	0.991	51.2	0.963
15	56.4	0.996	55.1	0.982
10	71.3	0.997	70.8	0.991

Data in Figure 3.3 are shown for the range of distances that are required for the experiment. Both magnetic field gradient and its linearity (R-squared) increase as the gap between the magnets decreases. The highest magnetic field gradient achieved with the double magnet configuration and the magnets used to-date is 71.3 (T/m).

Superparamagnetic Fe_3O_4 particles (MS0302, 1 μm diameter, MagSense Life Sci., Inc.) were chosen as the probe particles. Superparamagnetic particles become magnetized in a magnetic field and are nonmagnetic in the absence of the field, a quality that allows them to be dispersed in coating liquids with less likelihood of aggregation. Figure 3.4 (a) shows a scanning electron microscope (SEM) image of the spherical particles. Dynamic light scattering results showed that average particle size is 1.06 μm with a standard of deviation of 2 %; the error on viscosity calculation from the size distribution is less than 10 %. Vibrating sample magnetometer (VSM) data revealed that the saturation magnetization is 120 kA/m, as shown in Figure 3.4 (b).

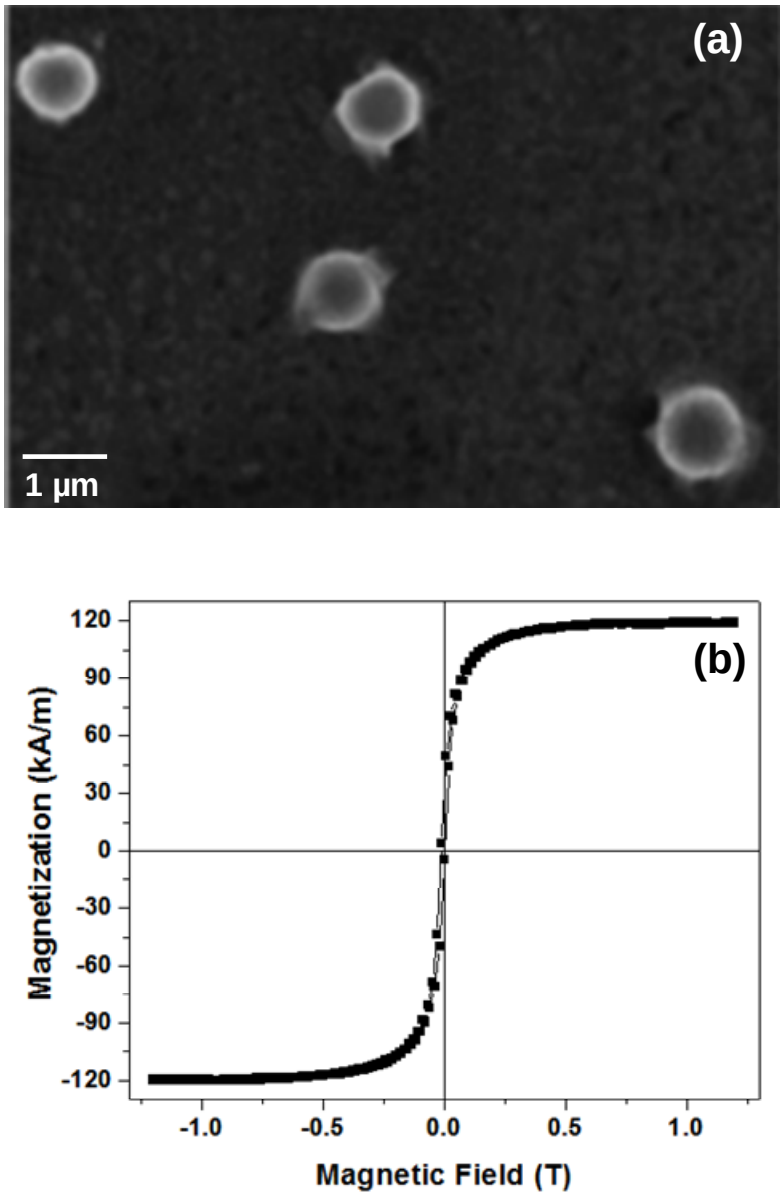

Figure 3.4 (a) SEM image and (b) magnetization curve of MS0302 probe particles.

Experiments in this research were carried out with a minimum magnetic field strength of 0.12 T to ensure that the particle reach at least 90 % of the saturated value. For fields that do not reach full saturation, the value of magnetization used to calculate viscosity was adjusted accordingly.

3.3.2 Particle imaging and data acquisition

The magnetic probe particles and their trajectories are observed with a digital optical microscope (KH-7700, Hirox-USA, NJ). This digital microscope has longer working distance than standard optical microscopes and allows magnets to be positioned next to the sample stage under the microscope. For the results shown here, we have used a lens (OL 140II) that spans magnifications from 140× to 1,400×. The maximum magnification was used for the experiments; the working distance is 1.3 cm and the depth of the field is 7.6 μm [88]. Particles at different coating depths can be tracked by focusing through the coating thickness. To facilitate this tracking, the microscope is mounted on the stepper motor (Compumotor, NEAT) for precise lens height adjustment (±0.1 μm).

To determine particle velocity, the particle positions are captured continuously at specified intervals (1 ~ 30 s). The particle-center position in each image is then tracked using Image J Plug-in (v. 1.41, NIH). Image J creates an *Image Sequence* using the continuously captured images from 3-D optical microscope system. The position of particle center is detected in each frame using *Threshold* and *Particle Tracker* features in

the software. The average velocity is determined from particle center positions in each frame and the time between the frames. This average velocity is the terminal velocity since the magnetic micro-particle reaches a constant velocity very quickly (< 1 s) in the medium, which has a viscosity within the range of 0.001 ~ 1,000 Pa·s. The average terminal velocity of the magnetic spherical particle is used to calculate the viscosity of a medium using Equation (3.6) [86].

3.3.3 Process control system

The copper sample stage is mounted on a multi-axis positioning stage (562 series ULTRAlign™ Precision, Newport) between the two permanent magnets. A heating system with temperature/process controller (CN8500, Omega) and thermocouple (type J, Omega) are connected to the sample stage (Figure 3.5 a and b). Air, or other process gas, flows from an inlet through the outlets in the stage to mimic an industrial drying process. Temperature, heating rate, air/gas flow rate and its direction can be varied. The width and length of platform for loading coating samples are 5.0 and 63.5 mm, respectively, and the width of coating samples is limited by the gap between two magnets. The maximum width of a coating sample is 15 mm.

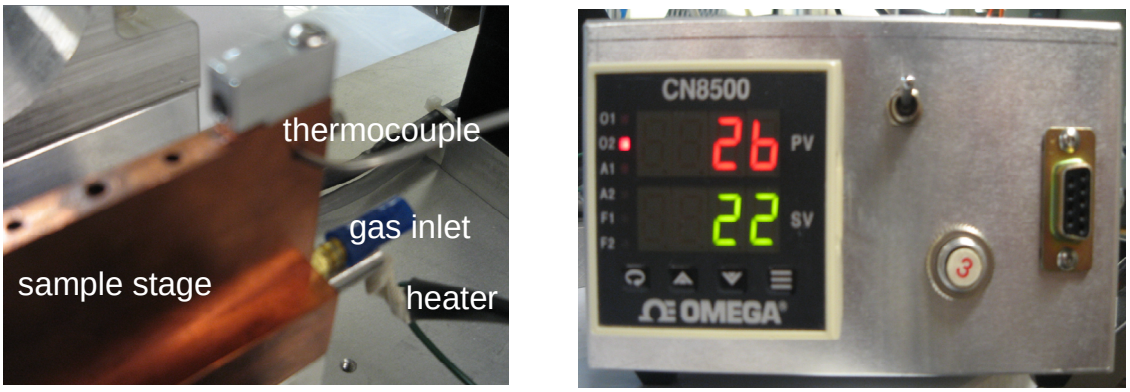

Figure 3.5 Pictures of (a) the sample stage and (b) the temperature/ heating process controller. The sample stage is connected with thermocouple, gas inlet, and heater. Gas outlets are holes in the sample stage.

3.3.4 Magnetic microrheometer

The schematic of the designed apparatus, magnetic microrheometer, is shown in Figure 3.6 (a). There are three main sections: magnetic manipulation, imaging, and sample stage with solidification system. For the manipulation of magnetic probe particles, two permanent magnets are mounted on the stages equipped with stepper motors. The magnetic field gradient depends on the magnet characteristics and can be adjusted by changing the ratio of pole diameter to the gap between the two magnets [67]. Therefore, the magnet holders have adapters for different magnet sizes and the stepper motors provide precise control of the gap between two magnets. A 3-D digital optical microscope system is used for the image/data acquisition. The microscope lens is

mounted on a stepper motor for precise lens height adjustment so that the focal plane can be changed to monitor particles at different positions through the coating thickness. For the solidification, a heating system with a temperature/process controller is connected to a copper sample stage, which has ports for adjustable air flow. Figure 3.6 (b) shows the picture of the magnetic microrheometer, and the dimensions and details of the apparatus is shown in Figure 3.6 (c).

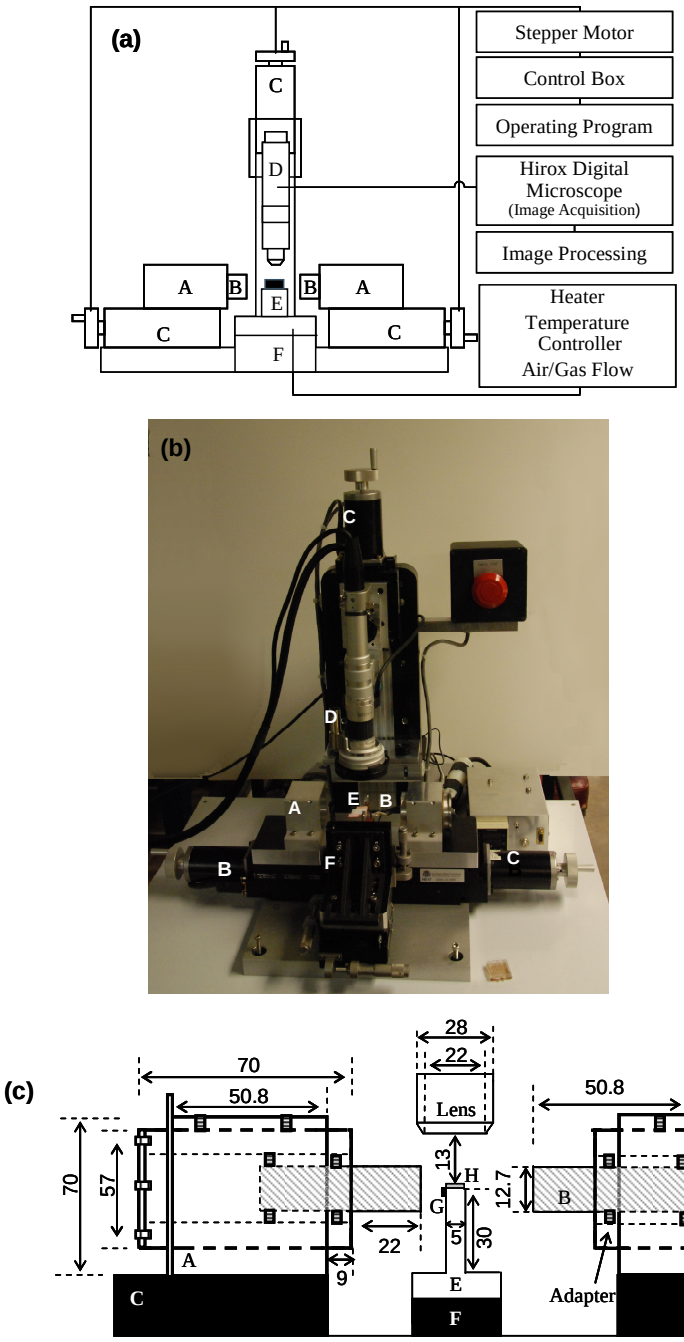

Figure 3.6 Overview of magnetic microrheometer setup, (a) schematics of the apparatus and configuration of control units, (b) picture of the apparatus, and (c) dimensions and details of magnets, magnet holders/adapters, and sample stage A: magnet holder and adapter B: NdFeB permanent magnet (D×L: 12.7×50.8 mm) C: stepper motor D: optical microscope (magnification: x140~1,400, working distance: 13 mm) E: sample stage connected to solidification system, F: micropositioner, G: Hall probe Gaussmeter, H: Clip to hold coating samples).

3.4 System Validation

3.4.1 Materials and methods

In order to validate the apparatus, magnetic particle velocities were measured as a function of time in aqueous glycerol (96.7 wt.%) solution and polyimide precursor (PIP) [poly(amic acid), M_w=157,000 g/mol, HD Microsystems] in n-methyl-2-pyrollidine (NMP) (Aldrich Chemical Co.) solution (10.5 wt.% of poly(amic acid) in NMP). The magnetic probe particles were initially dispersed in distilled water, but they were re-dispersed in NMP, which is miscible with distilled water, for dispersion in the PIP solution. The magnetic particles were dispersed in the solutions in dilute quantity (~10^{-4} vol.%) and this small concentration (10^{-4} ~ 10^{-5} vol.%) of probe particles was used to avoid interactions between the particles in microrheology experiments [61, 66, 83]. The probe particle concentration has to be controlled carefully for efficient viscosity measurement; interactions or collisions between particles were observed during particle tracking experiment at higher probe particle concentration (~0.1 vol.%), however, the number of probe particles was too small to get reliable data points at very dilute particle concentration (< 10^{-7} vol.%). The solutions were held in a small container and its dimension (W×L×H) was 7 mm × 7 mm × 5 mm and the volume of the sample solution was less than ~0.3 ml. The position of the focal plane during the observation was at the center of the pole surface of the magnet to track particle motions under more uniform magnetic field and field gradient. The particles tracked were far (> 1 mm) from the

container walls. For comparison, standard bulk viscosities of the solutions were characterized by a rheometer with a cone-plate fixture (Rheometric Scientific, ARES).

The apparatus was then used to characterize the viscosity of coatings at room temperature, in the absence of drying. Coating samples were prepared from aqueous polyvinyl alcohol (PVA) solution (5.08 wt.% PVA, M_w=130,000 g/mol, Aldrich Chemical Co.) and 10.5 wt.% of PIP in NMP. Wire-wound coating and dip coating methods were used to apply the coating solution onto the glass substrate (10 mm × 25.4 mm), giving an expected wet coating thickness about 150 μm. Data was taken within 5 minutes in the case of PVA coatings in order to ensure that the polymer concentration did not change appreciably due to evaporation of water. Again the focal plane was chosen at the center of the poles for maximum uniformity of the magnetic field gradient. For most experiments, particles in the center of the coating were tracked to avoid interference from the substrate and free surface. However, in some experiments we monitored the magnetic particle motion at different depths through the coating thickness.

The effect of drying time and temperature on the viscosity of PVA coatings was determined. The experimental set-up was the same as that described above, but the data were taken as a function of time at various temperatures from room temperature to 80° C. The heating system and temperature controller connected to the sample stage of the apparatus were used. For each experiment more than 4 particles were monitored continuously. For any given time point, at least 10 images were captured (1 image/sec.) and used to calculate the average velocity at that time. For higher temperature, data was collected in shorter time since the time scale of the measurement must be shorter than

time scale of viscosity change. For these particle velocity measurements, the particles near the middle of the coatings were traced to avoid the effect of coating substrate or surface.

3.4.2 Comparison with bulk rheometry

The magnetic force on the probe particles was measured by mapping magnetic field distribution from the permanent magnets. Observed particles within solutions were 2 ~ 3 mm away from the magnet pole, and the measured magnetic field gradient was 65 T/m. The magnetization of MS0302 particles was 115 kA/m in the observation range; therefore, magnetic force on the particles was constant (F_m ~3.93 pN) for the validation experiments. The magnetic force is strong enough to apply the force balance equation between F_m and F_{drag} to calculate the viscosity using Equation (3.6).

Figure 3.7 shows the particle terminal velocities (v_p) measured in aqueous glycerol solution and PIP solutions as a function of time. During the particle observation experiments, the sedimentation of the probe particles was negligible; the sedimentation velocity (v_{sed}) in both solutions was too low (< 0.005 μm/s) to detect. No aggregation or interaction between particles was observed in the field of view (235 μm × 176 μm) during the measurement. The magnetic force on the particles in the field of view was constant and the particles reached a constant, terminal velocity quickly. The standard deviation in the velocity values is low, less than ~5% of the average. The viscosity of the solution can be calculated using the average terminal velocity of the particles according

to Equation (3.6) so long as the liquid is Newtonian. Aqueous glycerol is Newtonian [59], but the PIP solution exhibits non-Newtonian behavior above a critical shear rate for the shear thinning [89]. The shear rate for the microrheology experiment is approximately given by the ratio of the velocity to the particle diameter and hence for the PIP solution, the shear rate was about 0.1 s^{-1}. As demonstrated below, the PIP solution is Newtonian at this shear rate. The average terminal velocity of the particle in aqueous glycerol (96.7 wt.%) solution was 1.98 μm/s with a standard deviation of 4.33 %, and that of the particle in 10.5 wt.% PIP solution was 0.13 μm/s with a standard deviation of 5.07 %. The viscosities from the force balance equation are 0.21 and 3.21 Pa·s, respectively.

Standard bulk rheometry showed that the viscosity of aqueous glycerol (96.7 wt.%) solution was 0.20 Pa·s, and that of the PIP solution was 3.13 Pa·s. These values agree with microrheology results to within 5 %. In the magnetic microrheology experiment, particle size distribution, surface roughness or shape irregularity may influence on the particle velocity within a fluid. Since microrheology results match bulk rheology results well, the impact of these additional factors appears not to be significant. The consistency is expected in this case given that the probe particle size is bigger than the characteristic structural size of the constituents in the liquid [85, 90]. These results demonstrate that the apparatus generates constant magnetic force on the probe particles in the solution, and the viscosity of each solution could be determined using constant particle velocity during the observation.

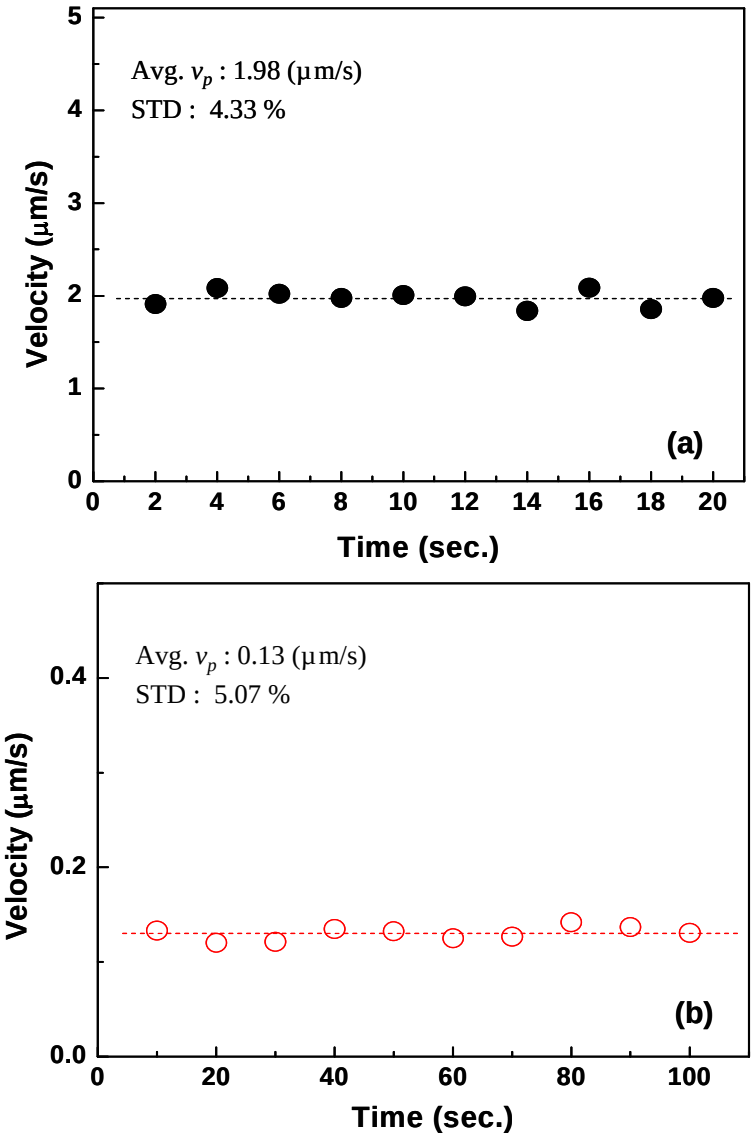

Figure 3.7 Velocity of probe particles in (a) aqueous glycerol (96.7 wt. %) solution and (b) 10.5 wt. % PIP solution.

Figure 3.8 (a) is the schematic of the particle velocity measurement and Figure 3.8 (b) shows an example of converted images of MS0302 particle (~1μm-diameter) trajectory in a PVA coating under the magnetic field gradient of 51 T/m. Particles in the middle of the PVA coating were traced to avoid the effects of the coating substrate and surface. The particle moved 21.96 μm for 9 seconds along the magnetic force direction, and its average velocity was 2.44 μm/s. Therefore, viscosity calculated from the force balance equation is 0.13 Pa·s; the shear rate was about 2.4 s^{-1} during the microrheology experiment. Since the particle velocities did not change significantly during the motion, the shear rate was almost constant.

The particle motions in PIP and PVA coatings were tracked under a range of magnetic field gradients of 40 ~ 67 T/m and the results compared with standard bulk rheometry of coating solutions. As shown in Figure 3.9, the viscosities of aqueous PVA solution and PIP solutions measured by standard bulk rheology were nearly constant in the low shear rate range. At $\dot{\gamma} = 0.1\ s^{-1}$, the viscosity of the PVA and the PIP solutions is 0.11 Pa·s and 3.13 Pa·s , respectively. Microrheology experiment results for PVA and PIP coatings without drying are also shown in Figure 3.9. The shear rate in these experiments was adjusted by changing the magnetic field gradient and hence the velocity of the particle. The average viscosity of the PVA coating by microrheometry is 0.13 Pa·s, while that of the PIP coating is 3.47 Pa·s. These values are close, but slightly higher, than to those determined from bulk rheometery.

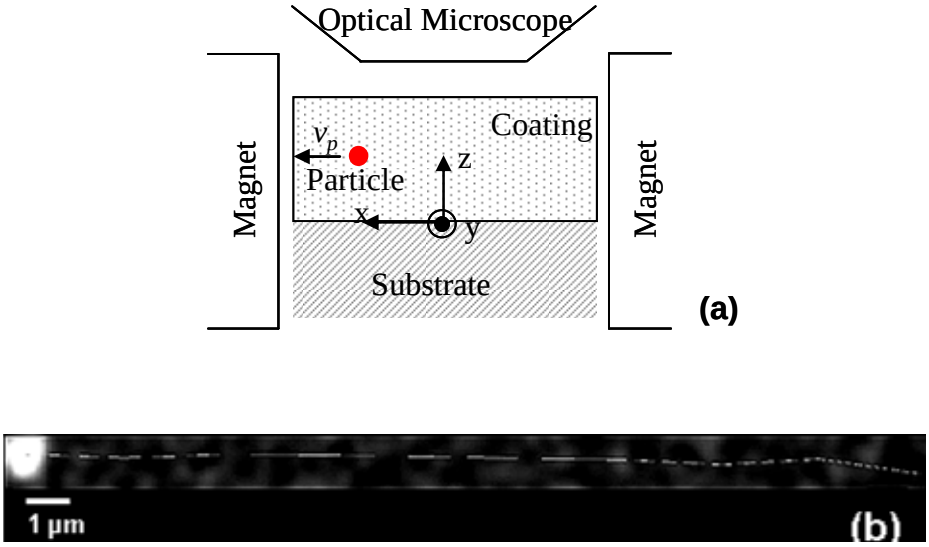

Figure 3.8 Schematic representation of (a) the particle velocity measurement and (b) acquired particle trajectory of MS0302 magnetic particle in PVA coating without drying process.

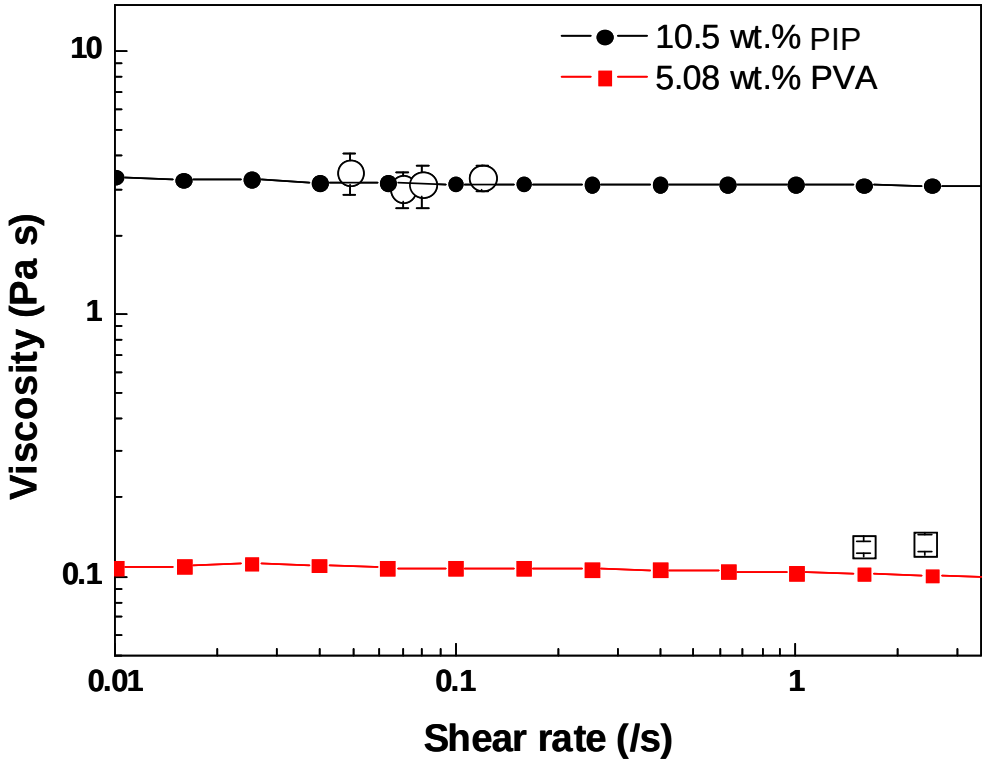

Figure 3.9 Viscosity versus shear rate of PIP and PVA wet coatings from particle velocity measurement (open), and the results of coating solution from standard bulk rheometry (solid).

3.4.3 Wall effect correction

Particle motion within coated liquid layers may be affected by the substrate. It has been studied that the drag on a spherical body moving in a containing vessel is significantly influenced by the existence of the wall, called the '*wall effect*' [91]. The wall effect on a moving particle in fluids is not negligible, and it is more significant in non-Newtonian fluid [92]. The wall effect correction factor becomes larger when the radius of the particle is close to that of the tube. Therefore, a particle that is closer to the wall will experience a higher drag force due to the wall effect.

Proximity to the substrate influences the velocity of a probe particle and must be accounted for in studies that probe spatial variation in viscosity through the coating thickness. A theoretical prediction [93] of this effect is given by

$$\eta = \left(1 - \frac{9R}{16z}\right)\left(\frac{2MR^2\,(dB/dx)}{9\mu_0 v}\right) \tag{3.7}$$

where z is the distance between the particle center and the substrate, and is plotted in Figure 3.10. Equation (3.7) holds for practical distances but not for those very near to the substrate ($z \rightarrow R$). The prediction reveals that a particle closer to the substrate experiences a higher drag force, and therefore has a slower velocity. For a probe particle of radius R, the particle velocity reaches 99 % of its uncorrected value at a distance of $56.25R$ from the substrate. This theoretical prediction is quite close to the criterion that previous researchers used (~20 diameters distance from a solid surface) to avoid the effect [61, 66, 83].

Particle velocity measurements at various positions through the thickness of a PIP coating were carried out using the Hirox lens (magnification: 1,400×, DOF: 7.6 μm). A magnet placed beneath the substrate was used to adjust particle position relative to the substrate. By focusing at the surface of substrate, a reference point was set and the distance that the stepper motor moves the lens to get a particle in focus provides its z position. Figure 3.10 shows the measured particle velocity data within the PIP coating along with the prediction from Equation (3.7). The measured particle velocity decreases when the particle moves near the substrate, consistent with the theory, and shows the condition necessary to avoid the 'wall effect' ($z > 56.25R$). The data also shows that the probe particle velocity is independent of position if the measured particles are sufficiently far away (> 30 μm) from the coating substrate and free surface. However, the measured velocity is slower compared to the prediction as the particle approaches the substrate. This difference is due in part to DOF of the lens (7.6 μm), which is shown as the horizontal error bar. Uncertainties in particle size and shape may also contribute to the difference and more work with a smaller DOF lens is needed for accurate measurements near the substrate.

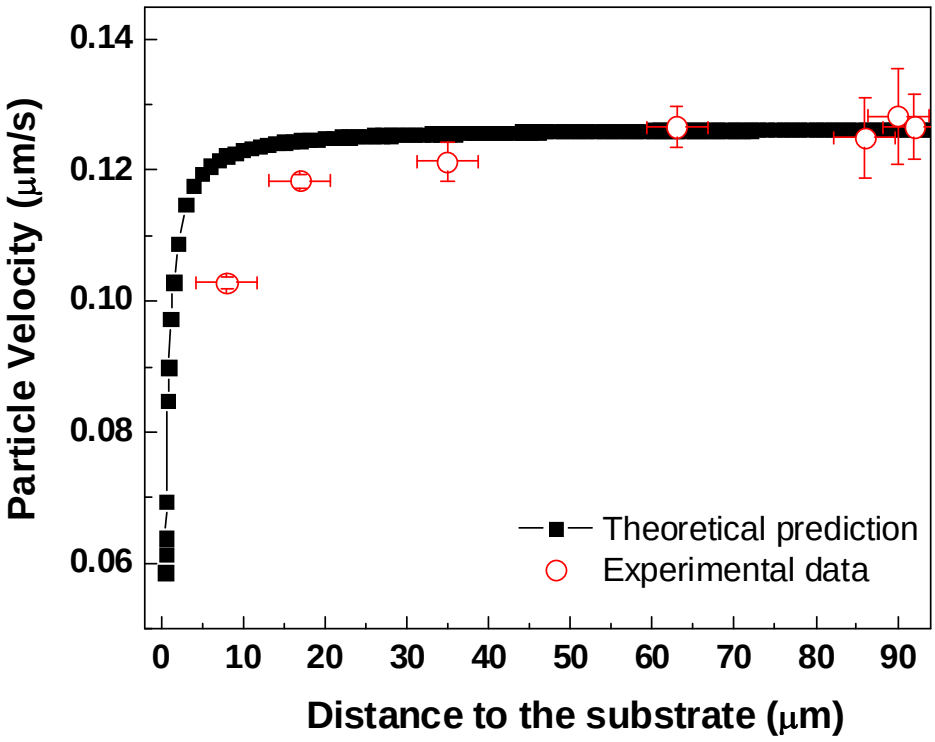

Figure 3.10 Theoretical prediction and experimental data of the effect of coating substrate on particle velocity within wet PIP coating as a function of position through coating thickness. Theoretical prediction and experimental measurements were done with 0.5 μm-radius particle in PI coating (=3.2 Pa s) under the applied magnetic field gradient of 65 T/m.

3.4.4 Coating viscosity measurement during drying process

The time evolution of the viscosity of a 5.08 wt.% PVA coating at various temperatures was measured using the microrheology technique. Figure 3.11 shows the particle velocity and calculated viscosity as a function of drying time at room temperature. As water evaporates, the particle velocity decreases and the viscosity of the coating increases from 0.13 Pa·s, initially, to 7.88 Pa·s after 44 minutes drying. There is a steep increase in viscosity at the later stages of drying. With the magnetic field gradient used in this experiment (up to 67 T/m), the particle motion became too slow to track after 44 min. The range of coating viscosities that can be measured with the apparatus is limited by the magnetic properties and the size of the probe particles and the magnitude of the generated magnetic field gradient. Bigger probe particles (2 ~ 10 μm diameter) would be suitable to characterize higher viscosity coatings since particle velocity in a given viscous medium is proportional to the square of the particle size. With bigger probe particles, however, tracking the *z* position and correcting for the effect of the substrate are more likely to be necessary.

Figure 3.12 show the viscosity of the coatings dried at higher drying temperatures (60 and 80 $^{\circ}$C). Measured coating viscosities did not change much in the early drying stage. We did not detect a viscosity decrease, which is expected due to the temperature increase. The polymer concentration increases quickly at higher drying temperatures, and therefore, these two competing effects may occur at very short time scales or simultaneously. The measurement time scale was limited by the frame rate (1 fps), and the actual measurement time for one probe particle at a given drying time was 10 ~ 20 s

since multiple data points were collected to calculate the viscosities. In the apparatus, taking a movie with higher frame rate (15 fps) would be beneficial to characterize rheological properties at shorter time scale during the coating solidification process.

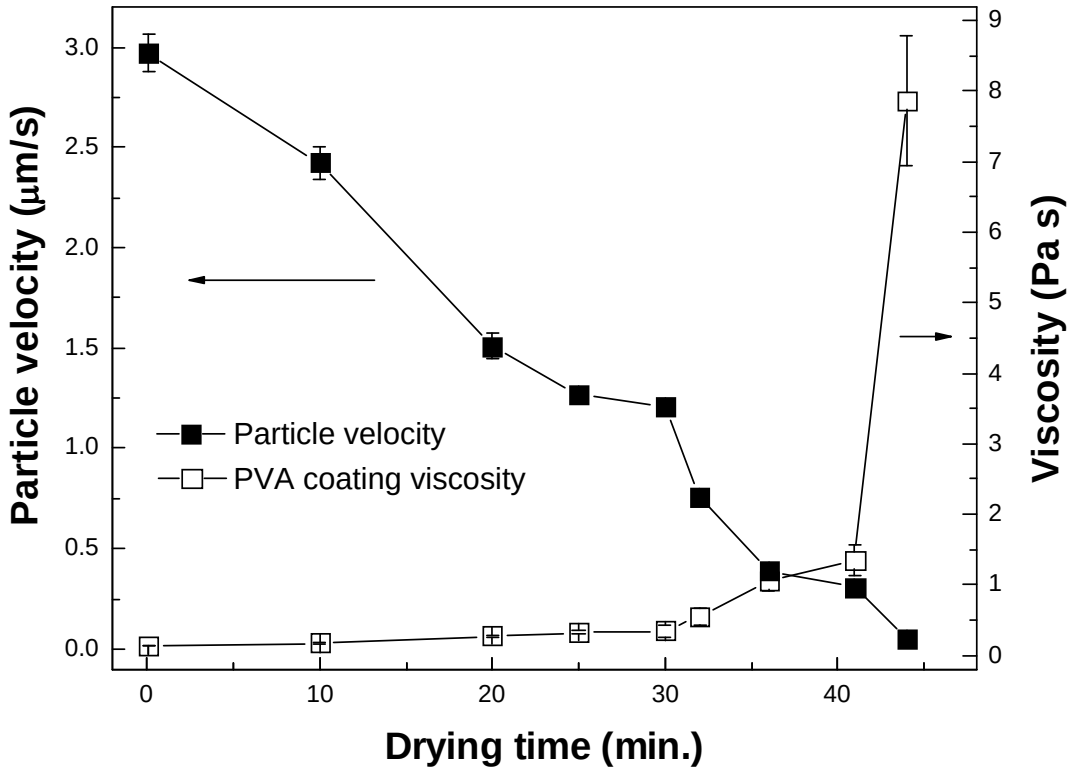

Figure 3.11 Particle velocity changes (solid square) in PVA coating and calculated viscosity (open square) of PVA coating as a function of drying time.

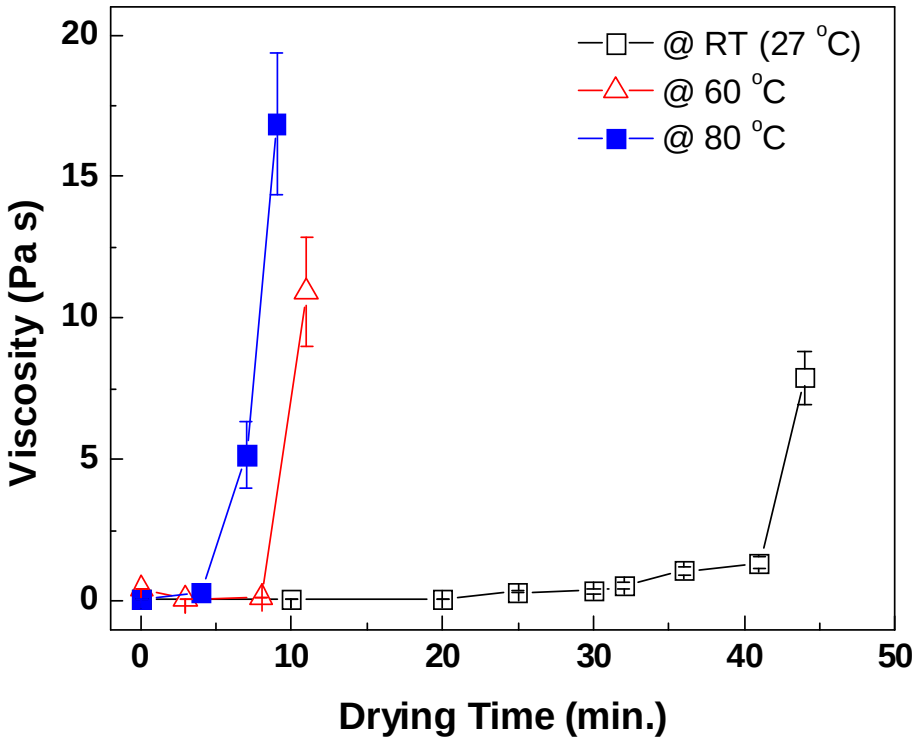

Figure 3.12 PVA coating viscosity change from particle velocity measurement at different drying temperatures; 27 °C (open circle), 60 °C (open triangle) and 80 °C (solid circle)

3.5 Summary

A magnetic microrheometer has been designed for the measurement of coating viscosity. The apparatus makes use of a long working distance, digital optical microscope so that magnet placement near the coating is possible. The method can follow the viscosity change of coated layer during drying or curing process at different temperatures. Hence, it can be used to gain a better understanding of defects related to rheology, such as sagging and insufficient leveling, and especially for tuning formulations and process conditions to avoid those defects. Probe particle velocity can also be tracked as function of thickness through a coating, and therefore, the method has the potential for characterization of a "skin" on the coating surface.

Chapter 4. Depthwise Viscosity Gradient in UV cured Epoxy Coatings*

4.1 Introduction

UV cured materials have been used in a wide range of coating applications, such as automotive and architectural coatings, wood and metal finishings, dental coatings, and encapsulants for electronic devices [22, 23]. The UV curing process provides high efficiency and reduces volatile organic compounds in manufacturing. Its advantages of fast cure, low operating costs and environmental friendliness have driven the current growth [23, 24]. UV curable systems generally consist of a photoinitiator (PI) and a mixture of reactive monomers and oligomers. UV light absorbed by the PI induces photopolymerization to form the final coating product. The curing reaction kinetics and structure development rate are affected by the type and concentration of PI, the wavelength and irradiance of UV light, and curing temperature [22-24]. Photorheology techniques that can characterize the local viscosity of coatings during photopolymerization will be useful for the investigation of the effects of these parameters on the structure development, final properties, and related defects.

Several methods have been developed to study the rheological properties of various UV curing systems. Modified parallel plate and oscillating rheometer designs have been used to monitor dynamic moduli (G', G'') during the UV curing process [25,

* A portion of this chapter has been published as: Jin-Oh Song, Alon V. McCormick, and Lorraine F. Francis, Depthwise viscosity gradients in UV-cured epoxy coatings, Macromolecular Materials and Engineering, 2012, DOI: 10.1002/mame.201100362.

26]. These methods have been improved for a wide range of measurable rheological property with a shorter time scale [94-96], and the methods have been combined with real-time Fourier-transform infrared (FTIR) spectroscopy to relate the extent of conversion to rheological data [27]. However, the samples for these previous studies are placed between the plates, and are not coatings. Moreover, these methods provide depth-averaged data and are not able to characterize depthwise gradients in local rheological properties.

UV light attenuation can produce depthwise gradients in the degree of cure [97]. UV irradiance is attenuated through coatings, for example, due to the absorption by PI. The Beer-Lambert law [97] in Equation (4.1) describes the effect of thickness and coating composition on light absorbance:

$$I_a = I_o(1-10^{-\varepsilon c l}) \tag{4.1}$$

where I_a and I_o are absorbed and incident irradiance of light, respectively, ε is molar absorption coefficient of the absorber (i.e., PI), c is the absorber concentration, and l is the material thickness. In addition, oxygen inhibition of the curing reaction at the surface can cause depthwise gradients in the structure development [98]. Such nonuniformity can cause gradients in the rheological properties of the coatings as they cure.

With PI absorption, the variation in the irradiance through the thickness leads to the development of a conversion gradient. The surface of the coating receives a higher irradiance of light and hence experiences a higher conversion. In the extreme, a solidified

'skin' can form at the coating surface. The skin can develop compressive stress due to the swelling from the diffusion of unreacted monomer beneath. When the compressive stress is high enough to make the skin buckle, wrinkles appear on the coating surface [3, 11].

In situ characterization of the change in coating viscosity as a function of depth during photopolymerization would be useful for designing process conditions and coating formulations. Some progress in measuring depthwise gradients has been made. Raman spectroscopy [28] and nano-indentation [99], have been used to follow conversion and modulus, respectively, but not during photopolymerization. Particle tracking microrheology [30] methods were used to characterize the gelation time of UV curing coatings as a function of depth during photopolymerization; however, this method did not provide real-time photorheology information.

In this chapter, a magnetic microrheometer is used for *in situ* characterization of the viscosity of epoxy coatings as a function of depth during the UV curing process. Epoxides are widely used as monomers for cationic photopolymerization, and the resulting epoxy coatings show good mechanical properties and adhesion to various substrates [100]. This system was chosen because it does not suffer from oxygen inhibition effects [98]. The local viscosity is measured by tracking the changes in magnetic probe particle velocity during UV light exposure at different depths through the coating thickness. Final coating surfaces are observed to detect surface defect formation, and real-time FTIR is also used to follow the bulk extent of cure, averaged over coating thickness. The measured microrheology results are used to study the effect of various

process conditions on the development of viscosity gradients and the formation of surface defects.

4.2 Experimental Section

4.2.1 Materials and methods

The epoxy resin for the coatings was bis-(3,4-epoxycyclohexylmethyl) adipate (Syna-Epoxy 28, Synasia Inc., NJ). A mixed triarylsulfonium hexafluoroantimonate salt (UVI-6976, Cyracure, NY) was added into the epoxy resin as photoinitiator for the cationic photopolymerization. The chemical structures of the epoxy resin and the PI are shown in Figure 4.1. UV absorption spectra of the coating materials were obtained using UV-visible spectrometer (8453, Hewlett Packard, Waldbronn, DE). Superparamagnetic Fe_3O_4 particles (MS0302, 1 μm in diameter, MagSense Life Sci.) were dispersed in the coating at low concentration (~10^{-4} vol.%). Coatings were prepared on a glass substrate using Mayer rods. The wet coating thickness was ~80 μm for the microrheology experiments. The initial viscosity of the wet coating without PI and UV curing was 0.49 Pa·s at room temperature, as measured by the magnetic microrheometer.

The coating samples were cured and monitored using a range of process conditions. A 365 nm wavelength UV lamp with an irradiance of 20 $\mu W \cdot cm^{-2}$ was used to cure the coatings with 0.2 and 2 wt.% of PI concentration to investigate the effect of PI concentration on the viscosity gradients and wrinkle formation during the curing process. To study the dependence on curing temperature, UV light wavelength, and irradiance, samples were also cured at 60 ^{o}C, with a shorter wavelength (254 nm) UV lamp, and at

two additional irradiances (1,000 and 20 $\mu W \cdot cm^{-2}$, by adjusting the lamp-to-coating distance to 30 and 85 mm).

Coating surfaces and the bulk extent of polymerization of the epoxide monomers were also monitored. Coating surface changes were observed by capturing pictures continuously at specified intervals (30 ~ 60 sec.) during curing using the digital optical microscope. Since the epoxide rings open during the polymerization, the disappearance of the characteristic peak (844 cm^{-1}) absorbance for epoxide ring stretches was monitored to track the bulk extent of cure by FTIR (Magna IR-750, Nicolet Instrument Co., WI). Real-time FTIR spectra were obtained during UV light exposure inside the FTIR instrument with the UV lamp positioned so as to avoid blocking the IR beam path. Coating liquids were sandwiched between two NaCl plates separated by a Teflon spacer to control the sample thickness of ~80 µm. Each conversion data point came from averaging 32 scans (total collection time: 19 sec.).

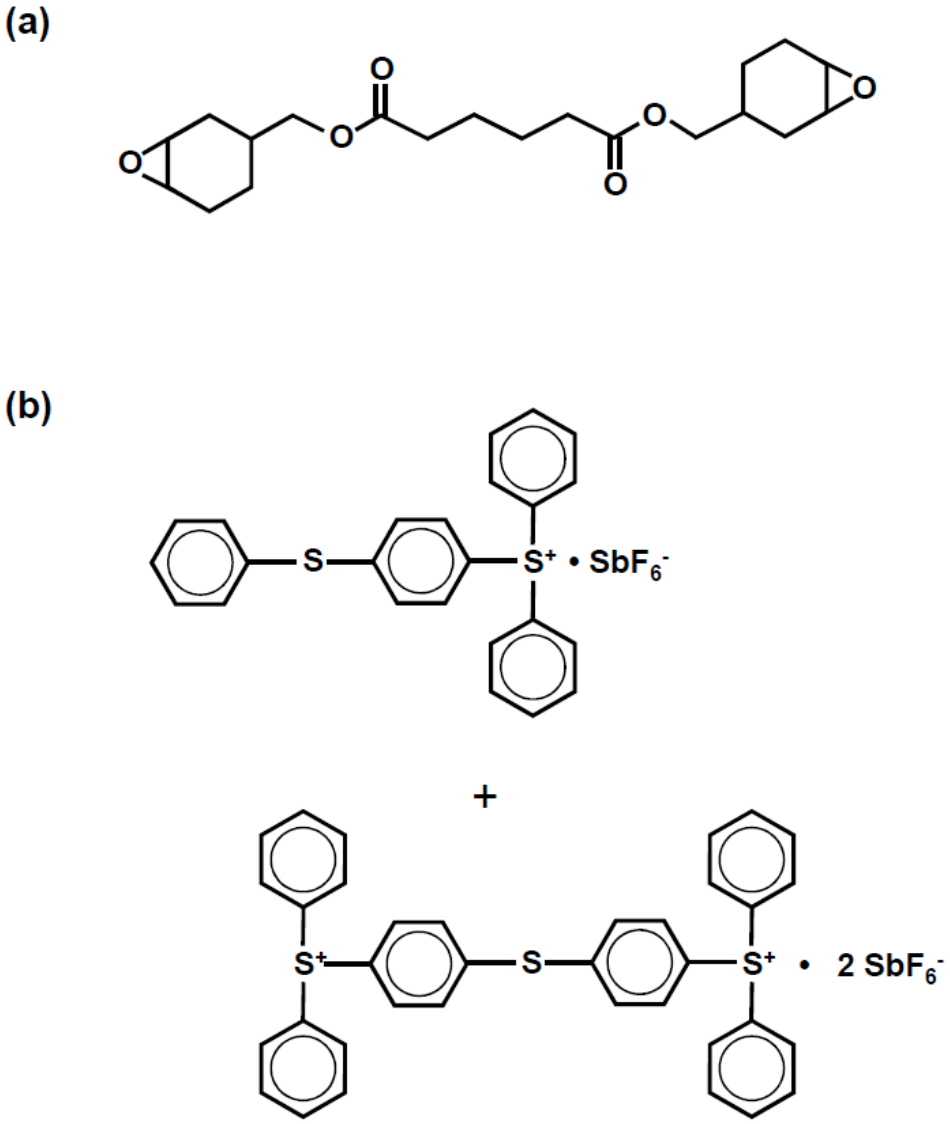

Figure 4.1 Chemical structures of (a) bis-(3,4-epoxycyclohexylmethyl) adipate and (b) a mixed triarylsulfonium hexafluoroantimonate salts.

4.2.2 Particle tracking for viscosity gradient measurement

The magnetic microrheometer is used for particle tracking in different depths in the coatings. A double NdFeB magnet configuration is used to control the magnitude and uniformity of the generated magnetic field gradients between the magnets. A digital optical microscope system and particle tracking software are used for the particle tracking. The digital optical microscope system has a long working distance (13 mm), and the magnification and depth-of-field (DOF) can be adjusted by changing the objective lens. The heating system with a temperature controller is connected to the sample stage, and the UV lamp with nominal wavelength of 254 or 365 nm (Spectroline, NY) is positioned between the objective lens of the microscope (1,400×) and coating for curing process. The wavelength range of the light emitted from the 254 nm lamp shows a narrow distribution (250 ~ 260 nm) compared to that from the 365 nm lamp (310 ~ 410 nm) [101]. The UV irradiance can be changed by adjusting the lamp-to-coating distance; it was measured using digital radiometer (DRC-100X, Spectroline, NY) with sensors (DIX-254A and DIX-365A, Specroline, NY) that have a spectral range of 230 ~ 280 nm (DIX-254A) and 320 ~ 400 nm (DIX-365A), respectively [102].

The viscosity variation through the coating thickness was characterized during UV light exposure using the magnetic microrheometer, as shown in Figure 4.2 (a). Given the DOF (7.6 μm) of the objective lens, most magnetic microrheology experiments were carried out in ~80 μm thick coatings to allow depthwise gradients to be detected. Since the coatings are optically transparent, the magnetic probe particles can be tracked at different depths simply by adjusting the lens position. Three different *z* positions from the

substrate were imaged in the coatings: top (z_1: ~70 µm), middle (z_2: ~55 µm) and bottom (z_3: ~35 µm). The magnetic particle motion along the applied magnetic field gradient direction was monitored as a function of UV exposure time. The bottom position (z_3) was set to be far enough from the substrate to avoid the reduction in particle velocity from the wall effect [103].

An example of the accumulated particle displacement as a function of time along the magnetic field gradient direction is plotted in Figure 4.2 (b). The slope of each time section is determined to provide particle velocity information. Sedimentation may cause the particle to leave the focal plane, but this event was rare and did not interfere with microrheology experiments; under our conditions, there was adequate lateral motion along the magnetic force direction for the particle velocity measurement. Enough data (at least 10 images) are taken to determine velocity for a given time segment. The interval between the images taken depends on the particle velocity. For example, the minimum interval time was 1 second when the coating viscosity was low (faster particle velocity), and it became up to ~30 seconds as the viscosity increased during curing. A different, identically prepared and cured sample was used to gather data at each *z* position for depth profiles of epoxy coating viscosity. At least five different samples were used to build one set of viscosity-time profile at each *z* position. The schematic representation of particle trajectories at different z positions in the wet epoxy coating is shown in Figure 4.3.

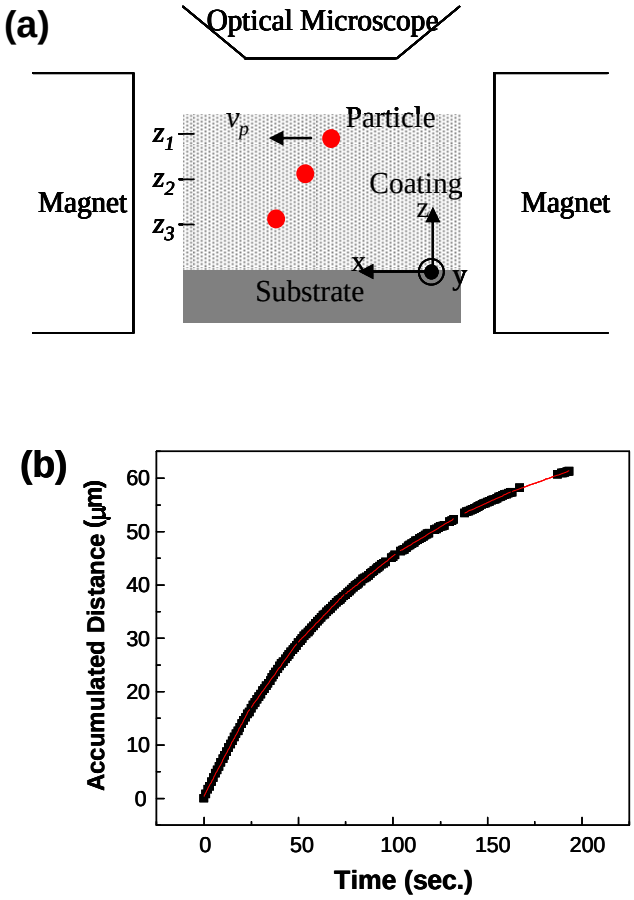

Figure 4.2 Schematics of (a) particle velocity measurements in UV curing coatings at different z positions (z_1: 70, z_2: 55 and z_3: 35 μm from the substrate), and (b) an example of the accumulated particle displacement along the applied magnetic field direction in UV curing coatings.

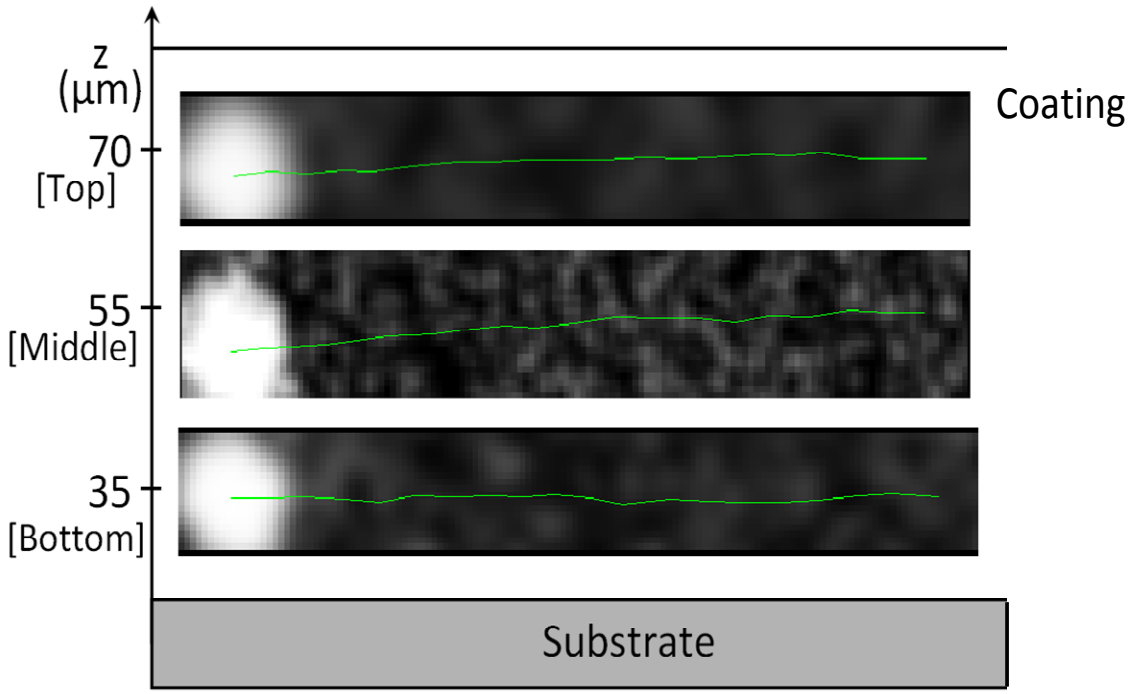

Figure 4.3 Schematic representation (not to scale) of the particle trajectories of magnetic probe particles at each *z* position in the wet epoxy coating.

4.3 Results and Discussion

4.3.1 Effect of photoinitiator concentration

The effect of the PI concentration was investigated using ~80 µm coatings cured at room temperature, with the 365 nm UV lamp at an irradiance of 20 $\mu W \cdot cm^{-2}$. Figure 4.4 shows the increase in conversion in epoxy coatings with an increase in PI concentration, as determined by real-time FTIR. In the coating with 0.2 wt.% PI, the degree of conversion increased rapidly and then leveled off at ~8 % after ~20 minutes of cure. With the higher amount of PI (2 wt.%) the conversion continued to rise with time, as expected due to the greater number of cationic active centers. With the conditions of our experiments, the conversion only reaches ~20 %. The degree of conversion can be increased by raising the irradiance or the temperature for a fixed time of UV light exposure [100]. However, since the goal of the present study is to characterize gradients, the relatively slow rate of cure was beneficial. The FTIR results in Figure 4.4 show depth-averaged data and do not provide spatial gradient information.

The viscosity-time profile through the coating depth was determined from magnetic microrheology studies for epoxy coatings with 0.2 and 2 wt.% PI. See Figure 4.5. The coating samples were cured on the sample stage of the magnetic microrheometer for particle tracking experiments using the same condition as for the FTIR measurements. For the coating prepared with lower PI content, the viscosity increases during curing at the top (z_1) and middle (z_2) were similar; however, the viscosity at the bottom (z_3) was

low compared to those of the upper positions. In contrast, for the coating prepared with higher PI content, the viscosity of the epoxy coating increased more rapidly with a steep increase of viscosity at the top position after 5 minutes of curing. The viscosity difference between the top and the lower positions became more significant during curing. For example, at ~10 minutes of cure the viscosity at the top position was out of our measurement range (< 600 Pa·s to use the assumption of Equation 3.6). However, the viscosity at the middle and bottom positions was still low (< 100 Pa·s).

The magnetic microrheometry data demonstrate the effect of PI concentration on both the rate of viscosity rise and the gradient development through the coating thickness. A power-law model could be fit to the viscosity-time curve at each depth in Figure 4.5:

$$\log \eta(t) = \log \eta_0 + nt \tag{4.2}$$

where $\eta(t)$ is the viscosity of the material as a function of time, η_0 is initial viscosity before curing reaction, n is a rate coefficient that indicates the rapidity of viscosity increase, and t is the time. This model has been used to analyze dynamic chemorheology of curing materials [104]. The n and R-squared values were calculated by fitting the viscosity-time curves; results are summarized in Table 4.1. The rate coefficient at any particular position is higher in the coatings with higher amount of PI, indicating faster curing. Within the coating with 2 wt.% PI, the viscosity rise in the top position was almost twice as fast as the middle position. The difference between the top and middle positions in 0.2 wt.% PI coating was smaller than the difference in the 2 wt.% PI coating.

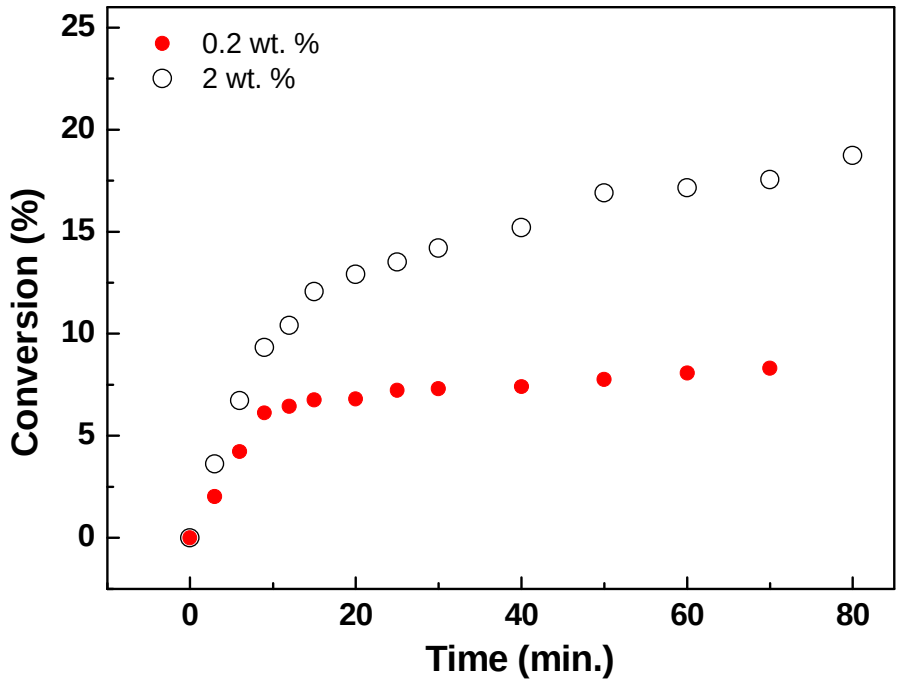

Figure 4.4 Real-time degree of conversion measurements using FTIR as a function of curing time of epoxy coatings with 0.2 and 2 wt.% PI concentration. Sample thickness for the conversion measurement is 80 µm. Data was collected with a UV wavelength of 365 nm at 20 $\mu W \cdot cm^{-2}$.

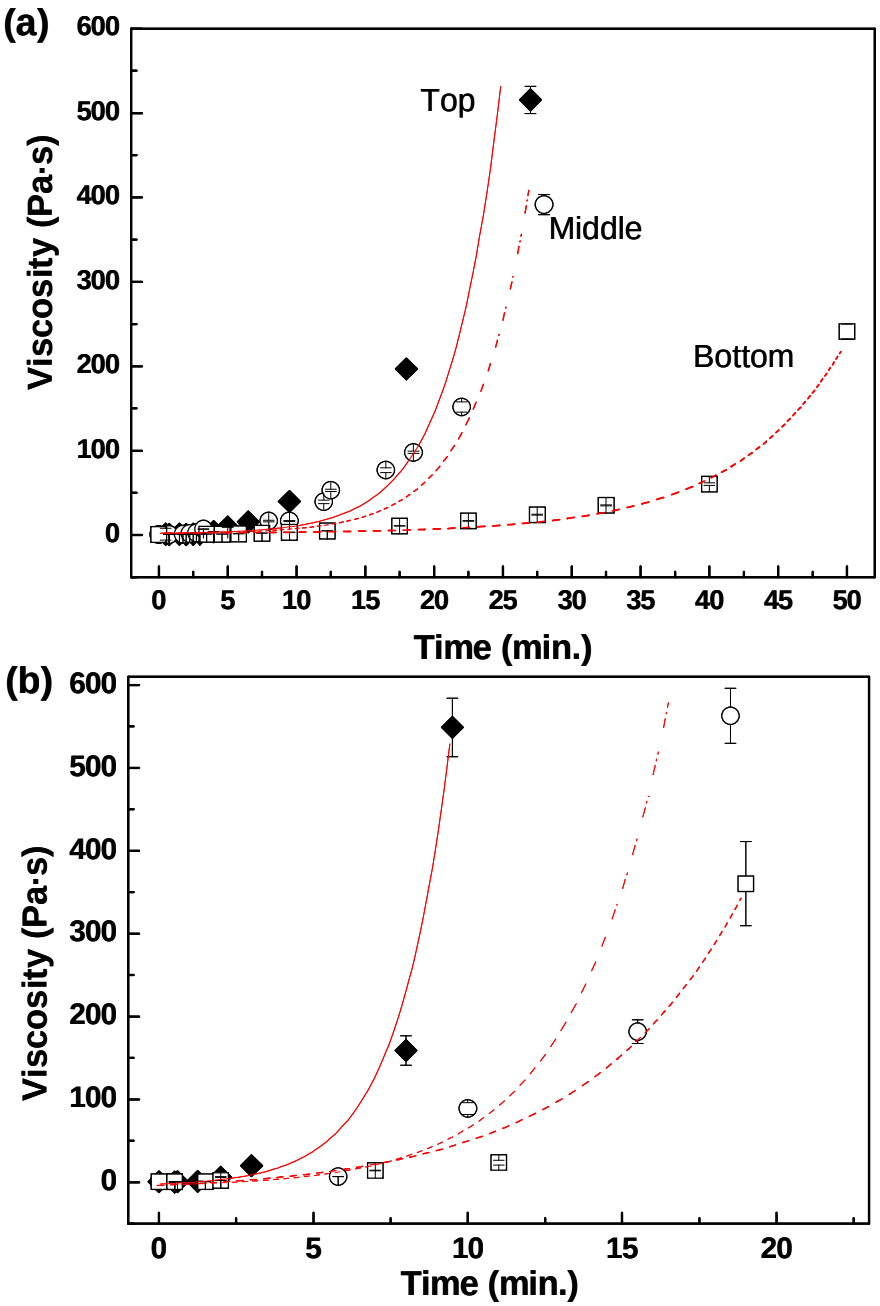

Figure 4.5 Viscosity-time profile of ~80 µm epoxy coatings at different *z* positions during curing with 365 nm UV lamp with an irradiance of 20 µW·cm^{-2} with the PI concentration of (a) 0.2 wt.% and (b) 2 wt.%. Equation (4) was used to fit the data. Error bars are based on the standard deviation of multiple measurements of particle velocity in a given time period, and the sample to sample variations. Equation (4.2) was used to fit the viscosity-time curves.

Table 4.1 Rate coefficient (*n*) at each depth in coatings* with different PI concentrations.

z position	*n* (R-squared)	
	PI 0.2 wt.%	PI 2 wt.%
z_1	0.11 (0.923)	0.31 (0.898)
z_2	0.10 (0.916)	0.17 (0.806)
z_3	0.05 (0.963)	0.15 (0.853)

* Cured with 365 nm UV lamp at 20 μWcm^{-2}

These curing gradients can also affect the final coating surface properties, such as wrinkles on the coating surfaces; therefore, the coating surfaces were monitored during UV light exposure to investigate surface appearance of UV cured epoxy coatings and its dependence on the process conditions. Figure 4.6 shows the effect of PI concentration on the surface appearance. An 80 µm thick coating with 0.2 wt.% PI concentration did not show any wrinkling (Figure 4.6 a), but a similarly thick coating with 2 wt.% PI showed wrinkling defects (Figure 4.6 b). The formation of wrinkles is consistent with the mechanism proposed by Basu *et al.* [11]. The diffusion of epoxy monomer into the pre-cured surface layer or skin causes swelling, which is constrained by the substrate, and leads to compressive stress. To relieve this stress the skin buckles out-of-plane, causing the wrinkling defects.

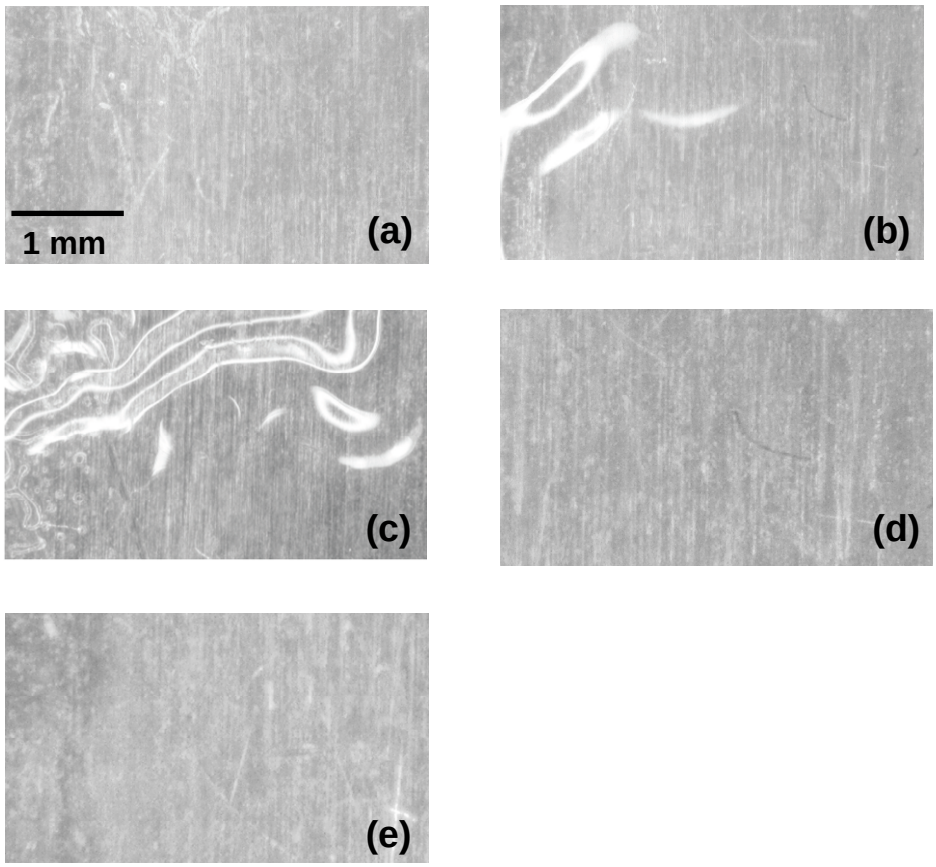

Figure 4.6 Epoxy coating surfaces after 90 minutes of curing cured with 365 nm and 20 $\mu W \cdot cm^{-2}$ UV light with coating thicknesses and PI concentrations of (a) 80 µm and 0.2 wt.%, (b) 80 µm and 2 wt.%, (c) 100 µm and 0.2 wt.%, (d) 20µm and 0.2 wt.%, and (e) 20 µm and 2 wt.%.

The magnetic microrheology results provide quantitative experimental data that can be used to investigate the relation between skin formation, surface wrinkles and the gradient development. A faster increase in the viscosity at the top of the coating with 2 wt.% PI (Table 4.1) compared to the middle and bottom positions indicates that the top position cures more rapidly. Therefore, a thin skin layer forms on a less-cured, viscous sub-layer. The viscosity at the top position was above the measurable viscosity range of the magnetic microrheometer after ~10 minutes of curing, while the viscosities at the middle and bottom positions were still within measurable ranges until ~20 minutes. Wrinkles started to appear on this coating after ~20 minutes of curing during the real-time monitoring of coating surfaces. These results show that the gradient between these top and middle positions significantly influences the wrinkling behavior, and the wrinkling of the coating with higher PI concentration appears to be linked to the measured steeper viscosity gradient between top and middle positions.

In contrast, no wrinkles were found on the surface of the coating with 0.2 wt.% PI, although a viscosity gradient was measured in Figure 4.5 (a) and Table 4.1. The coating with less PI showed more uniform viscosity increase at both the top and middle positions, while the viscosity increase was much slower only at the bottom position. The smaller difference in the rate coefficient (n) between top and middle positions led to a smooth coating surface. A thicker cured upper layer tends to form; this layer did not wrinkle, likely because it is thick enough and more fluid-like to resist buckling. These results are consistent with previous theoretical analysis of the buckling of an elastic skin

over viscous sub-layer; the critical wavelength, the minimum wavelength required for wrinkling, is reduced as the thickness of skin layer decreases [11].

In addition, the wrinkling behavior also depends on coating thickness. Wrinkles were found on the thicker (~100 µm) coatings with 0.2 wt.% PI concentration, as shown in Figure 4.6 (c). However, Figure 4.6 (d) and (e) shows that no wrinkles were produced at either PI concentration when the thickness was reduced to ~20 µm. The spatial viscosity gradient development in the thinner coating could not be measured accurately due to the DOF limit of the optical microscope. However, we expect the gradient to be diminished due to Equation (4.1). In coatings that are thick or with higher amounts of PI, more severe wrinkling defects form. These coatings are more likely to develop a distinct depthwise viscosity gradient and to form a skin. These results correlate well with the previous trends in our study of UV cured acrylate coatings [3]. And the size of this wrinkle pattern can be affected by the thickness and modulus of the skin layer, which also depends on the curing condition and materials [11]. The influence of PI concentration and coating thickness on wrinkle defects is summarized in the defect regime map in Figure 4.7. Cured coating surfaces and wrinkle defects were inspected visually.

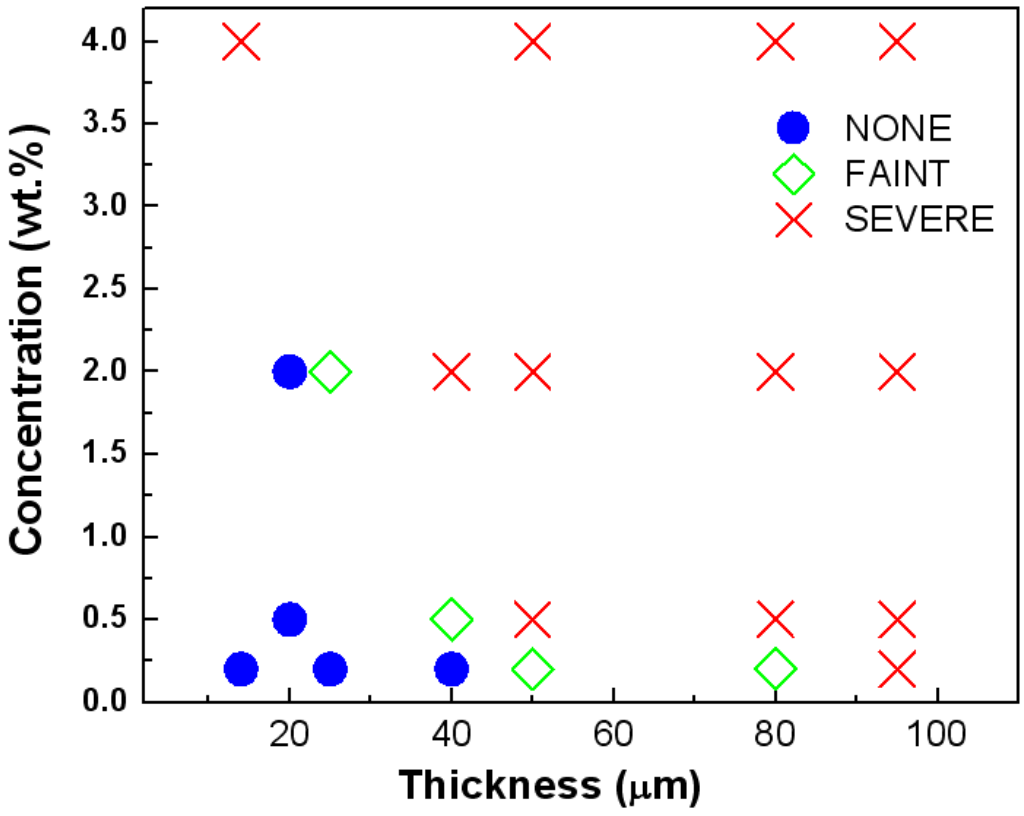

Figure 4.7 Defect regime map of epoxy coating cured with 365 nm and 20 μW·cm^{-2} UV light.

4.3.2 Effect of UV light source

The depthwise gradients of viscosity in the epoxy coatings were also affected by the wavelength and irradiance of UV light. A 254 nm wavelength UV lamp was used to cure the epoxy coatings with 0.2 wt.% PI at room temperature to investigate the effects. The coating cured with 254 nm wavelength UV light with an irradiance of 20 $\mu W \cdot cm^{-2}$ showed faster viscosity build-up at the top position of the coating and more severe gradients between the top and middle position in the coating compared with the results for a 365 nm UV lamp shown in Figure 4.8 and Table 4.2.

Figure 4.9 shows the UV absorption behavior of PI and a mixture of epoxy monomer with 0.2 wt.% PI, and the illustration of emission spectra of 254 and 365 nm UV lamps. Solutions of 0.6 wt.% of PI and monomer mixture, and 0.0012 wt.% of PI in methanol were prepared, respectively, to keep the same amount of PI in the methanol solution. The spectra of both solutions show strong absorption below 260 nm while the 254 nm UV lamp emits its radiation at the range of 250 ~ 260 nm. However, the absorption became almost negligible above 350 nm, indicating that less photo-induced polymerization could be achieved by the light emitted from the 365 nm UV lamp due to the absorption peak position as well as the broad spectrum with lower average spectral irradiance [101]. The steeper viscosity gradient measured in the coating cured with 254 nm wavelength (Figure 4.8 a) can be attributed to the stronger absorption by the PI at 254 nm, which produces faster cure and viscosity build-up at the top surface. According to the Beer-Lambert law in Equation (4.1), the decay rate of UV irradiance through the thickness is more severe; therefore, more significant curing gradients are expected.

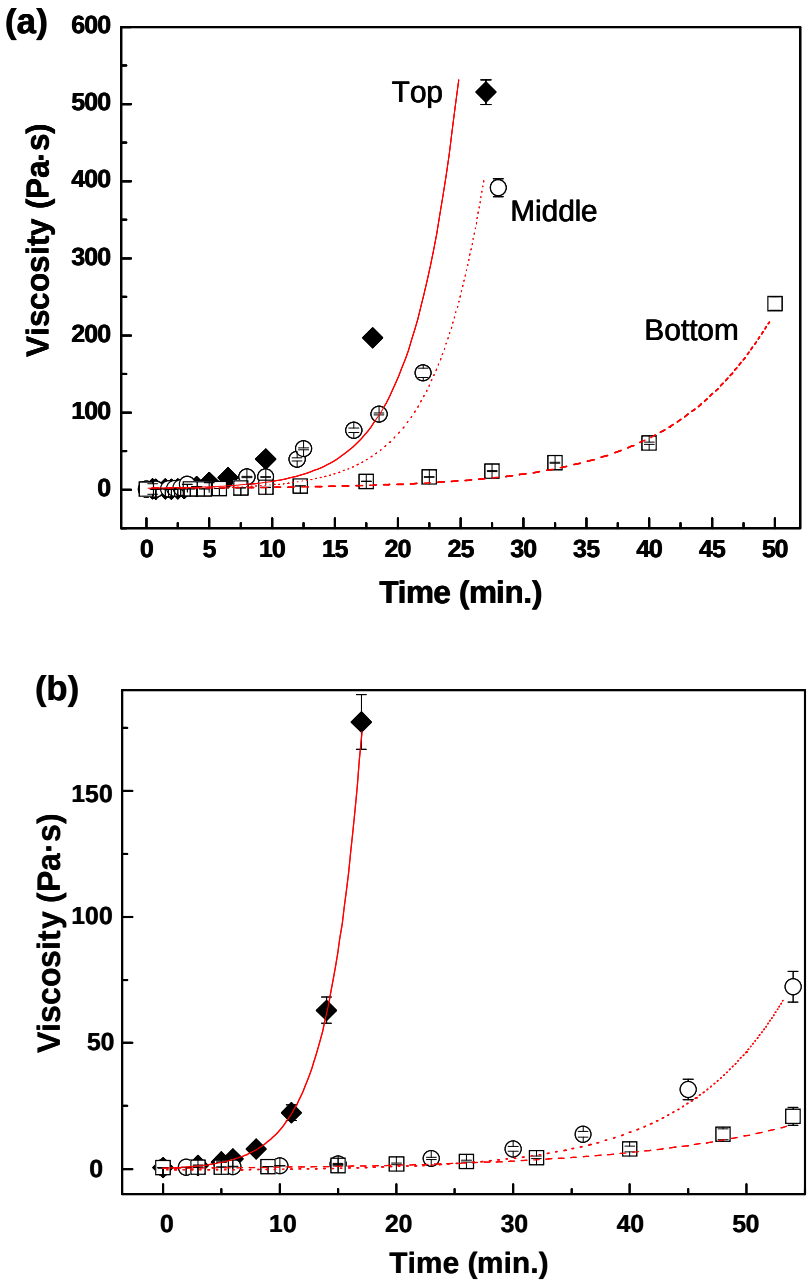

Figure 4.8 Effect of UV light wavelength on the viscosity-time profile of ~80 µm epoxy coatings with 0.2 wt.% PI concentration. Coating samples were cured with an irradiance of 20 µW·cm^{-2} at room temperature using (a) a 365 nm lamp and (b) 254 nm lamp. Equation (4.2) was used to fit the viscosity-time curves.

Table 4.2 Rate coefficient (*n*) at each depth in coatings* cured at different UV light wavelength.

z position	*n* (R-squared)	
	365 nm	254 nm
z_1	0.11 (0.923)	0.15 (0.929)
z_2	0.10 (0.916)	0.04 (0.917)
z_3	0.05 (0.963)	0.03 (0.912)

* Cured with 0.2 wt. % PI and an irradiance of 20 μWcm^{-2}

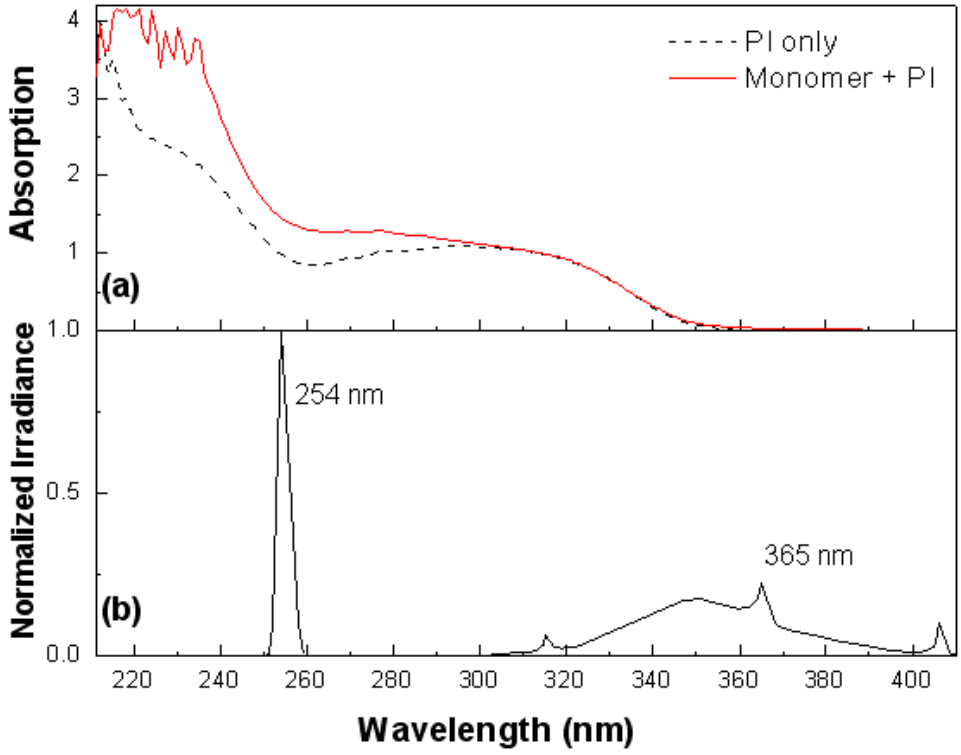

Figure 4.9 (a) UV absorption spectra of PI (UVI-6976) and the mixture of epoxy monomer with 0.2 wt.% PI, and (b) schematic of emission spectra of 254 and 365 nm UV lamps, illustrated using the product information [101].

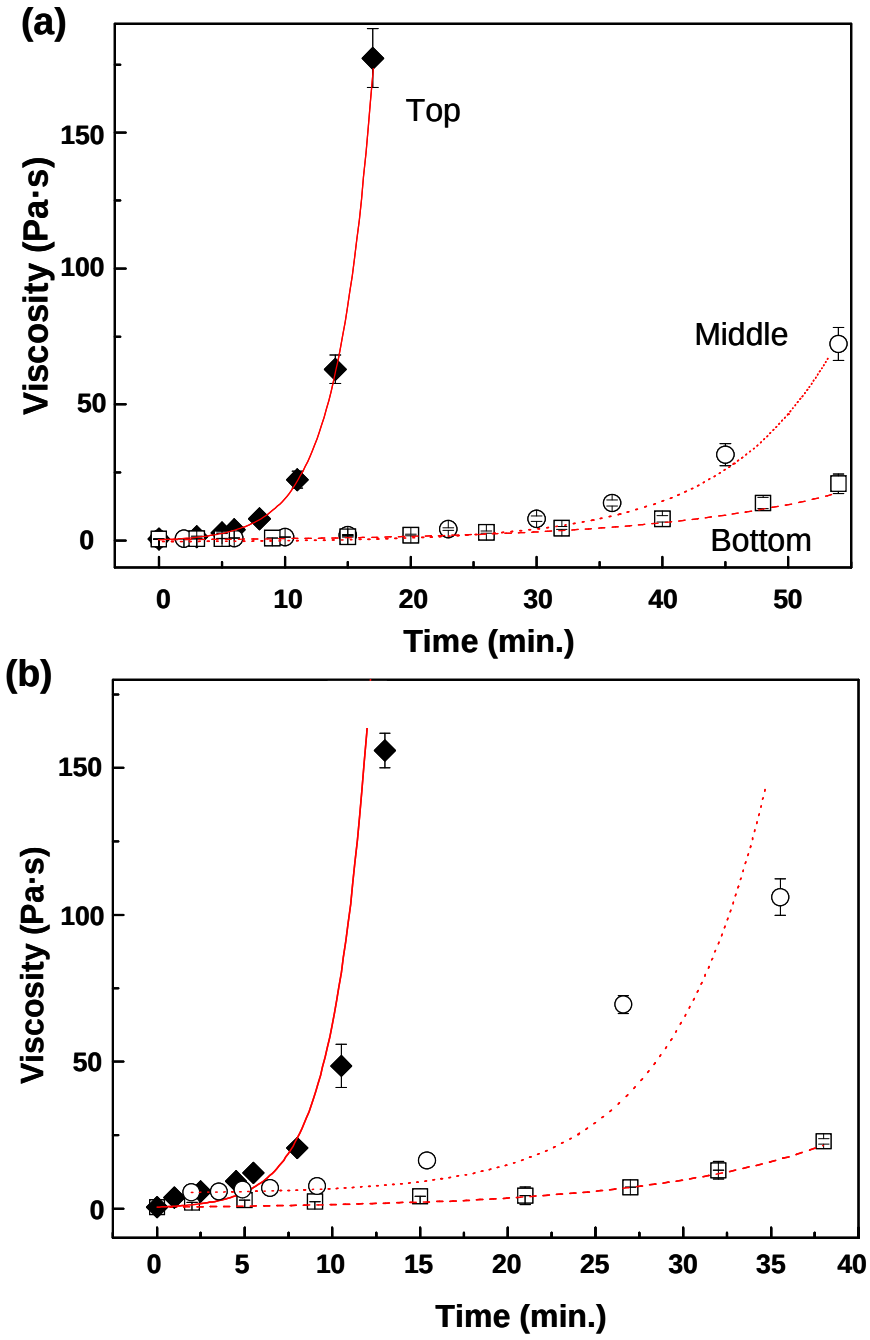

Figure 4.10 Effect of UV light intensity on the viscosity-time profile of ~80 µm epoxy coatings with 0.2 wt.% PI concentration. Coating samples were cured with a 254 nm UV lamp at room temperature with an irradiance of (a) 20 µW·cm^{-2} and (b) 1,000 µW·cm^{-2} . Equation (4.2) was used to fit the viscosity-time curves.

Table 4.3 Rate coefficient (*n*) at each depth in coatings* cured with different UV irradiance.

z position	*n* (R-squared)	
	20 μWcm^{-2}	1,000 μWcm^{-2}
z_1	0.15 (0.929)	0.25 (0.865)
z_2	0.04 (0.917)	0.06 (0.808)
z_3	0.03 (0.912)	0.04 (0.913)

* Cured with 0.2 wt. % PI using 254 nm UV lamp

The viscosity changes in epoxy coatings cured at different UV irradiances (20 and 1,000 μW·cm^{-2}) are shown in Figure 4.10, and compared in Table 4.3. Increased UV irradiance leads to faster viscosity build-up throughout the coating. The microrheology results also showed confirmable gradients at both irradiances. Changing the UV irradiance appeared to have more effect on increasing the overall curing rate than on the depthwise gradient through the coating thickness.

4.3.4 Effect of curing temperature

The effect of curing temperature on the viscosity gradient development was also characterized. A 254 nm UV lamp with a light irradiance of 1,000 μW·cm^{-2} was used to cure epoxy coatings with 0.2 wt.% PI at room temperature and 60 ^{o}C. The heater and temperature controller connected to the sample stage of the magnetic microrheometer

was used to control the curing temperature. In Figure 4.11, the microrheology data are shown, and the rate coefficient, *n* in Equation (4.2) for each position, is compared in Table 4.4. At 60 ^{o}C, overall viscosity increase was faster than at room temperature. The higher rate coefficient at each position in the coating cured at 60 ^{o}C is due to faster polymerization (i.e., higher apparent rate constant) [105]. Moreover, the measured initial wet coating viscosity was 0.09 Pa·s at 60 ^{o}C, and this initial lowered viscosity could improve the mobility of reacting species, which results in faster conversion and viscosity increase [106].

As shown in Table 4.4, the rate coefficients in the top positions were not much different at both curing temperatures; however, less spatial gradient developed, especially, between the top and middle positions in the epoxy coating cured at 60 ^{o}C. Faster diffusion of the reacting species through the epoxy coating thickness results in more uniform degree of cure. As previously discussed, wrinkling behavior on the coating surface strongly depends on the gradients developed between the top and middle positions in the coatings. Both epoxy coatings cured at high irradiance showed wrinkle defects as shown in Figure 4.12; however, the area covered by the wrinkles was much smaller in the coating with less spatial viscosity gradient cured at higher temperature.

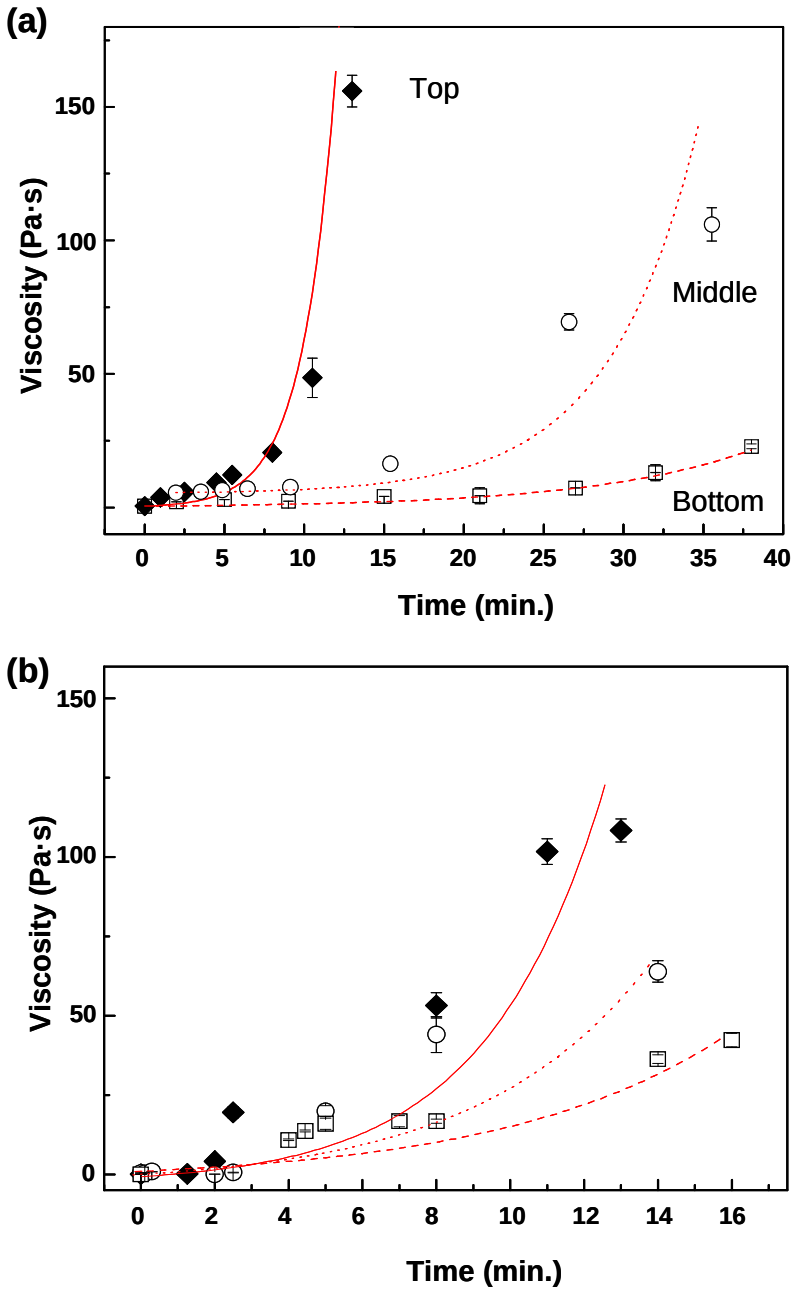

Figure 4.11 Effect of curing temperature on the viscosity-time profile of ~80 µm epoxy coatings with 0.2 wt.% PI concentration. Coating samples were cured with a 254 nm UV lamp with an irradiance of 1,000 µW·cm^{-2} at (a) room temperature and (b) 60 ^{o}C. Equation (4.2) was used to fit the viscosity-time curves.

Table 4.4 Rate coefficient (*n*) at each depth in coatings* cured at different temperatures.

z position	*n* (R-squared)	
	RT	60 ^{o}C
z_1	0.25 (0.865)	0.26 (0.834)
z_2	0.06 (0.808)	0.22 (0.801)
z_3	0.04 (0.913)	0.19 (0.815)

* Cured with 0.2 wt. % PI using 254 nm UV lamp with an irradiance of 1,000 μWcm^{-2}

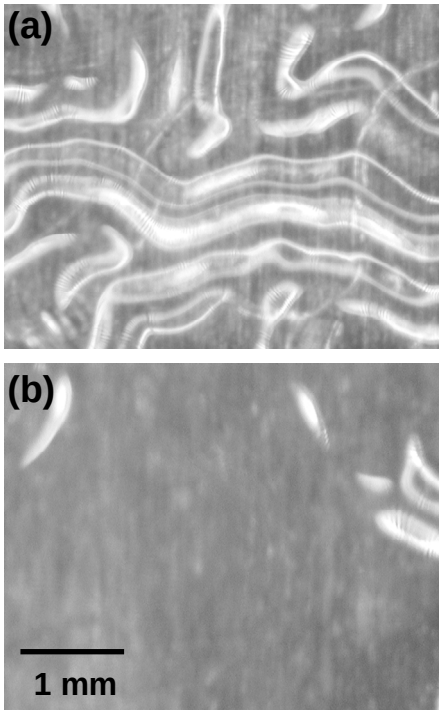

Figure 4.12 Epoxy coating surfaces after 60 minutes of curing with 254 nm and 1,000 μW·cm^{-2} UV light at (a) room temperature and (b) 60 ^{o}C. Coating thickness is ~80 μm, and PI concentration is 0.2 wt.%.

4.4 Summary

A magnetic microrheometer was used to measure coating viscosity during UV light exposure. The apparatus was used for real time monitoring of the local viscosity during UV induced cationic polymerization of epoxy coatings. The effects of photoinitiator concentrations, UV light source conditions and curing temperature were explored. Higher photoinitiator concentration and thicker coatings caused more severe viscosity gradients, which led to the formation of a skin and wrinkle defects on the coating surface. Likewise, curing with a UV wavelength that is more strongly absorbed by photoinitiator led to steeper gradients and a greater likelihood of surface wrinkles. Magnetic microrheometry results also confirmed that coatings cured at higher temperature had a lower depthwise viscosity gradient but a faster viscosity build-up. Hence higher temperature cure is preferred when fast curing and less gradient are both desired. These results are useful to design curing conditions and coating formulations to achieve desired final coating properties without defects, and understand the fundamentals of structure development in UV curing coatings.

Chapter 5. Viscosity and Surface Flow in Drying Coatings*

5.1 Introduction

Coating defects are often related to changes in the rheological properties of the applied coating liquid during drying [31, 32]. A coating liquid with lower viscosity can be beneficial for fast application and efficient leveling; however, coatings applied on a vertical or slanted substrate may 'sag' or develop drips as they dry if the viscosity does not increase quickly enough [8]. Sagging is a critical factor in determining the coating appearance in architectural coatings and automotive coatings that are applied by spraying [8, 33]. In addition, sagging may also occur when a web or substrate moves vertically upward just after the liquid is applied, as in roll coating and dip coating processes [31].

The extent of gravity-induced sagging flow on a vertical surface depends on the density, thickness, and viscosity of the coated layer [9, 32, 35]. Since the viscosity of the coated film increases substantially during drying, coating viscosity is one of the most critical factors for controlling sag. However, measuring the viscosity of coated liquid layers during drying is challenging. The viscosity of a coating liquid as a function of drying time (or solvent content) without deposition on a substrate has been studied using conventional rheometers [32, 36], and specially designed rheometers, such as modified plates [37] and T-bars [33]. These studies provide useful information; however,

* A portion of this chapter has been submitted as: Jin-Oh Song, Bryce Williams, Satish Kumar, and Lorraine F. Francis, In-situ monitoring of viscosity and surface flow in drying coatings using particle tracking experiments, Chemical Engineering and Processing Journal, 2011.

conventional methods cannot be used to follow the changes in rheological properties of coated layers during drying.

Experimental methods have been developed to characterize the extent of sagging in coatings. The sag length has been estimated by the visual inspection of dried final coating surfaces using "two color method" [8, 34] or distinctiveness of image (DOI) measurement [107]. Several attempts have also been made to monitor the amount of sagging on the coating surface with a modified sagging balance [9] or optical analysis systems [36, 108]. However, new techniques are still needed to analyze sag in diverse coating systems at smaller length scales, and to understand fundamental relationships between viscosity and sag. Specifically, *in situ* characterization methods for sagging flow and its dependence on the changes in viscosity and thickness at different drying conditions would be useful to tune drying conditions and coating formulations for efficient manufacturing of defect-free coatings.

In this chapter, micron-sized particles are tracked to characterize viscosity and sagging flow in drying coatings. A magnetic microrheometer is used to characterize the time evolution of viscosity in coatings as they dry at different temperatures. Surface smoothness is determined by both observation of the dried coating and a particle tracking-based surface flow measurement during drying. Measured viscosity-time profiles, final coating surface observations, and surface flow results are used to explore the link between the rheological properties and coating surface flow.

5.2 Experimental Section

5.2.1 Materials and methods

Coatings were prepared from aqueous polyvinyl alcohol (PVA) solution (12.1 wt.% PVA, M_w = 130,000 g/mol, Aldrich Chemical Co.). For microrheology experiments, an aqueous suspension of 1 μm superparamagnetic Fe_3O_4 particles (MS0302, MagSense Life Sci.) was dispersed in the coating solution. The particle concentration in the coating was less than 10^{-4} vol.%. The coating liquid was applied onto a pre-cleaned glass substrate using a wire-wound rod (# 50), resulting in an expected wet thickness of approximately 130 μm.

The viscosity of coatings during drying was measured using a magnetic microrheometer. Magnetic microrheology experiments were carried at various drying temperature from room temperature to 60 ^oC. Care was taken to monitor probe particle velocities at a specific position in the coatings, ~35 μm from the substrate. Measuring the velocity of a single probe particle from start to finish during drying was not practical. Instead, we collected several data points at different times from each coating specimen. Measurements were taken from more than five specimens to construct a viscosity-time profile. The schematic of magnetic microrheology for the time evolution of PVA coating viscosity is illustrated in Figure 5.1 (a).

Identically prepared aqueous PVA coatings (PVA 12.1 wt.%) were dried on a flat or inclined stage in the drying oven. The drying temperature in the oven was varied from room temperature to 60 ^oC, and the tilt angle was 7.5 ^{o}. The surfaces of the final dried

coatings samples were observed with an optical microscope to document surface smoothness. To estimate the shrinkage rate, the weight loss of coatings was also measured during drying at different temperatures on a hot plate to estimate the shrinkage rate.

5.2.2 Particle tracking for surface flow measurement

Surface flow was characterized by monitoring the velocity of lycopodium spores (diameter = 20 ~ 30 μm, Duke Scientific) on the surface of a coating mounted on an inclined sample stage, as shown in Figure 5.1 (b). The angle ($\theta = 7.5^{o}$) was set to get detectable spore velocities within a field of view during the measurements. The density of the spore (1.03 g/cm^3) is similar to that of the aqueous PVA solution; therefore, sedimentation of the spores during measurement was negligible. The spore motion on the coating surface was captured. For the results shown here, we used a lens (MX-5040Z Normal) that spans magnification from 50× to 400×. The spore motion was captured continuously. Velocity was determined by tracking the positions at each frame using Image J Plug-in (v. 1.41, NIH). The continuous velocity data was used to calculate the sag length during the drying process of PVA coatings.

Sag length is primary quantity that affects the final film appearance, and previous studies determined critical sag length by observing final surface appearance [34]. The sag length is smaller than the determined critical sag length, sagging defects are invisible.

Equation (5.1) describes the sag length and its dependence on the changes in coating viscosity and thickness during drying process:

$$Sag \quad length = v_{surface} t = (\frac{\rho g h^2}{2\eta} \sin\theta) t \tag{5.1}$$

where $v_{surface}$ is measured surface velocity, t is the drying time, g is the gravitational constant, and ρ, h, and η are the density, thickness, and viscosity of PVA coatings, respectively. θ is an inclined angle of the coating samples to induce a gravity driven flow during drying.

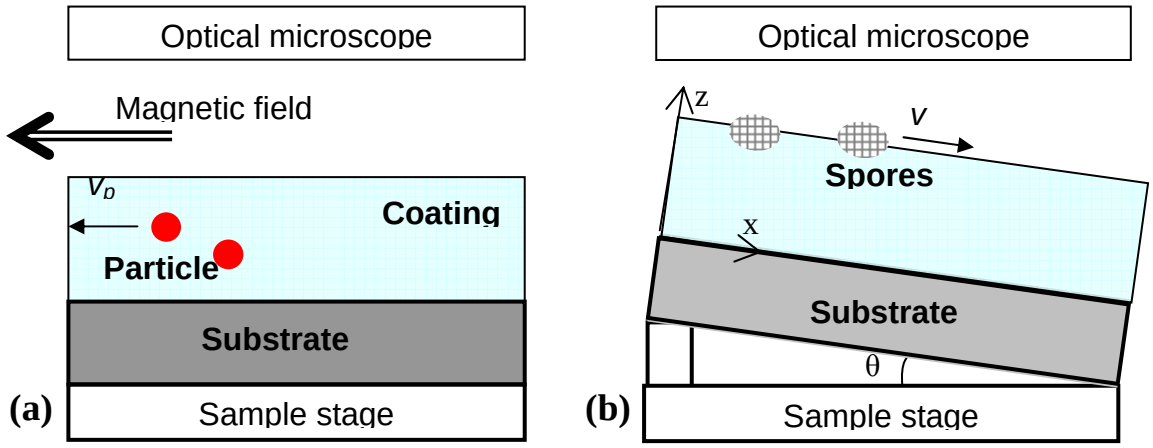

Figure 5.1 Schematic of (a) the magnetic microrheology for coating viscosity measurement and (b) spore motion tracking on a coating surface without magnetic field for sag length measurement on a tilt (θ = 7.5°) sample stage. The sample stage has channels for air/gas flow, and is connected to a heater with temperature controller.

5.3 Results and Discussions

5.3.1 Viscosity and surface of drying PVA coatings

Figure 5.2 shows the change in particle velocity and calculated viscosity of a 12.1 wt.% PVA coating during drying at room temperature. As water evaporates, the measured particle velocity decreases from 0.67 µm/s to 0.03 µm/s after 28 minutes. The calculated viscosity increases from less than 1 Pa·s to over 11 Pa·s over this time period. During evaporation, the PVA concentration increases and therefore the viscosity increases. From experiments on bulk solutions, the coating viscosity should increase according to a power law as the concentration increases [6]. The microrheology data shows the expected significant viscosity increase at the later stages of drying.

The particle velocity within a fixed focal plane was used to construct the viscosity-time profile. Data collection was stopped when the particle velocity became too slow to follow. The *z* position of the focal plane was chosen to be far enough away (~35 µm) from the substrate to minimize 'wall effect' on the particle velocity [93, 103]. The presence of the substrate adds to the drag force on the particle and a correction factor is needed in Equation (3.6) to account for the effect if the particle is within ~28 particle diameters of the substrate [103]. Another factor that must be considered is the presence of concentration gradients. During drying, the polymer concentration may become higher at the surface. Particles were monitored at a fixed position through the thickness so that the measurements would show the effect of drying time or the overall concentration increase.

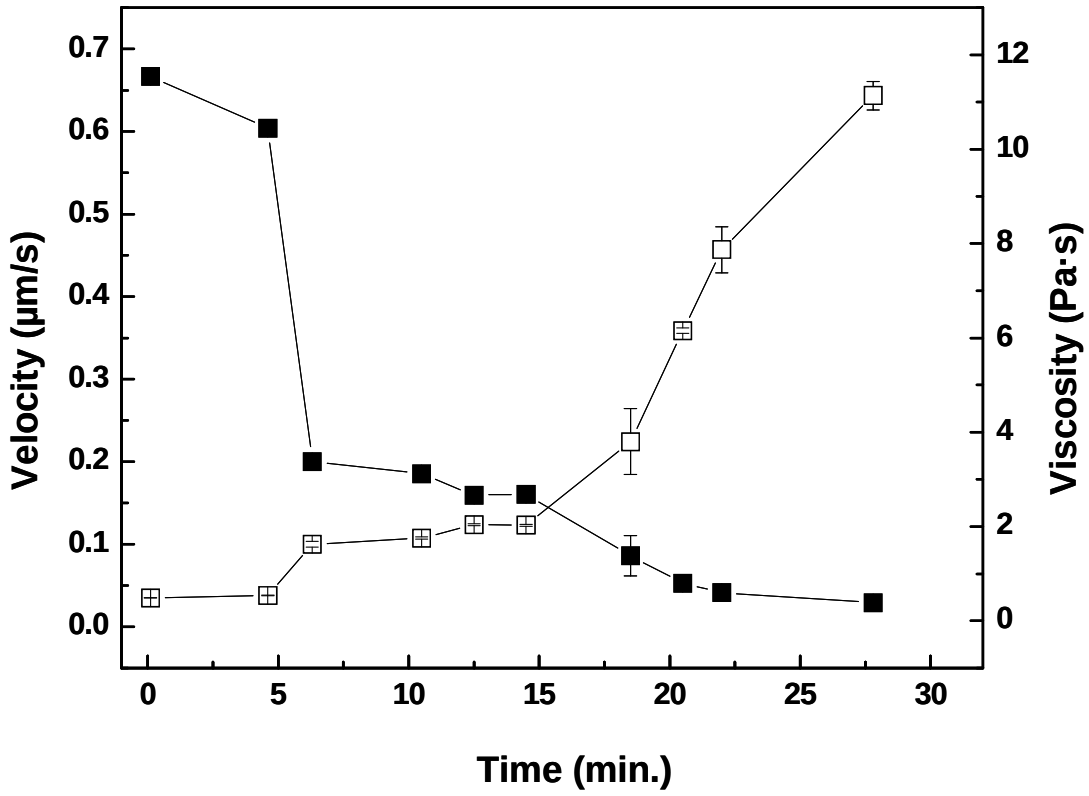

Figure 5.2 Particle velocity changes (solid square) in PVA coating and calculated viscosity (open square) of PVA coating as a function of drying time.

Figure 5.3 shows the particle velocities and viscosities of coatings dried at different temperatures. The measured particle velocity fell off more rapidly with time at higher drying temperatures, leading to a steep increase in viscosity. As drying temperature increases, the evaporation rate increases and hence the concentration of PVA goes up more rapidly with time. Therefore one expects the viscosity to increase faster. An additional factor, however, is the temperature itself. At higher drying temperature, the viscosity of the coating at any particular concentration is lower. The data show that there is a characteristic time for each drying temperature where the viscosity increases dramatically. These viscosity build-up times ($t_{build\text{-}up}$) are marked. The measured $t_{build\text{-}up}$ decreases with increasing drying temperature. The same trend was found in our previous results for 5.08 wt.% PVA coatings [103].

Images of the surfaces of PVA coatings dried on a flat substrate and an inclined substrate are shown in Figure 5.4. The PVA coating sample dried at room temperature on the flat stage (Figure 5.4 a) shows sufficient leveling without sagging, while the sample dried on the titled stage at room temperature (Figure 5.4 b) has visible accumulation of coating at the bottom of the specimen. The dried surfaces of PVA coatings also show sagging when they are dried on a tilted stage at 40 ^{o}C (Figure 5.4 c). However, sagging was prevented at drying temperature of 50 and 60 ^{o}C (Figure 5.4 d and 5.4 e). These results revealed that drying at 50 ^{o}C was sufficient to prevent sagging for this particular coating thickness and incline. Hence, $t_{build\text{-}up}$ at 50 ^{o}C can be considered as the time needed for the viscosity to build in order to prevent sagging. Interestingly, the $t_{build\text{-}up}$ may be useful in finding the time required for a coated film to be 'dry-to-touch' [33].

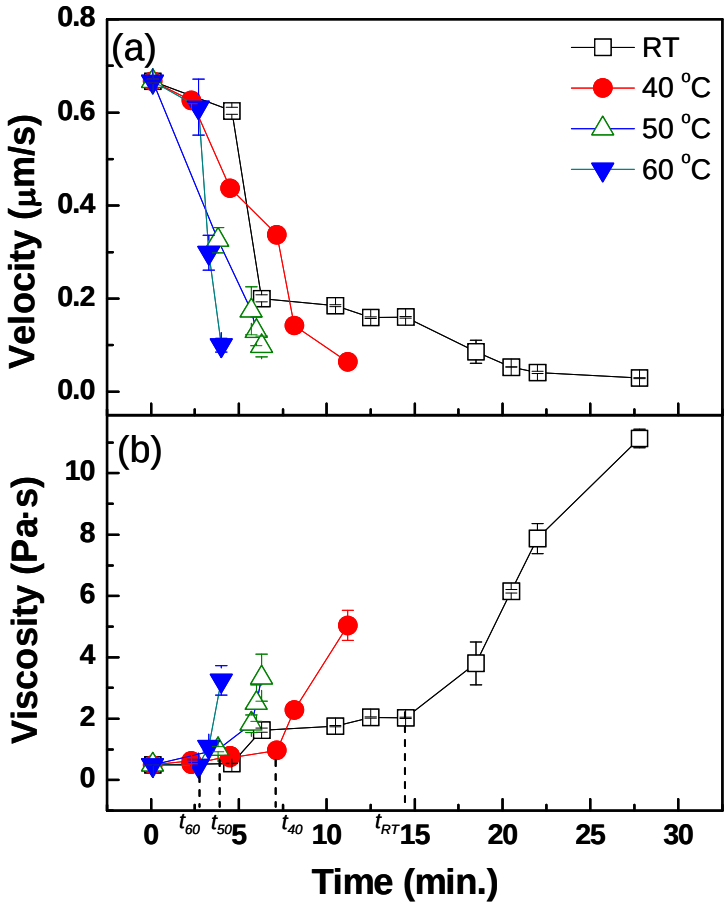

Figure 5.3 (a) Magnetic particle velocities measured at different drying times and tempeartures for a 12.1 wt.% PVA coating. (b) Coating viscosities calculated from the velocity data using Eq. (1). The viscosity build-up times at the various temperatures are marked.

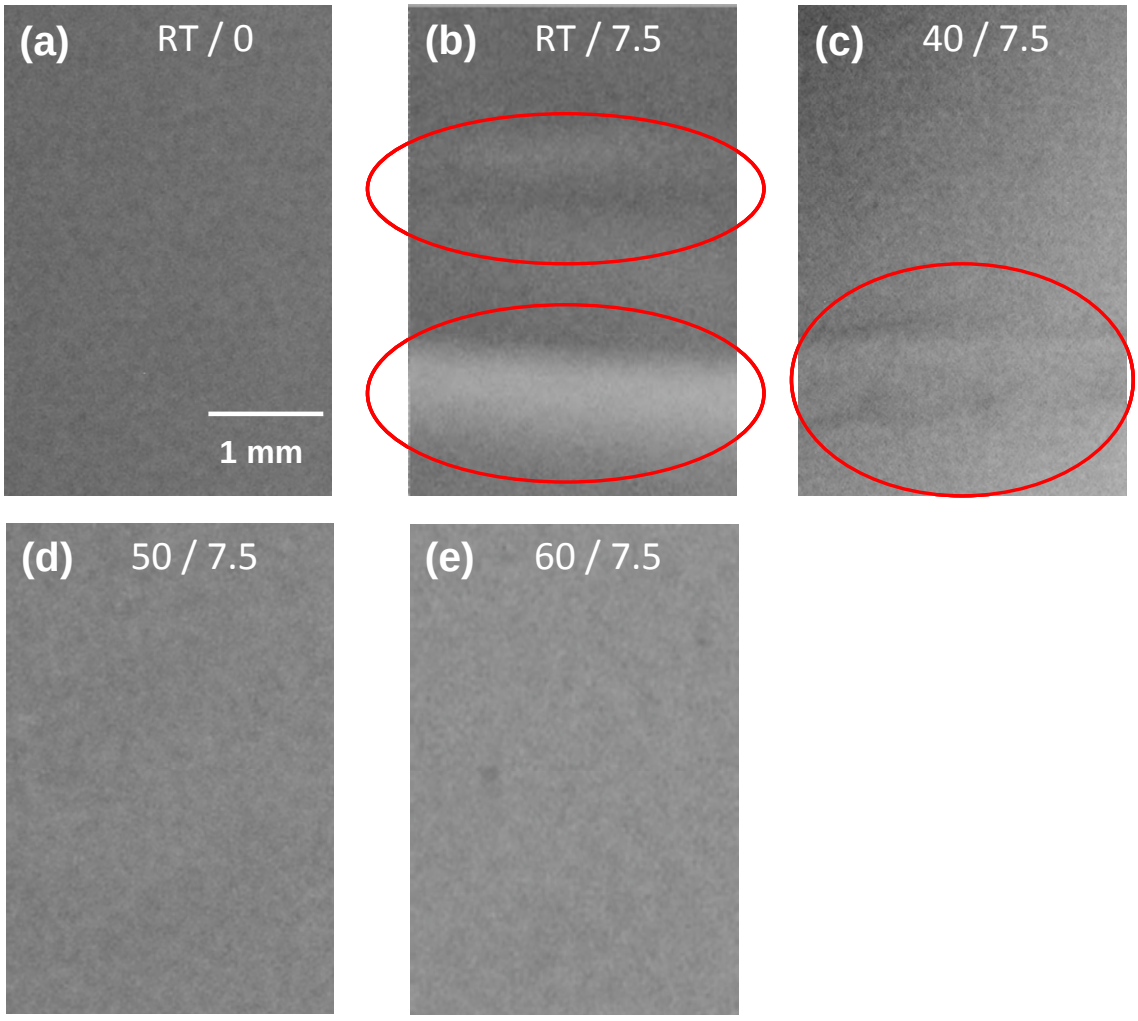

Figure 5.4 Final dried surfaces of 12.1 wt. % PVA coatings dried at different drying temperatures on flat or titled stage [drying temperature (^{o}C) / tilted angle (^{o})]. A circle shows uneven surfaces.

5.3.2 Analysis of sag length

For more quantitative analysis, surface flow velocity was determined from tracking the velocities of the lycopodium spores on the coating surfaces. The spore motion on the coating surface was driven by gravity induced flow of the coating; therefore, the spore velocity data tracked the coating surface velocity during drying. Figure 5.5 shows the spore velocity changes on 12.1 wt.% PVA coating surfaces as a function of drying time at different drying temperatures. The sag length (i.e., the distance traveled by the spore in a given time period) was determined by calculating the area under the spore velocity- drying time curve. As the coating dries at room temperature, the velocity decreases linearly from 8 μm/s to zero. At higher drying temperatures, the velocity first increases slightly before decreasing. The initial increase in velocity is likely due to an initial decrease in viscosity as the coating is heated. The sag length at room temperature is about 4 mm, which is long enough to detect sagging visually on the dried surface. However, the sag length at 60 ^{o}C is less than 0.8 mm, and sagging was not detected visually as shown in Figure 5.4 (e).

Previous studies determined critical sag length by observing final surface appearance or quantifying DOI [34, 107]. When the sag length is smaller than the critical sag length, sagging defects are invisible or DOI is higher than 80; under these conditions, coating surfaces are considered to be acceptable [34, 109]. Our particle tracking experiments can be used to accurately measure the sag velocity and predict the sag length for acceptable coating surface appearance under different drying conditions.

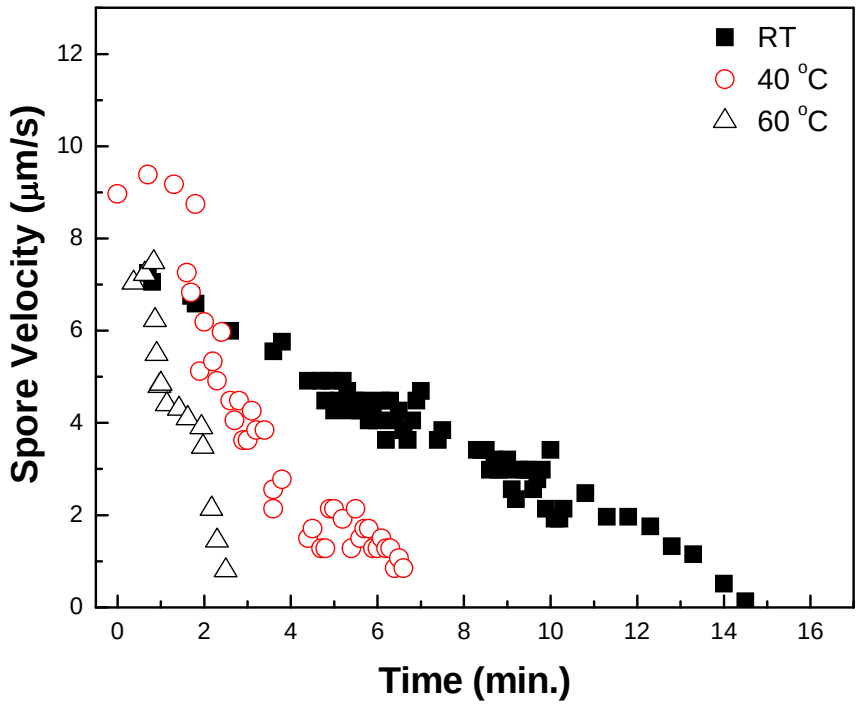

Figure 5.5 Measured spore velocities on 12.1 wt.% PVA coating surfaces as a function of drying time to calculate sag length changes during drying at different temperatures. Measurements are taken on a tilted sample stage.

The surface velocity using the lycopodium spore motion is influenced by the changes in coating thickness and viscosity at different drying temperatures. In Figure 5.5, the surface velocity decreases more rapidly when the coating dries at higher temperatures due to faster viscosity increase and thickness shrinkage, resulting in shorter sag length. The time for the surface velocity to drop to zero falls from ~ 15 minutes for room temperature drying to ~3 minutes for 60 ^{o}C drying. This time period is quite close to $t_{build\text{-}up}$ at each drying temperature in the viscosity-time profile in Figure 5.3, indicating that the tracking surface velocity itself can be useful to determine the time period for significant viscosity increase to prevent sag in drying coatings as well as the sag length. These particle tracking experiments will be useful for quantifying the length scale of sag over a broad range of drying conditions and coating material systems. They are also ideal for comparison with theoretical models of coating flow.

5.3.3 Effect of free surface on particle tracking

The magnetic particle within the focal plane is initially far from the coating surface; however, as drying proceeds, the free surface approaches the focal plane as illustrated in Figure 5.6. Berdan and Leal [110] predicted the effect of a fluid interface on particle drag; for a liquid/gas interface, the drag is reduced, but only when the particle is within one diameter of the interface. To determine if this occurred in our microrheology experiments, the position of the free surface was estimated using the initial evaporation rate determined from weight loss experiments.

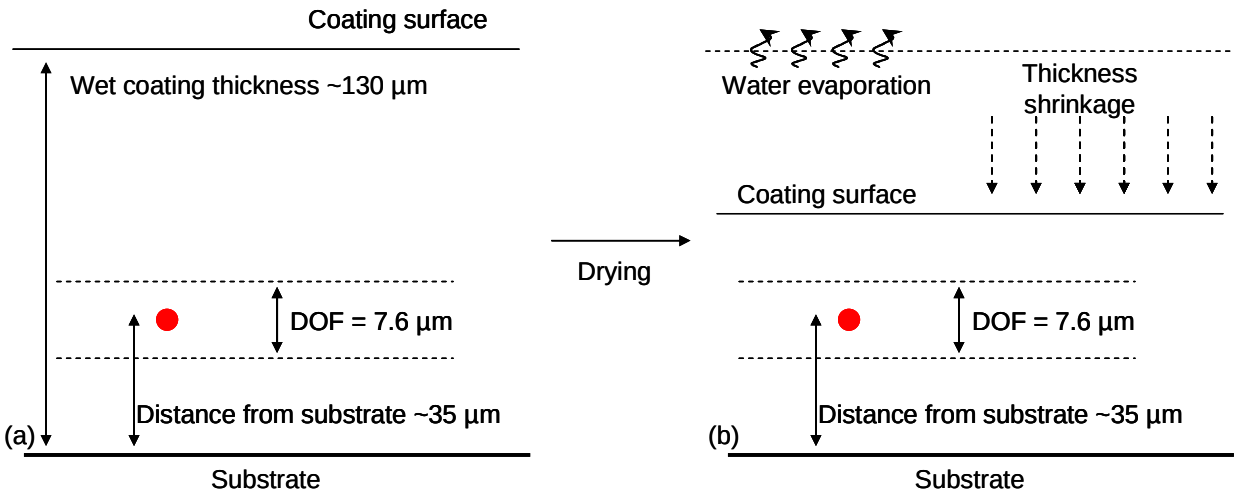

Figure 5.6 Illustration of the positions of coating surface and the probe particle within a focal plane (a) in an initial wet coating and (b) in a drying coating with thickness shrinkage.

Table 5.1 Coating thickness decease as a function of drying temperature from the mass loss measurement of 12.1 wt.% PVA coatings.

Temperature (^{o}C)	Rate of shrinkage (µm/s)
28	0.023
40	0.190
50	0.408
60	0.568

Table 5.1 shows the effect of the drying temperature on the estimated thickness shrinkage. The distance between the focal plane and the coating surface as a function of drying time at different temperatures is plotted in Figure 5.7, using the shrinkage rate in Table 1. Based on from the expected thickness of wet coatings, the initial position of the free surface was estimated to be ~130 μm from the substrate (Figure 5.6). The shrinkage rate at room temperature was slow enough so that particle velocity measurements were completed (i.e., particle velocity dropped below a critical value required for tracking) before the free surface came close to the focal plane.

However, at higher drying temperatures, the free surface approaches the tracked magnetic probe particle more rapidly, and this may interfere with measurements in the later stage of drying. For example, the last data point collected for the sample dried at 40 ^{o}C occurred at ~11 minutes in Figure 5.3, while the shrinkage rate data at 40 ^{o}C predicts the intersection with the focal plane after 8.3 minutes during drying. Likewise the final data points collected at 50 and 60 ^{o}C may have occurred after the coating surface intersected the focal plane. The actual times when the free surface meets the probe particle during magnetic microrheology experiment may be different than those computed with shrinkage rates in Table 5.1 because the weight loss was measured in a separate experiment, not on the sample stage of the magnetic microrheometer.

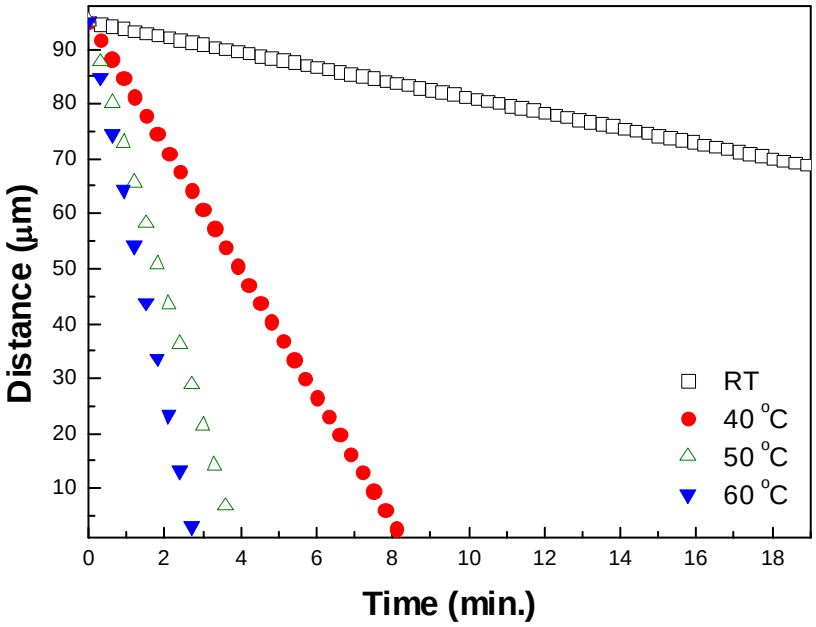

Figure 5.7 Distance between coating surface and focal plane as a function of drying time at different temperatures.

5.4 Summary

Magnetic microrheometry was used for *in situ* characterization of viscosity of PVA coatings during drying at different temperatures. Particle velocity changes in the drying coatings were tracked to follow the time evolution of the PVA coating viscosity. The coating thickness shrinkage rate during drying was also estimated since the probe particle may interact with an evaporating coating surface during the particle tracking. The viscosity-time profile showed the temperature dependence on $t_{build\text{-}up}$, and compared with the final surface observation results to investigate sagging on the coatings. Sag length change was also measured continuously using tracking lycopodium spore motions on the surface of drying PVA coatings. The methods for tracking sag length will be useful to quantify the effects of drying conditions on surface irregularity, and to investigate the sag length at micron length scale on smaller coating products, such as medical stents or guidewires. These real-time particle tracking data of the changes in viscosity and sag length can be used to find process windows or critical combinations of processing variables for improved final coating products, and as inputs to more comprehensive models.

Chapter 6. Microstructure Evolution in Drug-Polymer Coatings

6.1 Introduction

The characterization of coating structures in medical devices, such as drug-eluting stents (DES) is important to elucidate the drug microstructure evolution and stability through the products' life cycle. The microstructure of drug-polymer coatings can be affected by drying conditions (temperature and air/gas flow) or sterilization process condition (temperature and humidity) after drying process. The coating structure needs to be predictable and stable over a wide range of environmental conditions for desired final function of the coatings. The function of DES strongly depends on both the amount of total drug released and how the drug is released over time, and these can be affected by stent design, formulation, the structure of drug or surrounding polymer, and the amount of residual solvent [12, 13]. The drug morphology at the coating surface is critical for the device performance since the interface between the coating surface and human tissue affects biocompatibility [38]. Therefore, it is important to understand the structure of drug under various process conditions to control the coating product quality for biomedical applications. This will also provide better understanding of fundamentals in solidification phenomena in drug-polymer coating systems.

Various analytical methods have been used for physical or chemical mapping of the drug-polymer coating structure to investigate the correlation between drug elution profile and the spatial distribution or contents of drug, such as atomic force microscopy

[41, 42], near infrared and Fourier transform infrared imaging [43, 44], electron spectroscopy for chemical analysis (ESCA), and time-of-flight secondary ion mass spectrometry (TOF-SIMS) [38]. These techniques provided useful information on quantitative chemical analysis, however, the coating samples were characterized after the final structure development thorough solidification process, such as drying.

The structure development of drug-polymer coatings involves a range of physical or chemical phenomena, such as the nucleation or aggregation of drug particles, polymerization, and phase separation during solidification [45]. It is important to monitor the microstructure evolution in drug-polymer coatings to study kinetic parameters for nucleation or growth of drug phase since the desired drug structure is essential for the clinical efficacy of DES [12, 45]. The development of *in situ* analytical techniques, referred to as process analytical technologies (PATs) has improved the capability of in-line monitoring of complex dynamic characteristics of pharmaceutical products. Raman spectroscopy has been used as a reliable quantitative tool in PATs [45]. It has been used for process monitoring and control in pharmaceutical industry due to its advantages, such as non destructive and real time manner, fast data acquisition, and minimum sample preparation for the characterization [46].

Confocal Raman microscopy, a combined tool with an optical microscope, has the potential for the characterization of the structure evolution in DES, since it provides non-destructive chemical imaging of component distribution in drug/polymer mixtures with high chemical specificity and spatial resolution. The size and spatial distribution of drug phase in drug-polymer coatings has been characterized to investigate the effect of

formulation and process conditions on the final performance of DES using confocal Raman microscopy [38]. The method was also used for real-time imaging of surface morphology of drug-polymer coatings during drug release to study the correlation between drug elution profile and coating microstructure [111].

In Chapter 6, confocal Raman spectroscopy was integrated with a portable drying chamber in order to image the drug microstructure of coated thin-film samples *in situ*. The drying chamber was designed to control the nitrogen gas temperature and flow rate passing over the sample such that the residual solvent evaporation rate was solely based on convective mass transfer. Based on the evaporation rate of various solvents and coating formulations, the time scale of drying process and scans for chemical imaging was determined. The time evolution of drug size and distribution was investigated, and its dependence of drying rate and sterilization conditions was also discussed.

6.2 Design of apparatus for *in situ* confocal Raman microscopy

6.2.1 Mass loss measurement system

The rate of volatility and diffusivity of each solvent can affect the drug-polymer microstructure in the coating as the solvent diffuses and evaporates into the vapor phase. Therefore, evaporation rate of coating formulation needs to be quantified to generate right process window for real-time monitoring. A main control unit (PAU Unit, Apiste) for temperature, relative humidity (RH), and air flow adjustment was connected with a drying tunnel. The range of controllable temperature is 15 ~ 35 ^{o}C and that of RH is 20 ~ 100 %. A drying tunnel is connected with the main unit and a digital balance (Microbalance, Mettler Toledo) to measure the mass loss in pure solvents and coating formulations. The mass loss data is collected automatically every 1 second. Figure 6.1 shows the schematic and pictures mass loss measurement system.

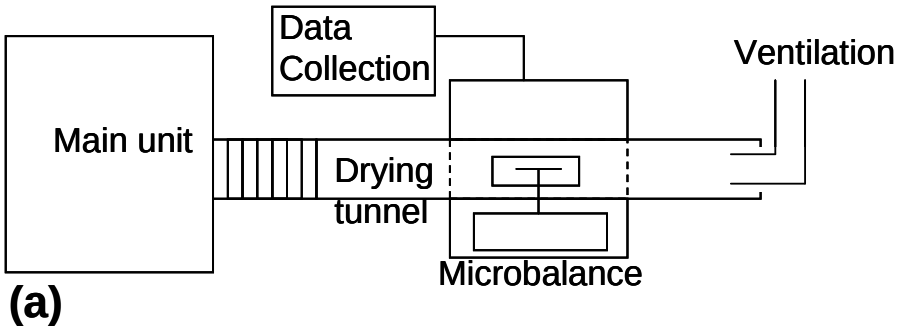

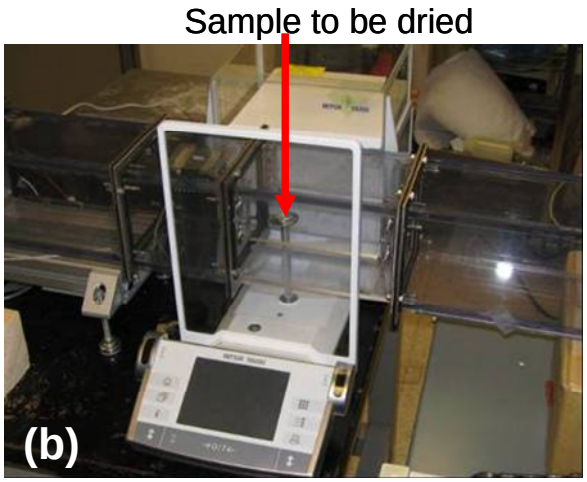

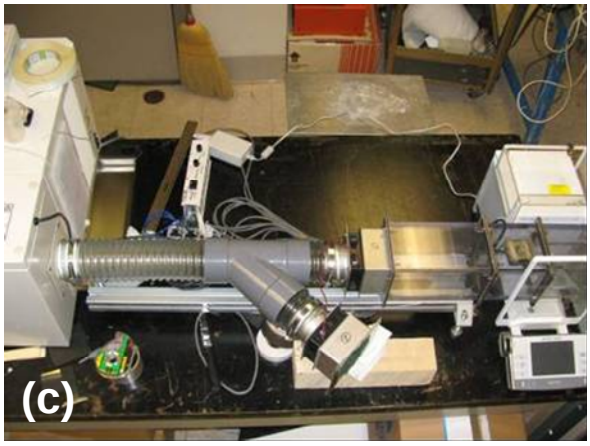

Figure 6.1 (a) Schematic of mass loss system and pictures of (b) microbalance and (c) drying tunnel connected.

6.2.2 Drying channel

A portable drying apparatus is required for the integration with Raman microscopy to investigate the effect of drying conditions on the coating structure. Figure 6.2 (a) shows the designed drying channel for coating sample preparation, *in situ* confocal Raman microscopy, and drying process through the air/gas inlet. The temperature controller system was also built using an air process heater (AHP-3741, Omega Engineering Inc.) and a digital process controller (CN3243, Temperature controller, Omega Engineering Inc.) for a controlled microenvironment, such as temperature and air/gas flow rate. The temperature range using the system is from room temperature to 540 ^{o}C. The integrated experimental system for *in situ* confocal Raman microscopy measurement is illustrated in Figure 6.2 (b).

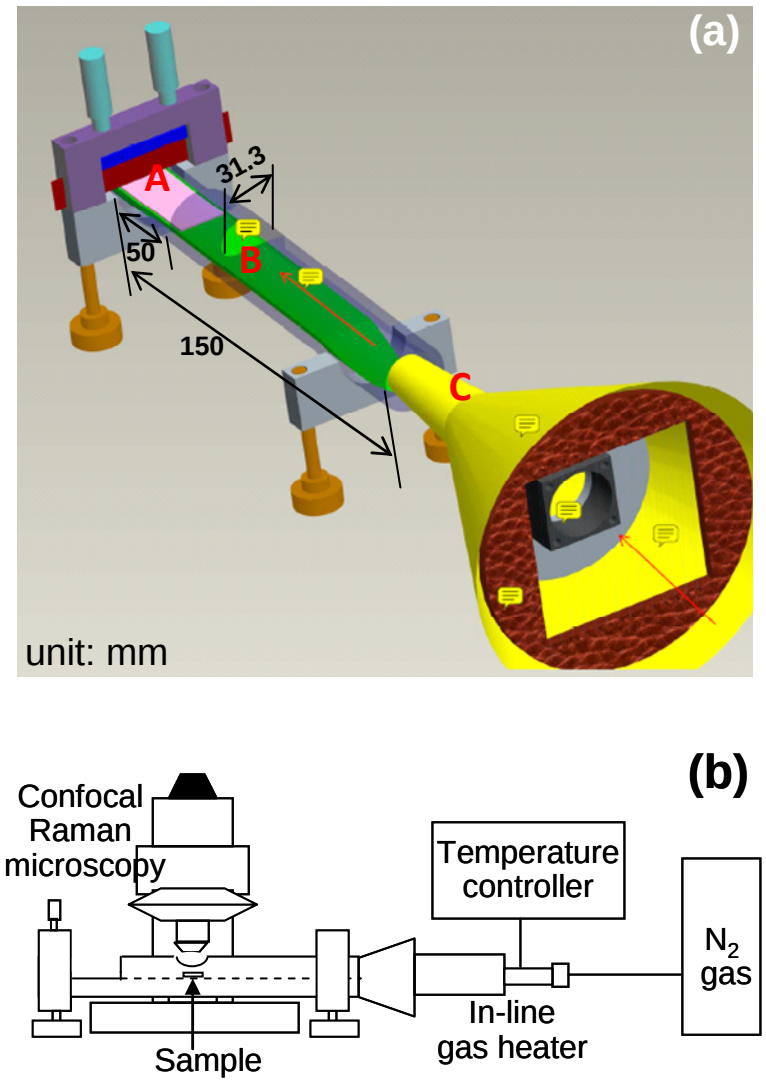

Figure 6.2 Schematic of (a) a portable drying apparatus, and (b) experimental set-up (not to scale) of confocal Raman microscopy with a drying apparatus and a temperature control system. A: stage for coating sample preparation, B: hole for confocal Raman microscopy, and C: air/gas inlet.

6.3 Experimental Section

6.3.1 Materials and methods

Mass loss of various solvents and coating formulations were measured to quantify evaporation rates at different drying conditions. All solvents and coating formulations for this study were provided by Boston Scientific Inc. Solvents used for the mass loss measurements are cyclohexanone, tetrahydrofuran (THF), and dimethylformamide (DMF). Some of solvent mixtures were also measured to distinguish the evaporation rate difference at each early and later stages of drying. Coating formulations consist of drug, polymer, and THF:DMF solvent mixtures. Indomethacin or everolimus is used as drug powder materials, and surrounding polymer matrix is biodegradable polymer, poly(lactic co-glycolic acid) (PLGA).

Coating samples were prepared using Mayer rods (#3, 5, 10, 18, and 26) for various thickness. For film preparation, highly reflective ferroplate or stainless steel substrates were cut into 25 x 25 mm^2 and flattened for good repeatability during film draw downs. With this draw down technique, both the surface and bulk characteristics could be replicated to match stent coating designs including similar drug loading and drug microstructure. Temperature controlled nitrogen gas was used for both drying and sterilization process, and the drying temperature was from room temperature to 100 ^oC to study the effect of drying rate on the microstructure.

6.3.2 Confocal Raman microscopy

As a result of system integration, the resulting coating phase separation mechanics can be analyzed over time in fixed lateral or cross-sectional regions of interest using confocal Raman microscopy. The Confocal Raman microscope (WiTec CRM-200) combines a green Argon laser (excitation wavelength, 514.5 nm and laser power, 11mW) with a high-powered spectral camera such that resolution down to 220 nm is possible [112]. The instrument used an X-Y translational scan table to move the sample laterally within +/- 3 nanometer steps and has a focusing resolution of 10 nm. Single Raman spectra were collected reasonably fast using an integration time of 50 milliseconds in order to produce either 9 µm x 9 µm area scans or 9 µm x 15 µm depth scans in less than 2 minutes each. The lateral areas were captured using multiple line scans in the X-Y plane, and similarly the depth scans were completed with microscope control in the Y-Z plane up to 20 µm coat thickness. The Raman analysis was an excellent technique to resolve the drug morphology since it can be filtered to specific wavelengths based on either drug or polymer chemical bonds from their unique excitation spectra. The signal intensity of the drug peak at spectral position 1610 ~ 1670 cm^{-1} (Figure 6.3 a) was based on a triene functional group [112]. Multiple polymer wavelengths were investigated based on their unique chemical bond structure including, however, the polymer did not provide a strong enough signal over the short integration times to provide meaningful data. In Figure 6.3 (b), the drug regions were represented by the brightest regions, while the polymer areas were darker and surrounded the drug areas.

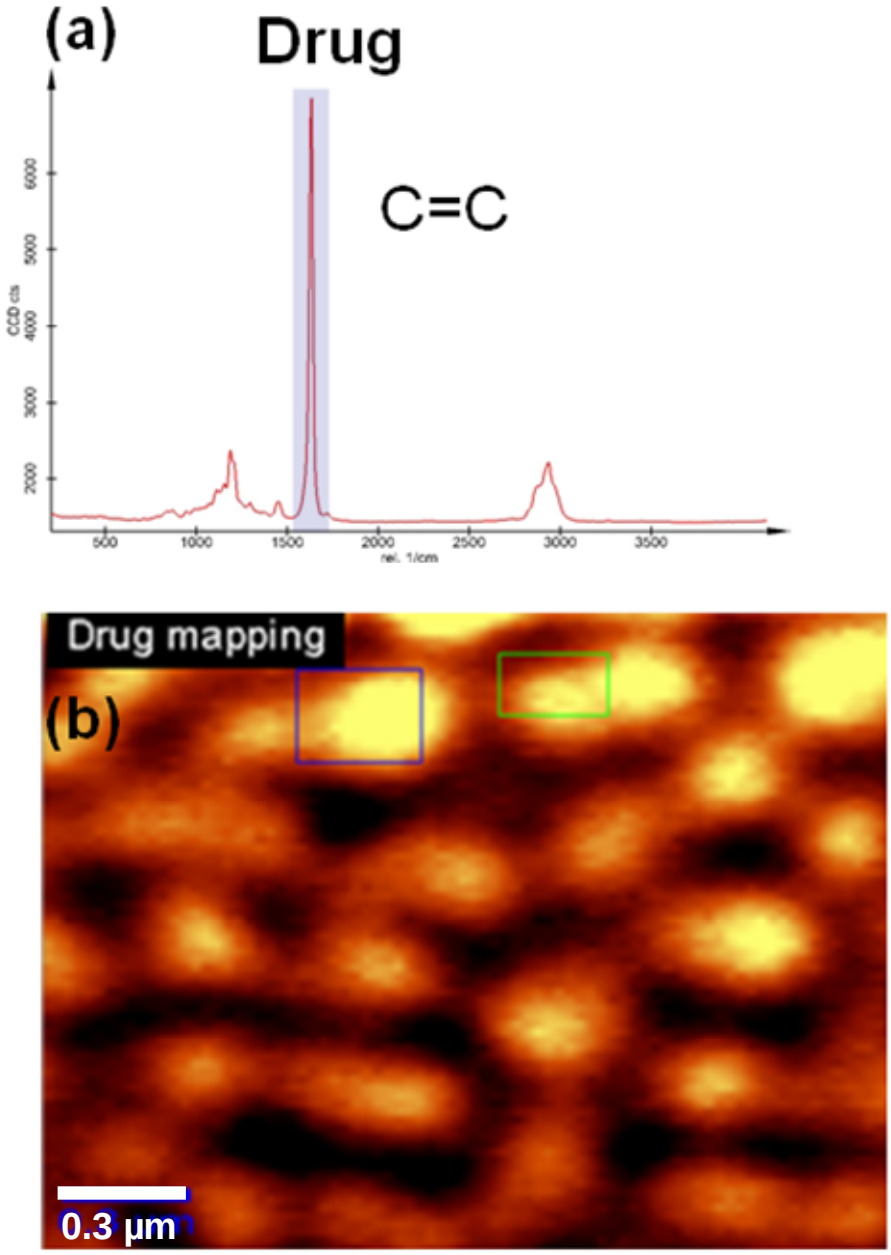

Figure 6.3 (a) Raman spectra of drug and (b) example chemical mapping of drug-polymer coating using lateral scan.

6.4 Results and Discussion

6.4.1 Quantification of evaporation rate

Using this system, the mass loss of pure and mixed solvents were measured to determine the evaporation rate, and summarized in Table 6.1. Since THF and THF:DMF mixtures showed higher initial mass loss rate during the early stage of drying, two different (early and late) mass loss rates were determined based on the point where the slope decreased significantly. The result shows the most volatile solvent is THF, and DMF shows the slowest evaporation. Figure 6.4 shows that solvent evaporation is increased by forced drying with higher temperature and gas flow, and the solvent mixtures show how more volatile solvent is dominant at early drying stage. Biodegradable polymer and solvent mixtures were also measured in Figure 6.5, and higher solids concentration formulations show slower drying rates. In the later sage with lower evaporation rate, solvent may be trapped due to skin formation at the coating surface. This quantified experimental data is useful to estimate the time scale of structure development, and also provides a right process window for both coating drying and real-time monitoring of drug-polymer coating structure.

Table 6.1 Mass loss rate of various solvents and mixtures

Solvent or mixture	Early mass loss (µg/sec)	Late mass loss (µg/sec)	Conditions (^{o}C / m/s)
THF	836.9	404.1	24 / 0
DMF:THF 1:3	461.1	10.8	23.2 / 0
DMF:THF 1:3 (FH)	1068.1	61	35 / 0.58
DMF:THF 3:1	114.2	11.4	23.7 / 0
Cyclohexanone	25.2	n/a	23.6 / 0
DMF	12.4	n/a	23.5 / 0

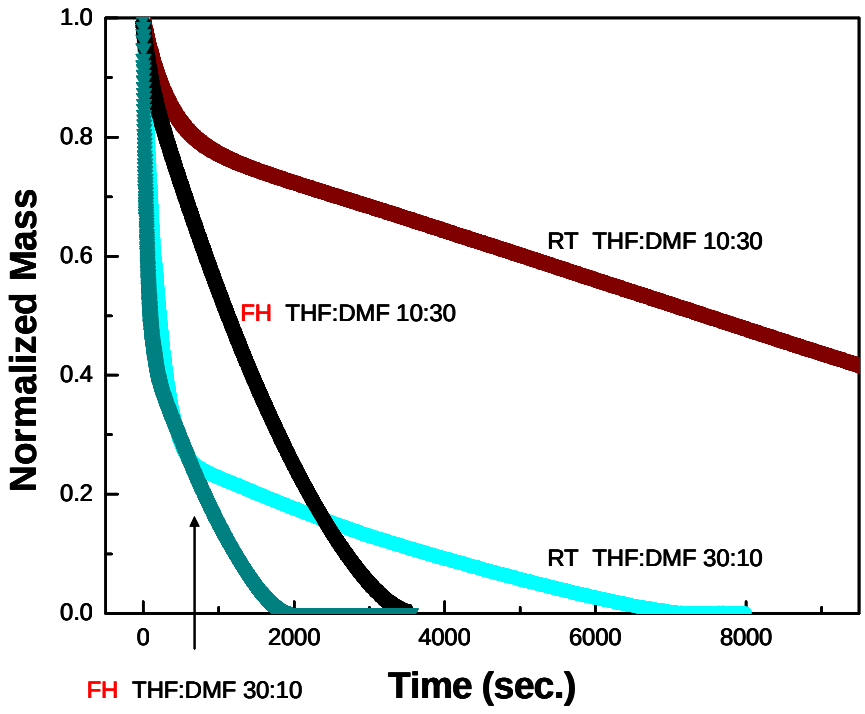

Figure 6.4 Normalized mass loss of solvent mixtures at room temperature and forced heat (FH) drying conditions.

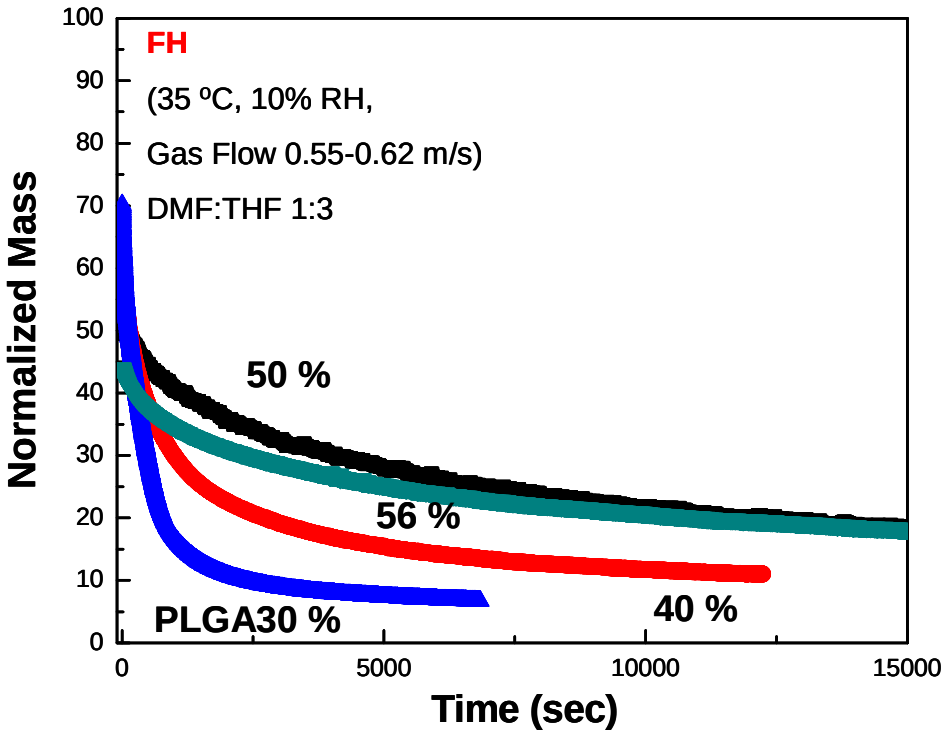

Figure 6.5 Amount of solvent remaining in coating formulations (PLGA / DMF:THF) as a function of drying time and solid (PLGA) concentrations.

6.4.2 Characterization of drug domains

For system validation, the final dried coating samples were characterized using confocal Raman microscopy, and compared with scanning electron microcopy (SEM) results to check if the method can be used to distinguish the difference in drug domains in coatings dried at different temperatures. Figure 6.6 show that the drug domain size is larger when the samples are dried at room temperature, compared to the size dried at 90 ^{o}C. This trend agrees well with SEM data, and clearly shows the temperature dependence of drug size and distribution within the final dried drug-polymer coatings.

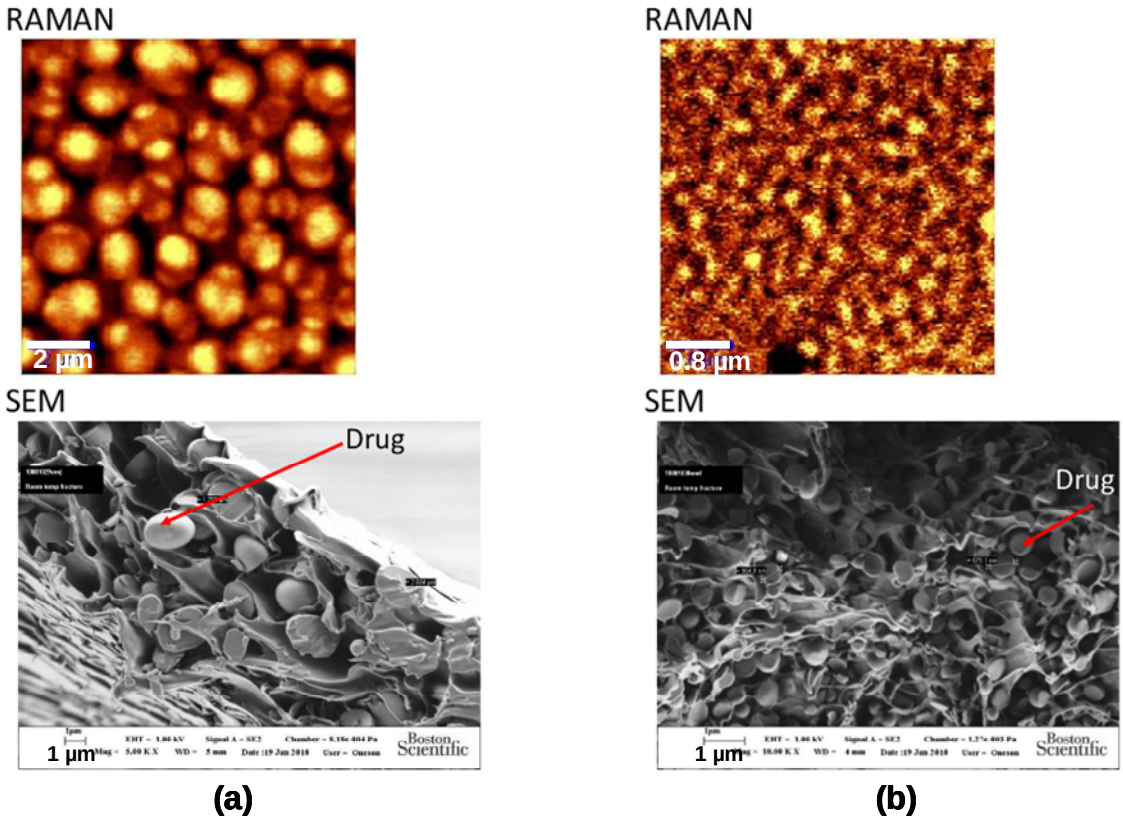

Figure 6.6 Raman lateral scan and cross-sectional SEM images drug-polymer coatings dried at (a) room temperature and (b) 90 ^{o}C.

Experimental confocal Raman microscopy data was used to capture the microstructure evolution in thin-film coatings during drying at room temperature. In Figure 6.7, high magnification of lateral scans taken at ~2.5 µm below the coating surface, describe the reordering of the drug domains. As lateral scans were continuously recorded every minute, a single particle gradually tracks across the image and sinks in-plane. This provides the evidence of particle mobility in both horizontal and vertical planes due to the gradual elution of residual solvent from the coating surface.

As show in Figure 6.8, nucleated drug particles are initially nano-dispersed throughout the bulk, with a relatively homogenous structure in the first 15 minutes. As it dries, the drug domains become more ordered and evolve with an apparent directionality that begins to create well-aligned vertical channels of surrounding polymer matrix. After 50 minutes, the drying front begins to halt further ingress into the coating and the drug domains are compacted near the surface. The bulk structure shows extended drug domains. A denser drug region was observed to collect near the surface. During drying at room temperature, there were significant coating morphology change in real-time, and the confocal Raman microscopy depth scans were able to illustrate the directionality and growth of drug domains. *In situ* confocal Raman microscopy also revealed that the drug domain distribution shows both a vertical packing and a distribution that contributes to a surface coarsening over time. The depth scan data showed more vertical orientation across the drug phase, and micro-channels that can result in further bulk drug access to the coating surface during drug release.

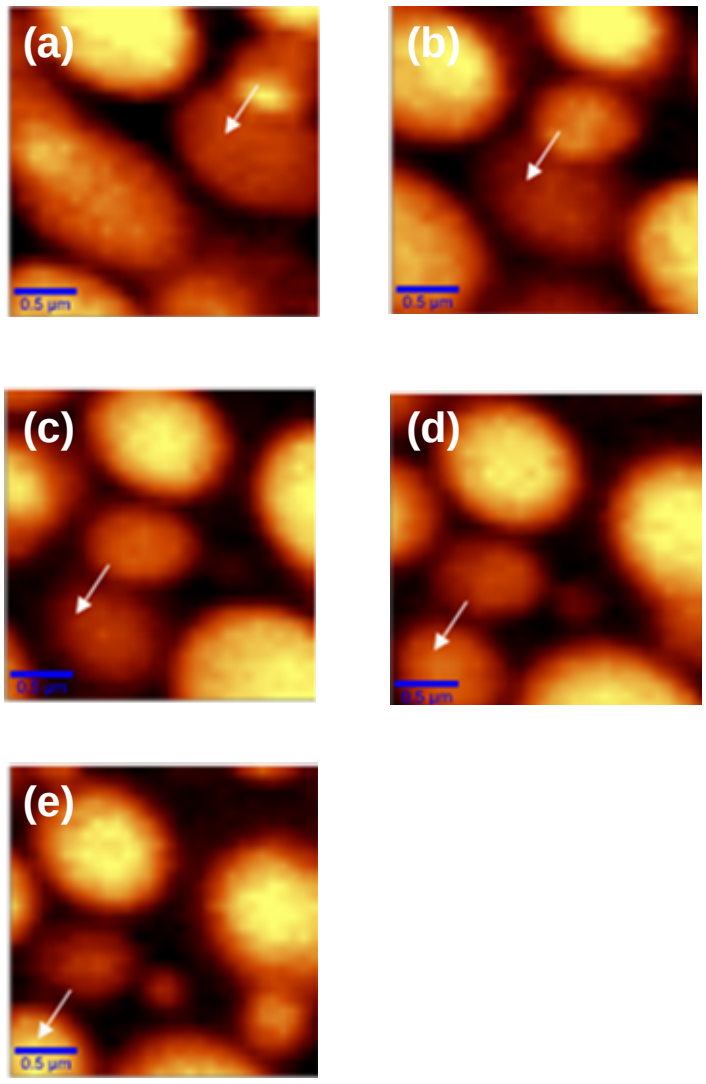

Figure 6.7 Real-time Raman imaging of drug domains in the coating during drying at room temperature (RT) for (a) 37, (b) 38, (c) 39, (d) 40, and (e) 41 minutes using lateral scans at a fixed position (~ 2.5 µm from surface after 37 min. drying at RT). The arrow indicates the direction of the lateral motion of a drug domain.

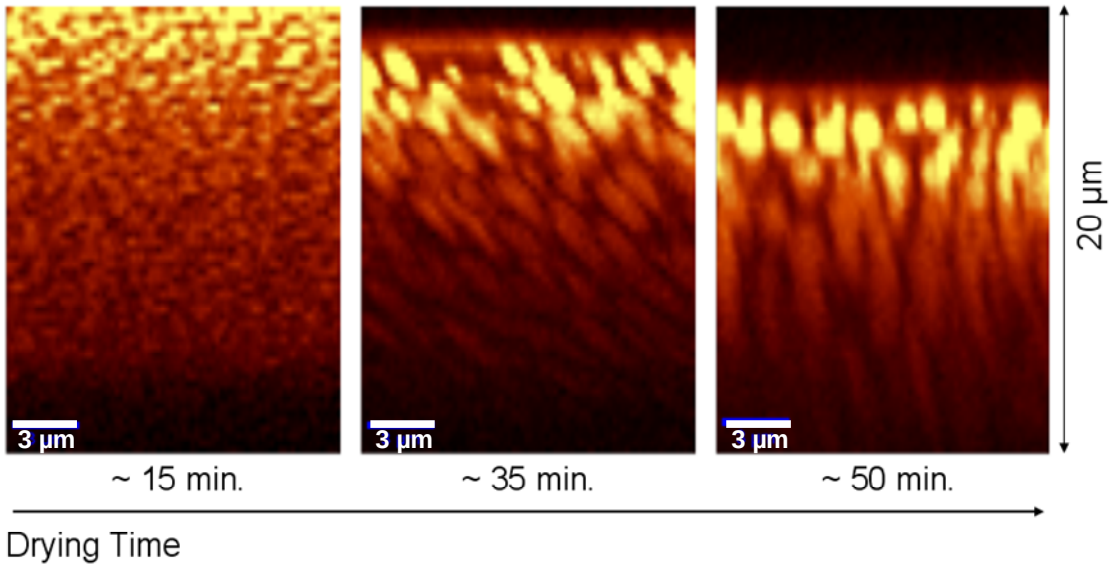

Figure 6.8 Real-time Raman imaging of vertical drug distribution through the coating thickness during drying at room temperature.

6.4.3 Effect of drying rate on structure development

The drying rate does influence the amount of residual solvent within the coatings, resulting in different thickness shrinkage rates, and drug domain sizes and distributions. Figure 6.8 showed that the drying front is perpendicular to the film surface, and the shrinkage rate of the film thickness is measured as a function of drying time in Figure 6.9. For both stagnant and convective gas flow conditions, the coating thickness decayed linearly (fast-steeper slope) within the drying time investigated during morphology development. The nitrogen gas flow tangential to the coating surface increased the solvent removal rate, and the shrinkage rate increased to 5.1 nm/s (1.4 nm/s without the nitrogen flow). This linear decay response agrees well with previous one-dimensional drying theory, where the coating thickness is driven by solvent concentration at the surface [18].

In Figure 6.10, the drying rate of thin-film coatings drastically affects the overall mean size of the drug domains. If the solvent is removed from the thin-film more quickly at higher drying temperatures, the particle mobility is arrested shortly after drug-polymer separation. However, as the drying rate gradually slows down, the drug microstructure reveals a coarsening in the domain size at lower drying temperatures. Drug domain size results are summarized in Figure 6.11. The mean drug domain size was observed to increase in diameter during slow drying cycles as the residual solvent provided an external force for particle mobility and clustering dynamics. The largest drug domain is created by a slow-drying process at room temperature.

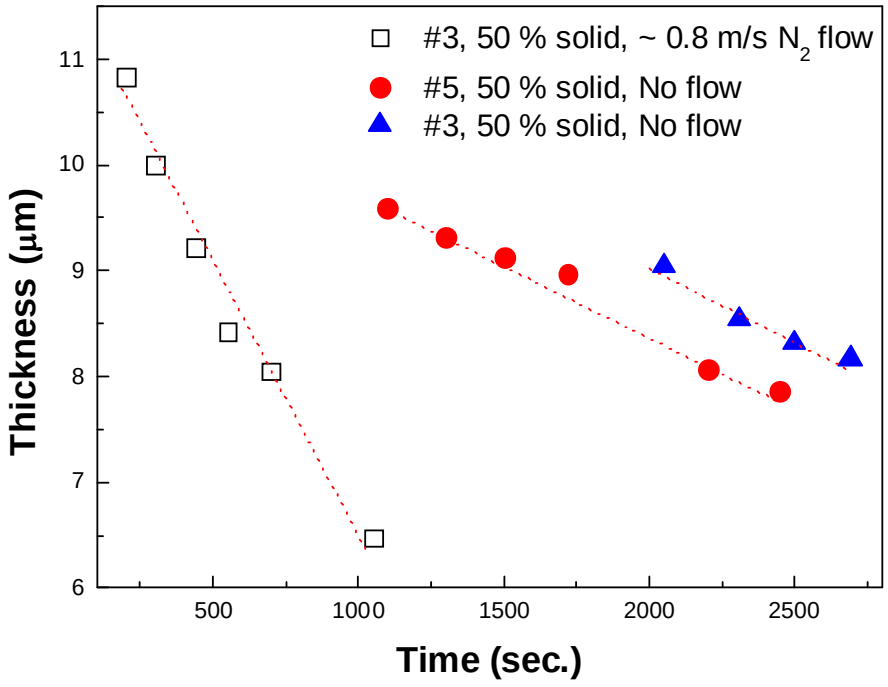

Figure 6.9 Drying front evolution and thickness shrinkage rate determined using real-time Raman depth scans of drug-polymer coatings during drying. Coatings were prepared using different Mayer rods (# 3 and # 5), and dried at room temperature with or without nitrogen flow.

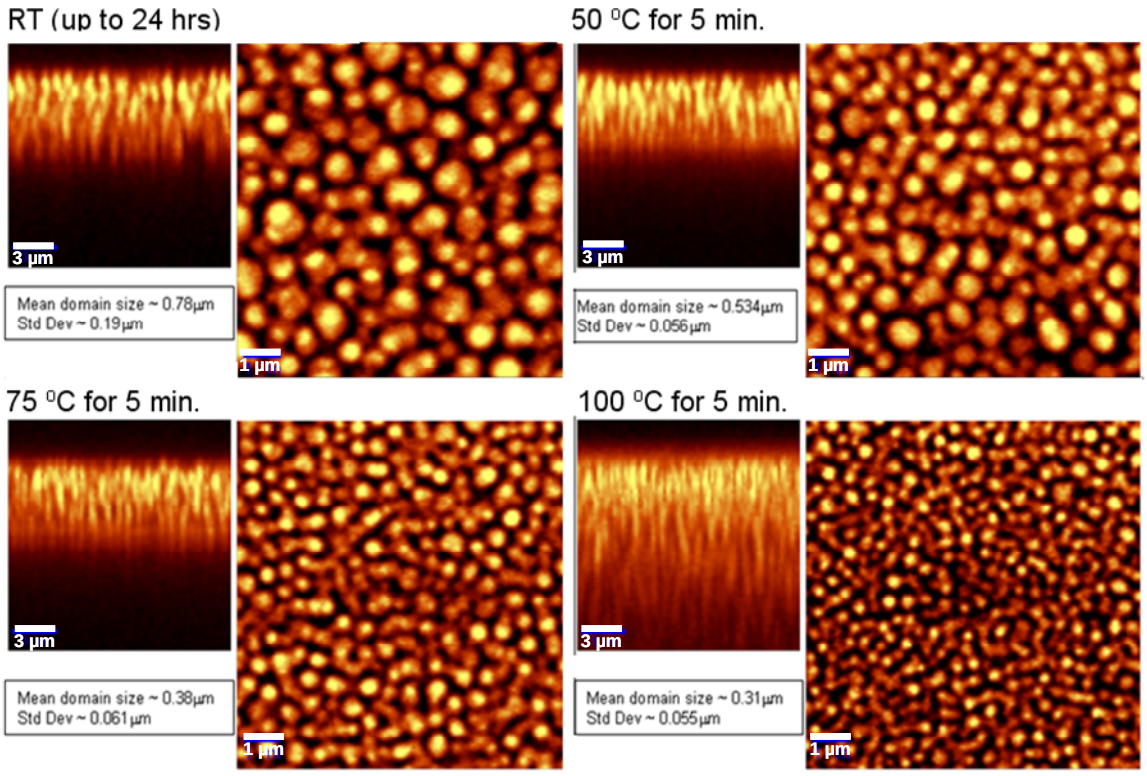

Figure 6.10 Changes in drug domain size and distribution due to changes in drying temperature.

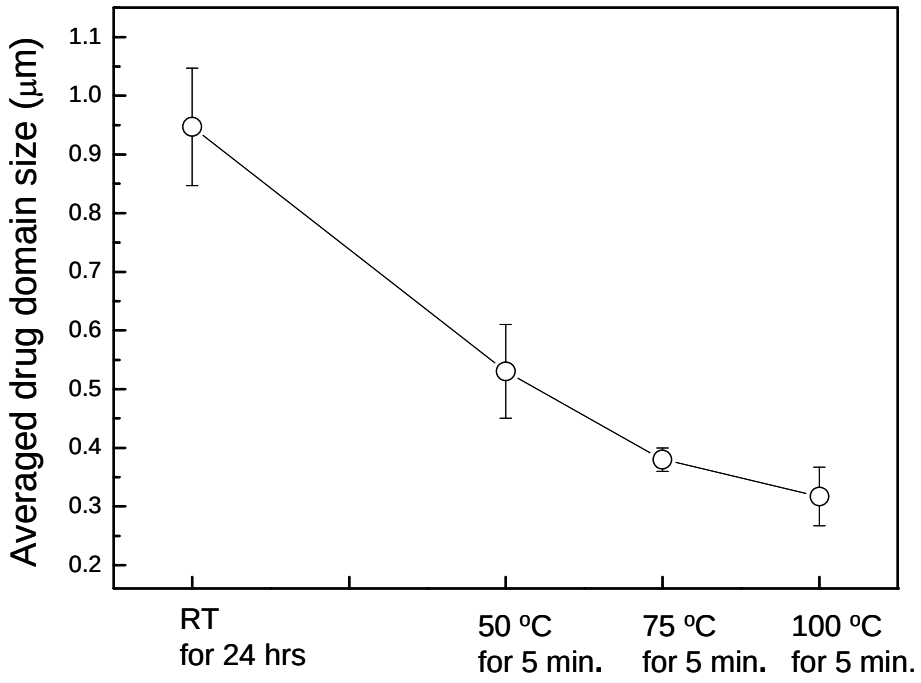

Figure 6.11 Averaged drug domain size change as a function of drying conditions.

Slower solvent removal enabled a gradual agglomeration of drug particles into larger domain size, while the domain size was reduced with faster solvent removal. The coatings dried at room temperature for 24 hours have about three times larger drug domain size than those dried at 100 ^{o}C for 5 minutes. Slow drying rate of thin-film coatings can enable aggregation and coarsening of the drug connected phases both at the surface and through the bulk. As drying rate decreases, the surface drug can combine to form a thicker overall skin. Likewise, a long drying phase in the bulk can enable further growth of drug-rich domains that lead to larger drug domain sizes.

The Raman depth scans in Figure 6.10 also show different intensity of drug-rich regions that can affect the drug elution rates over time. Drug elution based on surface drug concentration can affect early release, depending on the formation and thickness of the coarsened skin layer. The size and distribution of bulk drug can drive late release, based on the diffusion rates through the surrounding polymer shell or surface access via an interconnected network of channels. The level of surface-accessible drug regions can be tailored by drying conditions, showing different concentration of drug species at the surface and the degree of domain size and interconnections through the bulk.

6.4.4 Effect of sterilization process

The effect of the sterilization process on the microstructure was also investigated to understand the stability of the drug-polymer coating under moderate temperature cycles. The drug-polymer coating products generally require robust response to extreme

swings in environmental conditions during storage and aging. As the product is sterilized, the increased temperature above glass transition and humidity can change the drug and polymer microstructure as well as the drug elution rate. A small chamber was designed for the conditions recreated a 'mock-sterilization' cycle, and the process allowed the polymer to absorb water and potentially change its corresponding drug miscibility. Mock-strelization process used a controlled temperature and humidity microenvironment to elevate the thin-film coating above its thermal glass transition temperature.

Figure 6.12 shows the changes in the drug-polymer morphology and drug domain sizes after sterilization. The change in the drug-polymer morphology following mock-sterilization (Figure 6.12 b) shows an elevated drug domain sizes. The post-sterile samples increased in drug size, primarily due to the surrounding polymer swelling initially upon humidity exposure. The lamella structure coarsened into well-defined spherical domains surrounded by polymer shell. The sterilization process allowed the drugs to diffuse and aggregate again through more relaxed surrounding polymers due to the increased temperature and humidity. The increase in domain size in the bulk drug would lower its overall concentration density, leaving a lower elution rate unless supplemented by an increase in surface accessible drug or surface layer thickness. The curved surface shown in Figure 6.12 (b) is due to the delamination of the film. *In situ* confocal Raman microscopy in this study can monitor any changes to the coating microstructure induced from environmental conditions to determine any sensitiveness to humidity or temperature.

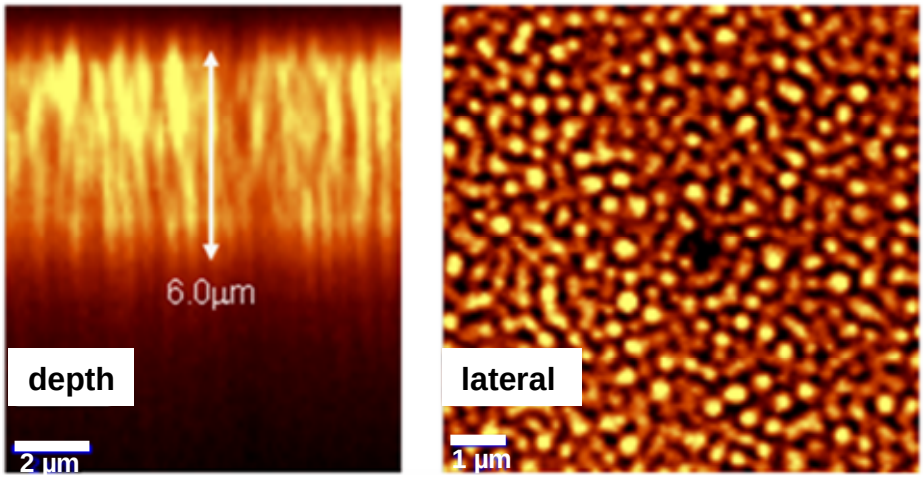

(a)

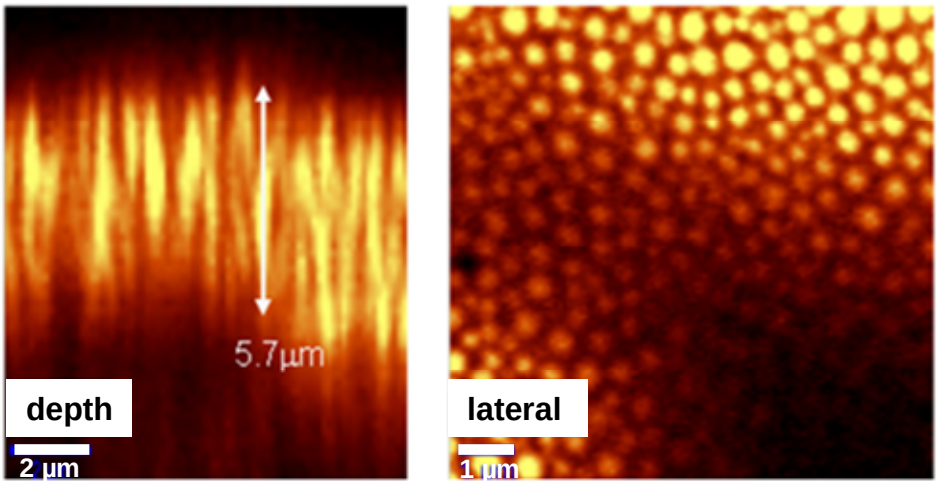

(b)

Figure 6.12 Depth and lateral scans of (a) pre-sterile and (b) post-sterile drug-polymer coatings. Pre-sterile coatings was dried at 95 ^{o}C for 5 minutes and the dried sample was sterilized at 55 ^{o}C for 30 minutes with 99 % of relative humidity.

6.5 Summary

In situ confocal Raman microscopy method was developed by an integration with the drying apparatus that we designed for controlled drying conditions. The evaporation rate of various coating formulations was determined to estimate the time scale of structure development and real-time monitoring. The size and distribution of drug domains were monitored by depth and lateral scans during drying to investigate the development of microstructure in drug-polymer coatings during drying. The effect of drying rate on the thickness change, drug particle mobility, and drug size and distribution were investigated to elucidate and optimize the process conditions and coating formulations. Larger drug domain sizes were observed as the coatings dried at a lower temperature. The changes in the microstructure of drug-polymer after sterilization process was also characterized using confocal Raman microscopy to predict the stability of DES. Increased temperature and humidity enabled drug phases to diffuse and re-aggregate through more relaxed surrounding polymer matrix, showing increased domain sizes.

Chapter 7. Future Work

7.1 Introduction

A magnetic microrheometer has demonstrated that the time evolution and spatial gradients of coating viscosity can be characterized using the magnetic particle velocity change under an applied external magnetic force. The coating viscosity was determined from the force balance equation between the magnetic force and the drag force. The apparatus uses two permanent magnets to manipulate the magnetic probe particles to generate strong and constant magnetic force which results in the lateral motion of probe particles with detectable constant velocities. The lateral motion of probe particles was monitored using the optical microscope at different depths into coatings. These particle manipulation and imaging methods were capable of tracking detectable particle motions to get coating viscosity information during solidification processes, however, the modification of current experimental set-up will be beneficial for more efficient *in situ* coating viscosity change characterization.

The current set-up has several limitations and issues need to be addressed to broaden its capability of characterizing the local rheological properties of various coating systems. Magnetic manipulation method using permanent magnets in the current design can adjust magnetic field gradient up to ~70 T/m which is high enough to characterize coating viscosity of ~1,000 Pa·s with ~1 μm diameter particles. Coating viscosities generally increased dramatically and became out of measurement range during our drying

or UV curing process while the coatings are still fluid-like. In addition, the manipulation is not suited to generate oscillatory or pulsed magnetic force for viscoelastic property characterization. Coating samples prepared in our previous experiments also had limitations. They should be optically clear and thick enough (>20 μm) to get reliable viscosity information as they solidified. Therefore, novel experimental strategies are also required to characterize more various coating systems, such as thin particulate coatings for batteries or medical devices.

In Chapter 7, alternative system designs and experimental strategies are discussed to enhance the functionality and utility of our current magnetic microrheometry for coating research. This chapter also deals with several issues during previous magnetic microrheology experiments in drying coatings, and experimental works with the improved analysis method and additional equipment set-up to overcome the issues.

7.2 Alternative System Design

Another method for the magnetic probe particles is the electromagnet configuration that is technically more challenging to set up. Electromagnets, rather than the permanent magnets in the current design, provide some advantages. They allow the adjustment of magnetic field gradient strength during the experiment. As a coating dries or cures, its viscosity climbs; hence, the optimal magnetic field gradient for measurement increases with time. Electromagnets have been used to control the magnetic field strength and generate gradients conveniently up to 100 T/m [66]. It will be one of the manipulation methods to move the magnetic probe magnetic particle detectably in high viscous medium.

The magnetic field can be varied in time, either as a step function or in sinusoidal oscillation, so that the viscoelastic properties can be determined [64,82]. Coating materials are not typically simple viscous liquids; therefore, the added insight from complex rheological data may be helpful in both probing the changing nature of the coating as it solidifies and designing the processing changes that are needed to address coating problems. Since an adjustable magnet stage was already built in the preliminary work, an electromagnet-based set-up would make use of the same microscope and platform as the current system, however, the permanent magnets would be replaced with electromagnets and the associated control and cooling equipment for the electromagnets will be added. A cooling system will be required if the applied current is high enough to generate substantial heat on the magnet core.

The electromagnet configuration can be used to study various rheological properties of materials using different particle manipulation methods. One experimental method is a creep experiment in which a field is applied in a step function for a specific period of time and then turned off. In this case, the motion of the probe particle is used to find the viscosity and the creep compliance of the liquid. Another method is an oscillation experiment, which gives a complex modulus. For materials in the linear viscoelastic regime, the shear rate dependence of viscosity can be determined from oscillatory measurements. In addition, measurement of other interesting phenomena, such as yield points and time dependent behavior, like thixotropy, and other materials, such as nanoparticle-based dispersions, are also of interest in the development of the electromagnet-based apparatus.

Our previous experiment results showed that the permanent magnet configuration is not suited to characterize nanoparticle-based coating systems. In this experiment, the magnetic probe particles were tracked within in anionic silica particles (D= ~20 µm)/water system (20 wt.% silica particles), and the interaction between silica particles and the probe particles made the particle tracking analysis more complex. Surrounding silica particles were piled up around the probe particle during the particle tracking experiment without drying, and it retarded the probe particle velocity as if the coating viscosity increased. Figure 7.1 (a) illustrates the effect of surrounding silica particles on the particle velocity. The aggregation of silica particles affected not only the particle velocity but also the particle trajectory. The particle trajectory was significantly influenced by surrounding silica particles while they are aggregating. The observed probe

particle in Figure 7.1 (b) shows a diagonal trajectory that cannot be used to characterize local coating viscosity. This issue in the nanoparticle-based system can be addressed using the oscillatory magnetic force with the electromagnet set-up.

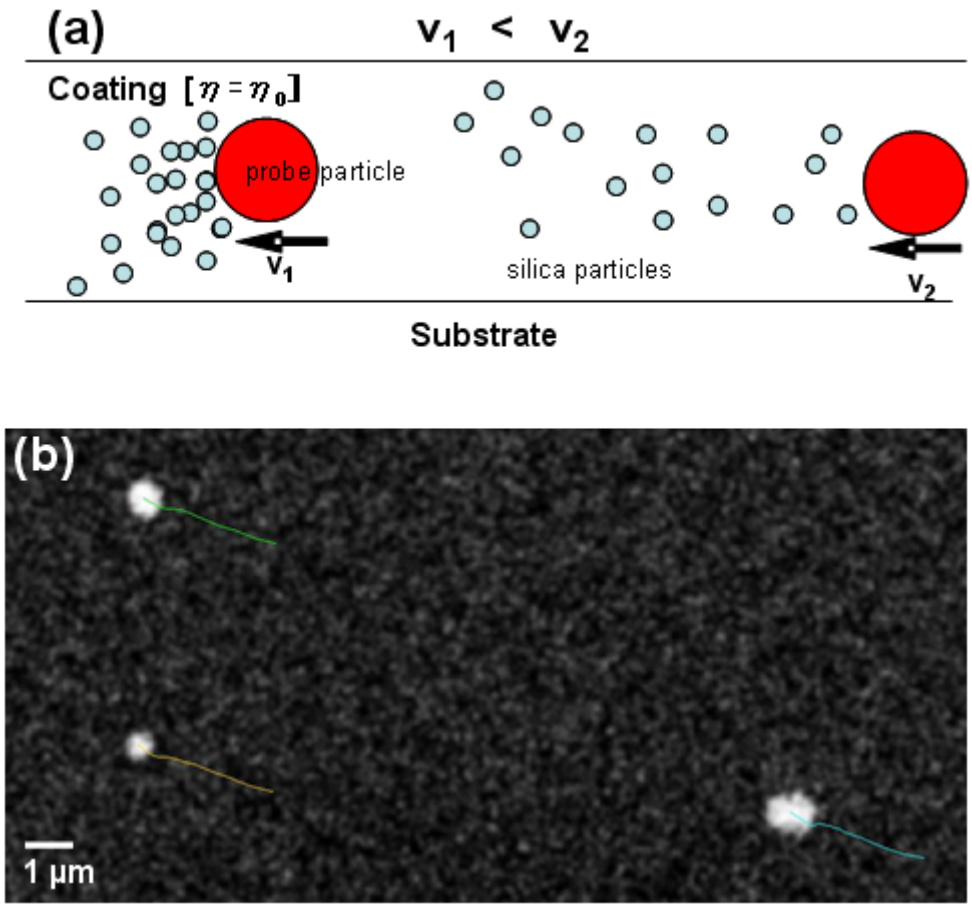

Figure 7.1 (a) Illustration of magnetic probe particle motions in silica/water system with a constant viscosity and (b) observed magnetic probe particle motions influenced by surrounding silica nanoparticles.

7.3 Drying Coating Surface

As drying proceeds, the coating free surface approaches the magnetic probe particle within the focal plane, and it may influence the probe particle motion during the magnetic microrheology experiment. Previous study predicted that drag is reduced when the particle is within one diameter of a liquid/gas interface [110]. Since the coating thickness and viscosity are expected to change dramatically during drying, it is important to understand precisely the effect of free surface position on the magnetic probe particle motion. Our previous coating thickness shrinkage rate data from mass loss measurements were used to estimate the free surface position in drying coatings, however, *in situ* free surface position data during magnetic microrheology experiments will provide more useful information to study the effect of the surface on the particles as well as the development of structure gradients through the thickness, such as skin formation.

Additional set-up is required to monitor the coating thickness change during drying or curing process. A detector needs to be small enough to attach to the current magnetic microrheometer. Laser displacement sensors (Keyence, NJ) can be used for real-time monitoring of the free surface position since they provide high accuracy and resolution, wide measurement range, fast measurement time. They also have small beam spot and long reference distance for more flexible installation [113]. LK-H series or LT-9000 series (Laser confocal displace meter) [113] will be the best to use for *in situ* coating thickness measurement. More precise characterization of coating thickness change will allow the study on more fundamentals of the interaction between coating surface and magnetic probe particles. It can also be used to detect the formation and

position of skin layer with surface rheology techniques using our experimental set-up for magnetic particle tracking or spore tracking on the coating surface.

Bibliography

1. *U.S. Census Bureau, Paint and Allied Products* (2010).

2. J. A. Lewis, K. A. Blackman, A. L. Ogden, J. A. Payne, and L. F. Francis, *Journal of American Ceramic Society*, 79, 3225 (1996).

3. J. A. Payne, L. F. Francis, and A.V. McCormick, *Journal of Applied Polymer Science*, 66, 1267, (1997).

4. R. A. Cairncross and C. J. Durning, *AIChE Journal*, 42, 2415 (1996).

5. R. A. Cairncross, L.F. Francis, and L.E. Scriven, *AIChE* Journal, 42, 55 (1996).

6. C. W. Macosko, *Rheology: Principles, Measurements and Applications*, VCH Publishing, New York (1994).

7. C. M. Chan and S. Venkatraman. *"Coating rheology"* in *Coatings Technology Handbook*, Marcel Dekker, New York (2001).

8. S. G. Croll and L.W. Kisha, *Progress in Organic Coatings*, 20, 27 (1992).

9. W. S. Overdiep, *Progress in Organic Coatings*, 14, 159 (1986).

10. S. E. Orchard, *Applied Scientific Research*, 11, 451 (1963).

11. S. K. Basu, L.E. Scriven, L. F. Francis, and A.V. McCormick, *Progress in Organic Coatings*, 53, 1 (2005).

12. K. M. Balss, G. Llanos, G. Papandreou, and C.A. Maryanoff, *Journal of Biomedical Materials Research - Part A*, 85, 258 (2008).

13. K .M. Balss, F. H. Long, V. Veselov, A. Orana, E. Akerman-Revis, G. Papandreou, and C.A. Maryanoff, *Analytical Chemistry*, 80, 4853 (2008).

14. S. Farquharson and Y. H. Lee, *Proceedings of SPIE-The International Society for Optical Engineering*, 4200, 89 (2000).

15. D. E. Bornside, C. W. Macosko, and L. E. Scriven, *Journal of Applied Physics*, 66, 5185 (1989).

16. R. A. Cairncross, L. F. Francis, and L. E. Scriven, *Drying Technology*, 10,893 (1992).

17. L. F. Francis, A.V. Mccormick, D. M. Vaessen, and J. A. Payne, *Journal of Materials Science*, 37, 4717 (2002).

18. H. Lei, J. A. Payne, A. V. McCormick, L. F. Francis, and W. W. Gerberich, *Journal of Applied Polymer Science*, 81, 1000 (2001).

19. J. A. Payne, A. Strojny, L. F. Francis, and W.W. Gerberich, *Polymer Engineering and Science*, 38, 1529 (1998).

20. G. W. Powers and J. R. Collier, *Polymer Engineering and Science*, 30, 118 (1990).

21. K. Watanabe and T. Amari, *Journal of Applied Polymer Science*, 32, 3435 (1986).

22. S.P. Pappas, *Radiation Curing: Science and Technology*, Plenum, New York (1992).

23. J.P. Fouassier, *Photochemistry and UV Curing: New Trends*, Research Signpost, Kerala, India (2006).

24. T. Slavinsky, *Metal Finishing*, 104, 50 (2006).

25. Y. Otsubo, T. Amari, and K. Watanabe, *Journal of Applied Polymer Science*, 31, 2099 (1986).

26. S. A. Khan, I. M. Plitz, and R.A. Frantz, *Rheologica Acta*, 31, 151 (1992).

27. P. A. M. Steeman, A. A. Dias, D. Wienke, and T. Zwartkruis, *Macromolecules*, 37, 226 (2004).

28. M. E. Nichols, C. M. Seubert, W. H. Weber, and J. L. Gerlock, *Progress in Organic Coatings*, 43, 226 (2001).

29. X. Gu, L. Sung, B. Kidah, M. Oudina, C. Clerici, H. Hu, D. Stanley, W.E. Byrd, J.Y.C. Jean, T. Nguyen, and J.W. Martin, *Journal of Coatings Technology Research*, 6, 67 (2009).

30. R. P. Slopek, H. K. McKinley, C. L. Henderson, and V. Breedveld, *Polymer*, 47, 2263 (2006).

31. E. B. Gutoff and E. D. Cohen, *Coating and Drying Defects; Troubleshooting Operating Problems*, Willey-Interscience, New Jersey (2006).

32. L.O. Kornum and H. K. R. Nielsen, *Progress in Organic Coatings*, 8, 275 (1980).

33. D. Bhattacharya, K. Seo, L. T. Germinario, M. D. Clark, K. W. McCreight, and C. Williams, *Journal of Coatings Technology Research*, 4, 139 (2007).

34. S. Wu, *Journal of Applied Polymer Science*, 22, 2769 (1978).

35. T. C. Patton, *Paint Flow and Pigment Dispersion*, Wiley-Interscience, New York (1979).

36. M. Bosma, R. Brinkhuis, J. Coopmans, and B. Reuvers, *Progress in Organic Coatings*, 55, 97 (2006).

37. Y. Otsubo, T. Amari, K. Watanabe, and T. Nakamichi, *Journal of Rheology*, 31, 251 (1987).

38. A. Belu, C. Mahoney, and K. Wormuth, *Journal of Controlled Release*, 126, 111 (2008).

39. S. Venkatraman and F. Boey, *Journal of Controlled Release*, 120, 149 (2007).

40. B. Balakrishnan, J. F. Dooley, G. Kopia, and E. R. Edelman, *Journal of Controlled Release*, 123, 100 (2007).

41. L. Lazzeri, M.G. Cascone, P. Narducci, N. Vitiello, M. D'Acunto, and P. Giusti, *Tribotest*, 12, 257 (2006).

42. I. Csontos, K. Ronaszegi, A. Szabo, S. Keszei, P. Anna, P. Fekete, G. Marosi, and T. Nagy, *Polymers for Advanced Technologies*, 17, 884 (2006).

43. H. Yang and J. Irudayaraj, *Journal of Pharmacy and Pharmacology*, 54, 1247 (2002).

44. T. Lee and S. Lin, *European Journal of Pharmaceutical Sciences*, 23, 117 (2004).

45. G. Févotte, *A Review: Chemical Engineering Research and Design*, 85, 906 (2007).

46. C. Eliasson and P. Matousek, *Analytical Chemistry*, 79, 1696 (2007).

47. R. E. Tamagawa, E. A. Miranda, and K. A. Berglund, *Crystal Growth and Design*, 2, 511 (2002).

48. R. E. Tamagawa, E. A. Miranda, and K. A. Berglund, *Crystal Growth and Design*, 2, 263 (2002).

49. T. Okumura and M. Otsuka, *Pharmaceutical Research*, 22, 1350 (2005).

50. N. Rodríguez-Hornedo, S. J. Nehm, K.F. Seefeldt, Y. Pagán-Torres, and C.J. Falkiewicz, *Molecular Pharmaceutics*, 3, 362 (2006).

51. T. A. Waigh, *Reports on Progress in Physics*, 68, 685 (2005).

52. P. Cicuta and A. M. Donald, *Soft Matter*, 3, 1449 (2007).

53. A. W. C. Lau, B. D. Hoffman, A. Davies, J. C. Crocker, and T. C. Lubensky, *Physical Review Letters*, 91, 198101/1 (2003).

54. V. Breedveld and D. J. Pine, *Journal of Materials Science*, 38, 4461 (2003).

55. T. Hanemann and K. Honnel, *Ceramics International*, 35, 269 (2009).

56. W. M. Deen, *Analysis of Transport Phenomena*, Oxford, New York (1998).

57. H. C. Berg, *Random Walks in Biology*, Princeton, New Jersey (1993).

58. P. C. Hiemenz and R. Rajagopalan, *Principles of Colloid and Surface Chemistry*, Marcel Dekker, New York (1997).

59. A. G. Fredrickson, *Principles and Applications of Rheology*, Prentice-Hall, Inc., New Jersey (1964).

60. M. L. Gardel, M. T. Valentine, and D. A. Weitz, *"Microrheology"* in *Microscale Diagnostic Techniques*, Springer-Verlag, New York (2005).

61. F. Amblard, B. Yurke, A. Pargellis, and S. Leibler, *Review of Scientific Instruments*, 67, 818 (1996).

62. E. P. Furlani and K. C. Ng, *Physical Review E*, 73, 061919 (2006).

63. A. R. Bausch, W. Möller, and E. Sackmann, *Biophysical Journal*, 76, 573 (1999).

64. M. Keller, J. Schilling, and E. Sackmann, *Review of Scientific Instruments*, 72, 3626 (2001).

65. C. Gosse and V. Croquette, *Biophysical Journal*, 82, 3314 (2002).

66. C. Haber and D. Wirtz, *Review of Scientific Instruments*, 71, 4561 (2000).

67. K. C. Neuman and A. Nagy, *Nature Methods*, 5, 491 (2008).

68. K. C. Neuman, T. Lionnet, and J. Allemand, *Annual Review of Materials Research*, 37, 33 (2007).

69. H. D. Ou-Yang, *"Design and application of oscillating optical tweezers for direct measurements of colloidal forces"* in *Colloid-Polymer Interactions: From Fundamentals to Practice*, Wiley, New York (1999).

70. K. C. Neuman and S. M. Block, *Review of Scientific Instruments*, 75, 2787 (2004).

71. E. J. G. Peterman, F. Gittes, and C. F. Schmidt, *Biophysical Journal*, 84, 1308 (2003).

72. E. A-Hassan, W. F. Heinz, M. D. Antonik, N. P. D'Costa, S. Nageswaran, C. A. Schoenenberger, and J. H. Hoh, *Biophysical Journal*, 74, 1564 (1998).

73. R. E. Mahaffy, C. K. Shih, F. C. MacKintosh, and J. Käs, *Physical Review Letters*, 85, 880 (2000).

74. T. Okajima, H Arakawa, M. T. Alam, H. Sekiguchi, and A. Ikai, *Biophyical Chemistry*, 107, 51 (2004).

75. R. S. Khandpur, *Handbook of Analytical Instruments*, McGraw-Hill, New York (2007).

76. J. Twardowski and P. Anzenbacher, *Raman and IR spectroscopy in biology and biochemistry*, Ellis Horwood, New York (1995).

77. C. J. Frank, R. L. McCreery, D. C. B. Redd, and T. S. Gansler, *Applied Spectroscopy*, 47, 387 (1993).

78. Y. Huang, T. Karashima, M. Yamamoto, and H. Hamaguchi, *Biochemistry*, 44, 10009 (2005).

79. M. Osterhold, *European Coatings Journal*, 4, 6 (2000).

80. C. Schoff, *Journal of Coatings Technology*, 71, 56 (1999).

81. G. Wisanrakkit and J. K. Gillham, *Journal of Applied Polymer Science*, 42, 2453 (1991).

82. A. R. Bausch, F. Ziemann, A.A. Boulbitch, K. Jacobson, and E. Sackmann, *Biophysical Journal*, 75, 2038 (1998).

83. J. L. Lewis, S. M. Burns, S. J. Samuels, R. L. Powell, and D. F. Katz, *Review of Scientific Instruments*, 65, 3268 (1994).

84. I. C. Carpen and J. F. Brady, *Journal of Rheology*, 49, 1483 (2005).

85. F. K. Oppong, L. Rubatat, B. J. Frisken, A. E. Bailey, and J. R. de Bruyn, *Physical Review E*, 73, 041405 (2006).

86. M. Gahleitner and R. Sobczak, *Rheologica Acta*, 26, 371 (1987).

87. Y. I. Cho, J. P. Hartnett, and W. Y. Lee, *Journal of Non Newtonian Fluid Mechanics*, 15, 61 (1984).

88. http://www.hirox-usa.com/products/mount_lens.html

89. S. A. Jenekhe, *Polymer Engineering and Science*, 23, 830 (1983).

90. T. G. Mason and D. A. Weitz, *Physical Review Letters*, 74, 1250 (1995).

91. I. D. Chang, *ZAMP*, 12, 6 (1961).

92. Y. Cohen and A. B. Metzner, *AIChE Journal*, 27, 705 (1981).

93. W. B. Russel, D. A. Saville, and W. R. Schowalter, *Colloidal Dispersions*, Cambridge, New York, (1989).

94. S. S. Lee, A. Luciani, and J. E. Månson, *Progress in Organic Coatings*, 38, 193 (2000).

95. H. Claesson, E. Malmström, M. Johansson, A. Hult, M. Doyle, and J. E. Månson, *Progress in Organic Coatings*, 44, 63 (2002).

96. L. E. Schmidt, Y. Leterrier, J. Vesin, M. Wilhelm, and J. E. Månson, *Macromolecular Materials and Engineering*, 290, 1115 (2005).

97. L. R. Gatechair and A. M. Tiefenthaler, *"Depth of Cure Profiling of UV-Cured Coatings"*, in *Radiation Curing of Polymeric Materials*, American Chemical Society (1990).

98. J. F. Rabek, *"Polymer Photodegradation - Mechanism and Experimental Methods*", Champman & Hall, New York (1995).

99. X. Gu, C. A. Michaels, P. L. Drzal, J. Jasmin, D. Martin, T. Nguyen, and J. W. Martin, *Journal of Coatings Technology Research*, 4, 389 (2007).

100. V. Y. Voytekunas, F. L. Ng, and M. J. M. Abadie, *European Polymer Journal*, 44, 3640 (2008).

101. http://www.spectroline.com/laboratory/lab_lamps_uv-quartz.html

102. http://www.spectroline.com/laboratory/lab_digitalradiometers_drc-series.html

103. J.-O. Song, R. M. Henry, R. M. Jacobs, and L. F. Francis, *Review of Scientific Instruments*, 81, 093903 (2010).

104. B. J. Love and F. Piguet-Ruinet, *Journal of Applied Polymer Science*, 106, 3605 (2007).

105. M. Lin and M. Wang, *Polymer International*, 48, 1237 (1999).

106. J. V. Crivello and U. Varlemann, *Journal of Polymer Science: Part A*, 33, 2463 (1995).

107. R. S. Hunter and R. W. Harold, *The Measurement of Appearance*, Wiley, New York (1987).

108. G. C. Dubbeldam, *Progress in Organic Coatings*, 20, 261 (1992).

109. H. L. Frisch and C. Scopazzi, *Journal of Applied Polymer Science*, 43, 1067 (1991).

110. C. Berdan II and L.G. Leal, *Journal of Colloid and Interface Science*, 87, 62 (1982).

111. J. Dong, J. D. Foley, C. Frethem, R. A. Hoerr, M. J. Matuszewski, J. E. Puskas, and G. Haugstad, *Langmuir*, 25, 5442 (2009).

112. http://www.witec.de

113. http://www.kyence.com